Measurement of jet properties in pp and Pb-Pb collisions at $\sqrt{s_{\mathrm{NN}}} = 5.02$ TeV with the ALICE experiment at the LHC

Ritsuya Hosokawa

March 2019

Measurement of jet properties in pp and Pb-Pb collisions at $\sqrt{s_{\mathrm{NN}}} = 5.02$ TeV with the ALICE experiment at the LHC

Ritsuya Hosokawa

Submitted to
the Graduate School of Pure and Applied Sciences
at the University of Tsukuba
and
Doctoral School of Physics
at Université Grenoble Alpes
in Partial Fulfillment of the Requirements
for
the Degree of Doctor of Philosophy in Science

Abstract

Jets, defined as collimated sprays of high-momentum particles, are experimental signatures of hard-scattered quarks and gluons produced in hadronic interactions. Jet production cross sections are calculable within perturbative Quantum ChromoDynamics (pQCD), and therefore jet measurements provide stringent tests of pQCD predictions. In ultrarelativistic heavy-ion collisions, jets are well calibrated probes of the Quark-Gluon Plasma (QGP). Under extreme conditions of high temperature and/or high pressure, partons are deconfined and form a strongly interacting QCD medium. The initial hard scattered partons lose energy while traversing this medium due to radiative and collisional energy loss. Consequently, jet properties get modified in comparison with the vacuum case, phenomenon named jet quenching. QGP transport properties can be studied by measuring jet quenching.

The charged jet production cross sections in proton-proton collisions at $\sqrt{s} = 2.76$ TeV and $\sqrt{s} = 7$ TeV were measured by the ALICE experiment. The predictions of pQCD calculations with Leading-Order (LO) accuracy were compared with the measurements and exhibited only poor agreement by about 20-50 %. In Pb-Pb collisions, the strength of jet suppression was quantitatively assessed at $\sqrt{s_{\rm NN}} = 2.76$ TeV and $\sqrt{s_{\rm NN}} = 5.02$ TeV through the measurement of the nuclear modification factors ($R_{\rm AA}$). The strength of charged jet suppression was quantified as a function of in-medium parton path-length based on the measured $R_{\rm AA}$. The jet elliptic flow v_2, defined as the jet azimuthal distribution relative to the 2^{nd} order event plane, which is sensitive to the difference of the in-medium parton path-length in-plane and out-of-plane, was measured at $\sqrt{s_{\rm NN}} = 2.76$ TeV. The measured jet v_2 in mid-central Pb-Pb collisions was consistent with model predictions. The medium response was studied through jet-track correlations at $\sqrt{s_{\rm NN}} = 2.76$ TeV as a function of centrality. The result suggested that the in-medium suppressed energy was re-distributed to large angles with respect to the jet axis. The phenomenon was described by a phenomenological calculation taking into account hydrodynamical evolution of the medium.

In this thesis, two complementary aspects of jet physics with the ALICE detector at the LHC are studied. First, the upgrade of the ALICE electromagnetic calorimeter trigger system is presented. The Di-jet Calorimeter (DCal) was installed during LHC Long Shutdown

1 to extend the azimuthal coverage of the existing ElectroMagnetic Calorimeter (EMCal) and PHOton Spectrometer (PHOS). The trigger system has been upgraded to account for this new detector configuration. We upgraded the firmware for the Summary Trigger Unit , which is the electronics of the trigger system, to implement a brand new algorithm combining information from the three calorimeters. We also carried out the upgrades for the new data stream convention and for communication error monitoring system among electronics for the trigger system. We performed the commissioning tasks for the trigger system before the data taking of Pb-Pb collisions in 2015 and the trigger system have been operated throughout the LHC Run2 (2015-2018). The new physics results utilizing the triggered data start to come out.

Second subject is charged jet measurements in pp and Pb-Pb collisions at $\sqrt{s_{\rm NN}} =$ 5.02 TeV. The measurement of the production cross section of charged jets reconstructed with cone resolution parameter $R = 0.2$, 0.3, 0.4, and 0.6 in pp collisions at $\sqrt{s} = 5.02$ TeV is for jet transverse momentum $5 < p_{\rm T,jet}^{\rm ch} < 100$ GeV/c is outlined. A comparison of the production cross section to LO and Next-Leading-Order (NLO) pQCD predictions is shown. Good agreement, within about 10% discrepancy, of the production cross section with NLO pQCD calculations is found for $10 < p_{\rm T,jet}^{\rm ch} < 100$ GeV/c with large theoretical uncertainties. The NLO pQCD calculations shows large discrepancy from the measured result in lower $p_{\rm T,jet}$ range ($5 < p_{\rm T,jet}^{\rm ch} < 10$ GeV/c) though the theoretical uncertainties are also large. The systematic uncertainties on the pQCD calculation could be improved with higher-order calculation, such as Next-to-Next-to-Leading Order. It may also be important to understand non-perturbative effects, such as the underlying event, for an improved understanding of the jet production cross section in this low $p_{\rm T,jet}$ region. The measurement of charged jet v_2 in mid-central (30-50%) Pb-Pb collisions at $\sqrt{s_{\rm NN}} = 5.02$ TeV is presented. The result is compared with the charged jet v_2 in Pb-Pb collisions at $\sqrt{s_{\rm NN}} = 2.76$ TeV. No collision energy dependence on the charged jet v_2 is found. The result is also compared with a toy-model Glauber simulation based on the estimated jet suppression strength from the measured charged jet $R_{\rm AA}$. It is found that both jet $R_{\rm AA}$ and jet v_2 are simultaneously described by the medium-induced constant jet transverse momentum suppression of $\Delta p_{\rm T} \propto \rho^{1.1} \langle L_\sigma \rangle^{2.6}$. Here, $\langle L \rangle$ is the average in-medium parton path-length estimated with a Glauber simulation and ρ is the centrality dependent initial energy density. This result is close to the in-medium radiative energy loss scenario of $\Delta p_{\rm T} \propto \rho^{3/4} L^2$. However, one another scenario of $\Delta p_{\rm T} \propto \sqrt{\rho} L$ is not ruled out due to current large uncertainty. Finally, the measurement of charged jet-hadron correlations in mid-central (30-50%) Pb-Pb collisions at $\sqrt{s_{\rm NN}} = 5.02$ TeV with respect to the 2^{nd} order event plane is also presented in

order to study initial collision geometry dependence of jet modification in Pb-Pb collisions is presented. The near-side correlation functions for trigger jets $p_{\mathrm{T,jet}} > 20$ GeV/c and associated tracks $0.7 < p_{\mathrm{T,track}}^{\mathrm{assoc}} < 2$ GeV/c, $2 < p_{\mathrm{T,track}}^{\mathrm{assoc}} < 4$ GeV/c are measured. Broader near-side jet peak shape out-of-plane jet in comparison with the one in-plane is observed for $0.7 < p_{\mathrm{T,track}}^{\mathrm{assoc}} < 2$ GeV/c associates. A near-side peak position shift in azimuth towards in-plane direction are also observed for both p_{T} range. The measured jet-hadron correlations are compared to a model prediction by JEWEL. Only the peak position shift for low-p_{T} associates are partially reproduced by the prediction. This result suggests that the near-side peak shape modification w.r.t 2^{nd}-order event plane cannot be described only by the in-medium parton energy loss and parton shower evolution. The medium-induced near-side jet modification may be understood as a combination of in-medium radiation, initial geometry dependent energy suppression and medium response with hydrodynamical evolution.

Acknowledgments

Firstly, I would like to express the deepest gratitude to Prof. R. Guernane and Prof. T. Chujo, who supported my reserch activities and also daily life in France and Japan. They gave me a lot of advices on my analysis and support for works overseas. I would like to express appreciation to Dr. H. Yokoyama who also supported reserch activities. Especially, no doubt that the trigger system upgrade for ALICE calorimeters could not be completed without his co-working.

I would like to express deep gratitude to Prof. Y. Miake, Prof. Y. R. Schutz and Prof. C. Furget. They gave me the opportunity to reserch the high-energy nuclear physics. I also would like to thank for their careful reading of my thesis. I express deep gratitude to Prof. K. Oyama for careful reading and reviewing this PhD thesis. My deep appreciation goes to Prof. S. Esumi. He gave me a lot of meaningful advices for the physics analysis. I would like to thank professional instructions about electronics from Prof. I. Motoi. I would like to express many thanks to Prof. O. R. Bourrion, Prof. G. C. Balbastre, Prof. J. Faivre who gave me meaningful advices when I was working at Grenoble. I appreciate Prof. S. Sakai, Dr. H. Masui, Dr. Y. Watanabe, Prof. N. Jaime, who gave me insightful advices and many support for my works. I recieved technical support from Mr. S. Kato, who maintained the computing system at University of Tsukuba.

I would like to express deep gratitude to all the current and previous members of High energy nuclear physics group at University of Tsukuba and Universitè Grenoble Alpes (LPSC). Especially, I would like to thank for frendship and a lot of discussions with Dr. T. Nonaka, Mr. W. Sato, Dr. R.Aoyama, Dr. T. Sugiura, Dr. N. Tanaka, Dr. H. Nakagomi, Dr. D. Watanabe, Dr. S. Mizuno, Dr. H. Hassan. I also express my thank to frendship with Dr. T. Todoroki, Dr. T. Niida, Dr. J. Bhom, Mr. K. Oshima, Ms. H. Ozaki, Mr. T. Kobayashi, Mr. K. Kihara, Mr. J. Lee, Mrs. I. Sakatani, Mr. T. Shioya, Mr. M. Hirano, Mr. H. Yamamoto, Mr. B. Kim, Mr. K. Ito, Ms. S. Kudo, Ms. M. Chang, Mr. Y. Fukuda, Mr. K. Sato, Mr. T. Ichisawa, Mr. H. Kato, Mr. D. Kawana, Mr. Y. Kawamura, Mr. T. Suzuki, Mr. K. Nakagawa, Mr. T. Nishimatsu, Mr. H. Joung, Mr. M. Takamura, Mr. K. Tadokoro, Ms. K. Nakagawa, Ms. M. Hatakeyama, Ms. Y. Hoshi, Mr. N. Ito, Mr. K.

Okubo, Ms. Y. Sato, Mr. Y. Sudo, Mr. K. Tsukui, Mr. R. Nakazato, Mr. K. Mitamura, Mr. K. Yasaki.

I would like to express deep gratitude to ALICE Asian France (AAF) colloborators. Especially, Prof. O. Busch, who is now resting in peace, provided me large amount of knowledge and insightful advices for my analysis. I'm confident that I wouldn't achieve my studies without him. I would like to thank Prof. Y. Mao, Prof. H. Pei for their advices for my tasks and management of the collaboration.

I would like to express ,any thanks to the colleagues, Dr. D. Sekihata, Ms. H. Murakami, Dr. S. Yano, Dr. T. Okubo, Mr. K. Terasaki, Mr. K. Yamakawa, who spent good time together at CERN.

Finally, I would like to thank my parents, Mr. Y. Hosokawa and Mrs. Y. Hosokawa for their understanding and continuous support for my activities.

Contents

List of Tables

List of Figures

Chapter 1 Introduction

One of the ultimate questions for Physics is *'What is the origin of matter and how its constituents interact with each other?'*. In our current understanding, the world is governed by four fundamental interactions - electromagnetic, weak, strong, and gravity. Today, the theory of general relativity [1] and the Standard Model [2, 3] are the successful theories to describe the fundamental interactions and the elementary particles. Three of the fundamental interactions - electromagnetic, weak and strong - are well modeled in the framework of the Standard Model while the gravity interaction is described by the theory of general relativity. The Standard Model is the integration of the electroweak model which describes the electromagnetic and weak interactions, and Quantum ChromoDynamics (QCD) which describes the strong interactions.

The elementary particles are classified into two groups in the Standard Model: fermions and bosons. Quarks and leptons are fermions and they compose the matters while the gauge bosons (photon, gluon, Z and W) play the role of force carriers. The Higgs boson is the only scalar boson in the Standard Model which gives mass to fundamental particles [4]. The elementary particles in the Standard Model are listed in Fig. 1.

The physics of quarks and gluons, which are collectively called 'partons', in other words the physics at the scale where the QCD effects are dominant, is the subject of this thesis. Partons cannot be isolated and are confined under normal conditions into bound states, which are called 'hadrons'. However, indirect signatures of a parton can be observed in high-energy particle collisions as collimated sprays of high-momentum final-state particles, known as 'Jets'.

In this thesis, jets are measured with a twofold interest. Firstly, a measurement of jet production cross sections provides stringent tests of theoretical predictions since the elementary process of jet production is one of the most fundamental processes in QCD. In this work, the charged jet production cross section in pp collisions at $\sqrt{s} = 5.02$ TeV is measured and compared to several perturbative QCD (pQCD) based model predictions. Secondly, the Quark-Gluon Plasma (QGP), the state of hot and dense QCD matter formed in ultrarelativistic heavy-ion collisions, can be probed by measuring jets. As mentioned above, partons are normally confined into hadrons but, under the extreme conditions of high temperature and/or high density, partons are deconfined to form a hot and dense

QCD medium. Measurements of jets allow to probe the entire evolution of QGP in ultra-relativistic heavy-ion collisions since jets originate from hard-scatterings taking place at the early stages of the collision. It is expected that the energy of these initial hard-scattered partons is suppressed while traversing the QGP which results in modifying the jet properties in comparison with QCD vacuum. In Ref.[5], the charged jet production cross sections in Pb-Pb collisions at $\sqrt{s_{\rm NN}} = 5.02$ TeV were measured to build the charged jet nuclear modification factors ($R_{\rm AA}$) by using the results obtained in pp collisions. In this thesis, more differential measurements of jet v_2 and jet-hadron correlations in Pb-Pb collisions at $\sqrt{s_{\rm NN}} = 5.02$ TeV are presented to study jet modifications owing to parton energy loss and re-distribution in the QGP.

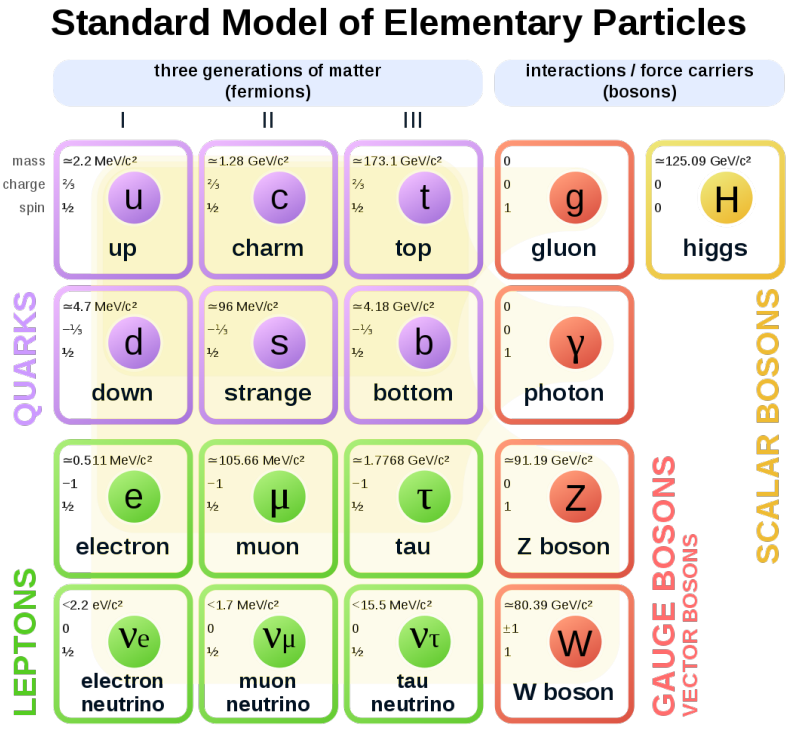

Figure 1: The Standard Model of elementary particles [6]

1.1 Quantum Chromodynamics (QCD)

The interaction between partons is dominantly governed by the strong interaction. On the larger scale, the strong interaction is effective in binding nucleons inside nuclei.

The Quantum ChromoDynamics (QCD) is a non-Abelian quantum field theory that

Interaction	Relative strength	Carrier
Weak	10^{25}	Z and W boson
Strong	10^{38}	gluon
Electromagnetic	10^{36}	photon
Gravitation	1	graviton (undiscovered)

Table 1: The four fundamental interactions in the nature. The relative strength of Gravitation is taken to have a value of 1.

describes the strong interaction [7, 8]. The gauge symmetry of QCD quantum numbers, the 'color charges', are described by $SU(3)$ group. $SU(3)$ group consists of a set of unitary 3×3 matrices.The fundamental representation of $SU(3)$ is a triplet. The three color charges of quarks (Red, Green, Blue) form a $SU(3)$ symmetry group. $SU(3)$ group has $3^2 - 1 = 8$ generators which correspond to 8 gluons. Since gluons carry color charges, not only quarks but also gluons do interact with each other.

The gauge invariant QCD Lagrangian is expressed as:

$$\mathcal{L} = \bar{q}(i\gamma^\mu \partial_\mu - m)q - g(\bar{q}\gamma^\mu T_a q)G^q_\mu - \frac{1}{4}G^a_{\mu\nu}G^{\mu\nu}_a \tag{1}$$

where $q, \bar{q}$ are the color and anti-color fields, γ^μ is the Dirac $\gamma-$matrix, g is the strong coupling constant, G^a_μ is the gauge field for a given color a. $G^a_{\mu\nu}$ is the field strength tensor which is expressed as:

$$G^a_{\mu\nu} = \partial_\mu G^a_\nu - \partial_\nu G^a_\mu - g f_{abc} G^b_\mu G^c_\nu \ . \tag{2}$$

The coupling constant g is given as a function of the theory's equivalent of the fine structure constant $\alpha_s(Q^2)$ as:

$$g \equiv \sqrt{4\pi\alpha_s(Q^2)} \tag{3}$$

where Q is the energy scale of the process.

1.1.1 Asymptotic freedom and Confinement

One of the most remarkable features of QCD is that the coupling constant becomes small at large energy scale. This behavior is known as 'asymptotic freedom'. It suggests that perturbative calculations are applicable for large energy scale QCD processes. The α_s at leading order in perturbative expansion of the strong coupling is given as a function of the energy scale Q by:

$$\alpha_s(Q^2) = g^2/4\pi = \frac{1}{\beta_0 ln(Q^2/\Lambda^2_{QCD})} \tag{4}$$

where, β_0 is the 1-loop β-function coefficient and Λ_{QCD} is the QCD scale parameter. Λ_{QCD} is an important parameter for the predictive capability of QCD because it gives the starting

energy scale at which a perturbative calculation becomes applicable. The current most probable value of Λ_{QCD} is 210 ± 14 MeV [2].

While asymptotic freedom allows to probe partons at large energy scale, the growth of the coupling constant at small energy scale leads to the binding of partons into color-singlet hadrons of size of the order of 1 fm. This behavior is known as 'color confinement' or simply 'confinement'. The potential of a static quark and anti-quark pair is obtained phenomenologically by fitting the lattice QCD calculations with the following function:

$$V(r) = V_0 - \frac{\alpha}{r} + \sigma r \tag{5}$$

where r is the distance between two quarks and $V_0,\ \alpha,\ \sigma$ are the unknown parameters. The fit result is shown in Fig. 2.

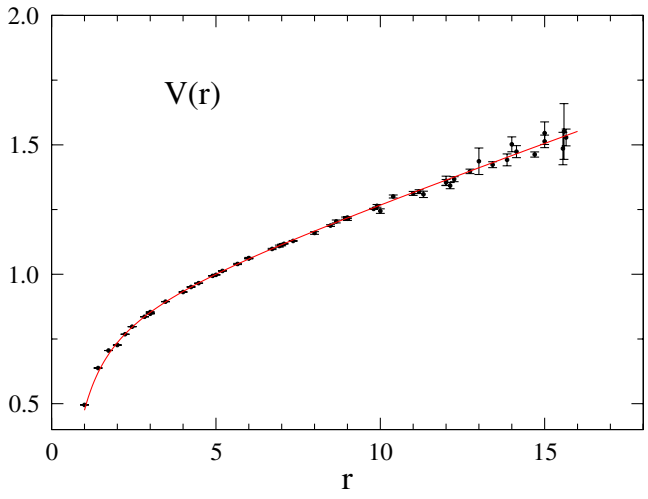

Figure 2: Static quark potential $V(r)$ from 2+1 flavor lattice QCD calculations [9]

1.2 Hard scattering and Jets

Hard parton scatterings of large momentum transfer ($Q^2 \gg \Lambda_{QCD}$) is the dominant mechanism for high-transverse momentum (p_{T}) hadron production in high-energy nucleus-nucleus collisions. The production cross section of high-p_{T} hadrons is calculable from the underlying parton-parton processes using the 'factorization theorem' [10]. The hadronic production cross section of a hadron h, to order $\mathcal{O}(1/Q^2)$, is expressed as:

$$d\sigma_{AB\to h} = f_{a/A}(x_1, Q^2) \otimes f_{b/B}(x_2, Q^2) \otimes d\sigma_{ab\to c}(x_1, x_2, Q^2) \otimes D_{c\to h}(z, Q^2) \tag{6}$$

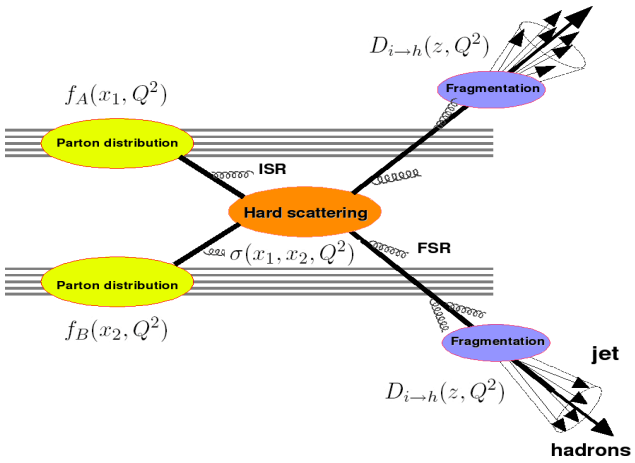

Figure 3: Sketch of the hard scattering in hadronic collisions [8]

where $f_{a/A}(x,Q^2)$ is the Parton Distribution Function (PDF), the probability of finding a parton of flavour a with momentum fraction $x = p_{\mathrm{a}}/p_{\mathrm{A}}$ in a nucleus A. $d\sigma_{ab\to c}$ is the partonic hard-scattering cross section for partons a and b. $D_{c\to h}$ is the Fragmentation Function (FF) which is the probability of the outgoing parton c to fragment into hadron h with $z = p_h/p_c$. For example, Fig. 4 shows the PDF measured with deep inelastic $e^{\pm}p$ scattering [11] and Fig. 5 shows the FF for positively charged pions based on single-inclusive pion production in electron-positron annihilation, lepton-nucleon deep-inelastic scattering, and proton-proton collisions [12].

As illustrated in Fig. 3, hard scattered partons undergo a so-called parton shower before fragmenting into final state hadrons resulting in collimated sprays of high-p_{T} hadrons. This collimated spray of hadrons, called '*jet*', is the typical experimentally measurable signature of partons. Since most of jets originate from $2 \to 2$ parton scattering process, two jets are usually produced back-to-back in azimuth (di-jets).

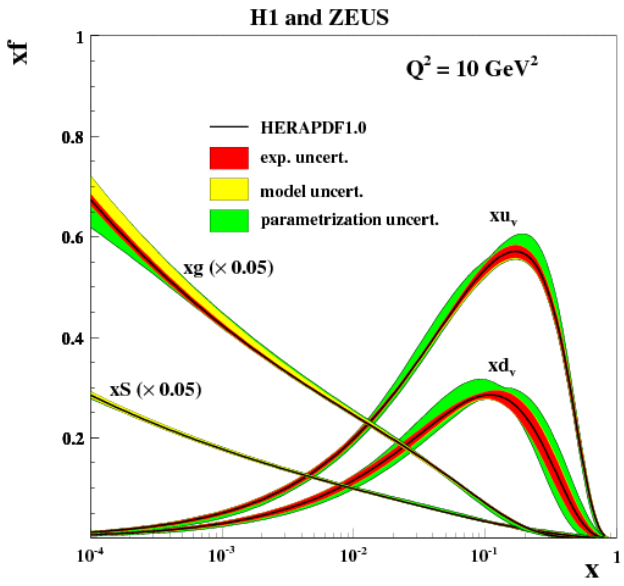

Figure 4: The Parton Distribution Functions from HERAPDF1.0 at $Q^2 = 10$ GeV^2 [11].

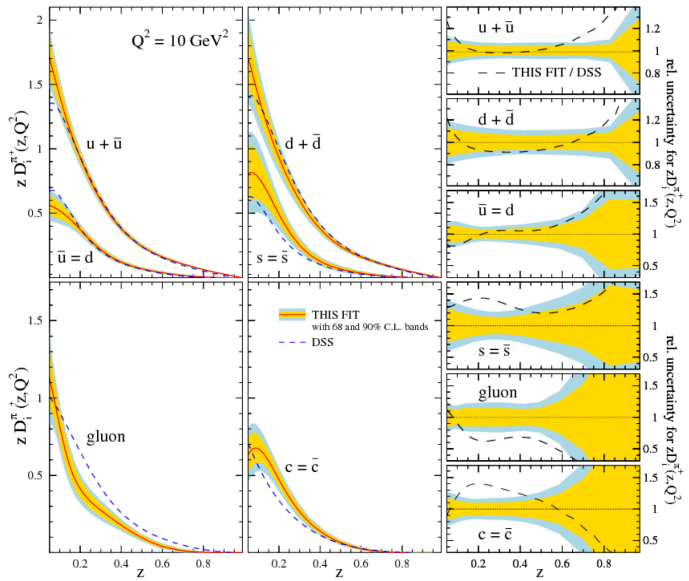

Figure 5: The individual Fragmentation Functions for positively charged pions $zD_i^{\pi^+}$ at $Q^2 = 10$ GeV^2 [12].

1.3 Quark-Gluon Plasma (QGP)

Because of color confinement, partons are bound into hadrons under normal conditions as mentioned in Sec.1.1.1. However, at extremely high temperatures and/or densities, partons are expected to deconfine and behave like free particles because of asymptotic freedom.

Deconfined partons form a strongly interacting QCD medium, called 'Quark-Gluon Plasma' (QGP) by analogy with classical electromagnetic 'plasma'. Historically, QGP formation was originally predicted by Collins and Perry [13], who predicted that matter composed of quarks may exist under extreme conditions such as in the core of neutron stars and in early Universe a few μs after the Big Bang. Results from recent lattice QCD calculations, predict a critical temperature $T_c \sim 150-200$ MeV and energy density $\epsilon_c \sim 0.5-1.2$ GeV/fm^3 for the phase transition from hadronic to QGP state. Fig. 6 illustrate our current understanding QCD phase diagram and Fig. 7 shows the results of lattice QCD calculations. The experimental evidence of QGP formation is introduced in Sec.1.7.1 and 1.7.2.

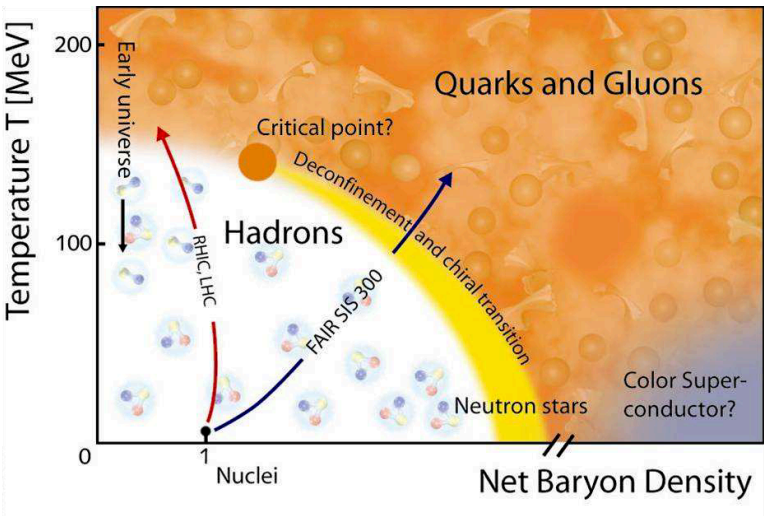

Figure 6: A sketch of the QCD phase diagram [14]

1.4 Relativistic heavy-ion collisions

Relativistic heavy-ion collisions provide unique experimental conditions for QGP formation in the laboratory. Particle accelerators propel massive nuclei to almost speed of light and cause them to collide. As of 2018, high-energy heavy-ion collision experiments are performed at the Relativistic Heavy Ion Collider (RHIC) and the Large Hadron Collider (LHC). These are circular particle accelerators built at Brookhaven National Laboratory

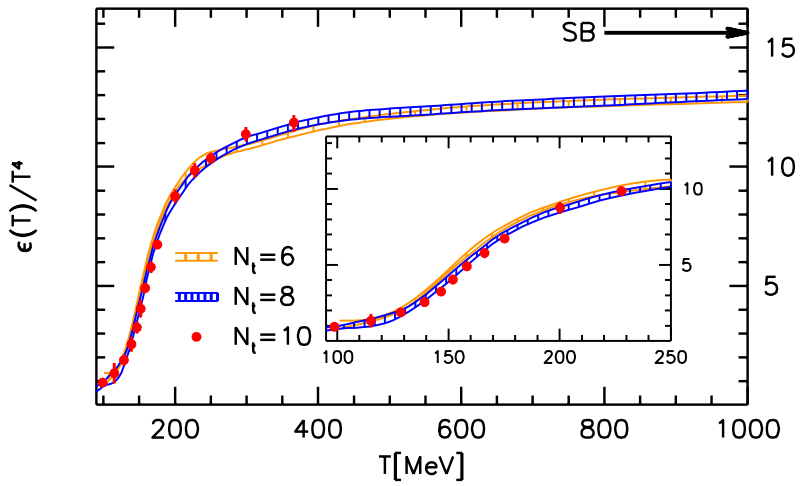

Figure 7: The energy density normalized by T^4 as a function of the temperature. SB is the Stefan-Boltzmann limit $\epsilon_{SB} = 3p_{SB}$ [15]

(BNL) and European Organization for Nuclear Research (CERN) respectively. An energy density of 5.4 ± 0.6 GeV/fm^3 in central Au+Au collisions at $\sqrt{s_{\rm NN}} = 200$ GeV was reported at RHIC [16] and 13 ± 2 GeV/fm^3 in central Pb-Pb collisions at $\sqrt{s_{\rm NN}} = 2.76$ TeV at LHC [17]. RHIC and LHC have both reached energy densities in heavy-ion collisions higher than the predicted critical energy density for QGP formation. At RHIC, various nucleus species are accelerated to different center-of-mass energies to study system size and energy dependence of QGP observables and to explore the QCD diagram of state. At LHC, proton and lead nuclei are accelerated up to the currently world's top center-of-mass energy of $\sqrt{s_{\rm NN}} = 5.02$ TeV. Longer QGP life-time and larger jet production cross sections are expected at LHC energies than at RHIC top energy. Therefore, studies of partonic energy loss in QGP with hard probes, such as jets, are one of the main subjects of the LHC physics program. Features of ultrarelativistic heavy-ion collision experiments performed at BNL and CERN are summarized in Table 2. The experimental datasets of pp and Pb-Pb collisions at $\sqrt{s_{\rm NN}} = 5.02$ TeV used for the measurements presented in this thesis were recorded in 2015 by the ALICE detector at the LHC [18].

Table 2: Summary of relativistic heavy ion collisions

Year	Accelerators	Location	Species	$\sqrt{s_{\mathrm{NN}}}$ Energy(GeV)
1986	AGS	BNL	^{16}O, ^{28}Si	5.4
1992			^{197}Au	4.8
1986	SPS	CERN	^{16}O, ^{32}S	19.4
1994			^{208}Pb	17.4
2000	RHIC	BNL	^{197}Au	130
2001			^{197}Au	200
2003			d-^{197}Au	200
2004			^{197}Au	200, 62.4
2005			^{63}Cu	200, 62.4, 22.4
2007			^{200}Au	200
2008			d-^{197}Au	200, 62.4
2010			^{197}Au	200, 62.4, 39, 11.5, 7.7
2011			^{197}Au	200, 19.6, 27
2012			^{238}U	193
2012			^{63}Cu-^{197}Au	200
2014			^{197}Au	200, 14.6
2014			^{3}He-^{197}Au	200
2015			p-^{197}Au	200
2015			p-^{197}Al	200
2016			^{197}Au	200
2016			d-^{197}Au	200, 62.4, 19.6, 39
2017			^{197}Au	54
2018			^{96}Zr,^{96}Ru	200
2018			^{197}Au	27
2010	LHC	CERN	^{208}Pb	2760
2011			^{208}Pb	2760
2013			p-^{208}Pb	5020
2015			^{208}Pb	5020
2016			p-^{208}Pb	5020, 8160
2017			^{129}Xe	5440
2018			^{208}Pb	5020

1.4.1 Space-time evolution

In this section, a global picture of heavy-ion collisions is described. Fig. 8 shows the space-time evolution of a nucleus-nucleus collision. The initial collision time is $\tau = 0$.

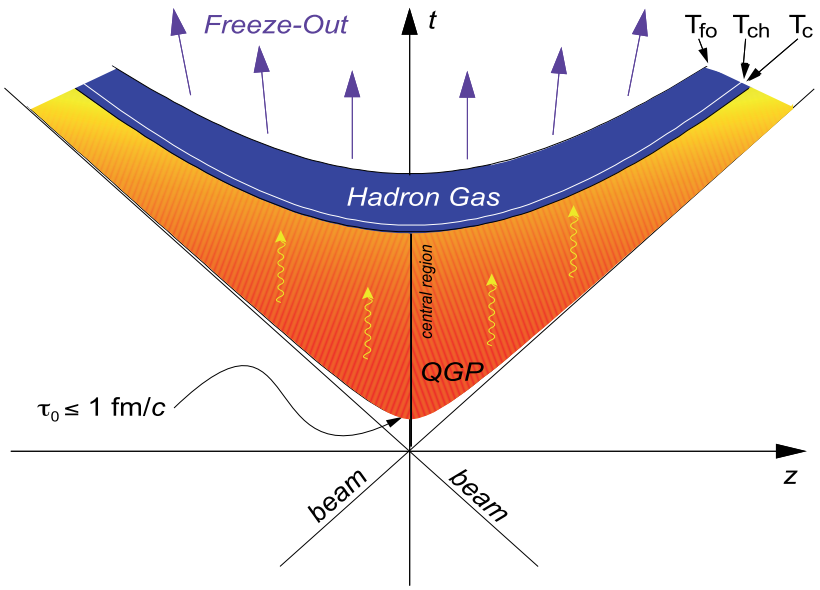

Figure 8: Sketch of the space-time evolution of a nucleus-nucleus collision [8]

1.) Before collision ($\tau < 0$)

Nuclei are accelerated to the desired center-of-mass energy. Due to Lorentz contraction, the longitudinal thickness of the nuclei is contracted to $2R/\gamma$, where R is the radius of the nuclei and γ is the Lorentz factor.

2.) Nuclear overlap and Pre-equilibrium ($0 < \tau < \tau_0$)

During collision, a large amount of partons are created experiencing multiple interactions leading to the formation of partonic matter. The collision energy is deposited into initial overlapping region of the two colliding nuclei. During the early stages of the collision, hard processes occur.

3.) QGP formation and hydrodynamical evolution ($\tau_0 < \tau < \tau_c$)

If the system reaches the critical conditions during step 2.), a QGP state is created at time τ_0. The space-time evolution of the QGP can be described by the equations of relativistic hydrodynamics. Following the hydrodynamical expansion of the system, the mean free path-length of partons increases and the system cools down.

4.) Chemical freezeout ($\tau_c < \tau < \tau_{ch}$)

When the system conditions drop below the critical conditions at time τ_c (corresponding to the critical temperature T_c) partons confined back into individual hadrons when their mean free path-length becomes comparable to the system size. Hadron species are fixed at time τ_{ch} (T_{ch}), which is called 'chemical freezeout'.

5.) Kinetic freezeout ($\tau_{ch} < \tau < \tau_{fo}$)

Hadrons continue to interact elastically after chemical freezeout. Momenta and energies of hadrons are fixed when the mean free path-length of hadrons becomes sufficiently longer than the system size. This stage called 'kinetic freezeout' takes place at time τ_{fo} (T_{fo}). We are able to detect hadrons after freezeout steps, 4.) and 5.).

1.4.2 Collision geometry - Participants and spectators

In this section, geometrical aspects of relativistic heavy-ion collisions are explained. The understanding of collision geometry is essential to explore QGP properties. Fig. 9 illustrates two nuclei before and after a non-central heavy-ion collision.

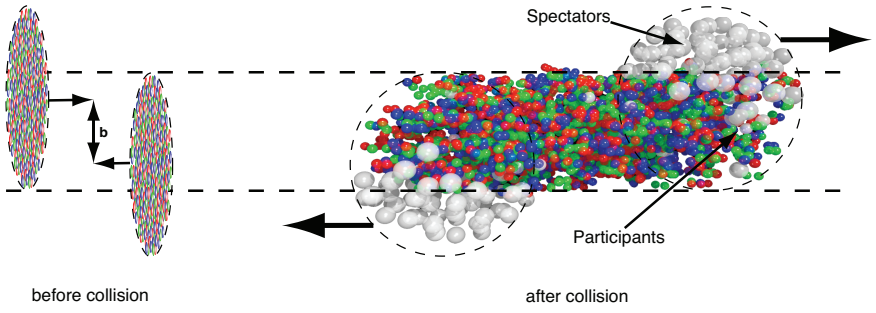

Figure 9: Left: Two heavy-ions before the collision with impact parameter b. Right: The spectators continue unaffected, while in the participant zone particle production takes place. [19]

The impact parameter b, which is defined as the distance between the center of two nuclei, determines the overlap area of the two colliding nuclei. The degree of overlap, called 'centrality', is defined as a function of the impact parameter b [20] as:

$$c_b \equiv \frac{1}{\sigma_{\text{inel}}} \int_0^b P_{\text{inel}}\left(b'\right) 2\pi b' db' \tag{7}$$

where σ_{inel} is the inelastic nucleus-nucleus cross section and $P_{\text{inel}}(b)$ is the probability of inelastic collision with impact parameter b. Experimentally, the impact parameter cannot be measured. Therefore, centrality is determined with a cumulative distribution of a

measurable observable n, such as particle multiplicity:

$$c \equiv \int_{n}^{\infty} P\left(n'\right) dn' \tag{8}$$

where the probability distribution of c is constant by construction: $P(c) = 1$ for $0 < c < 1$. Fig. 10 shows the mean multiplicity value of n ($\bar{n}$), which was calculated by the $\mathrm{T_R ENT_O}$ model [21], versus centrality defined by impact parameter (c_b). In the inset of this figure, $\bar{n}(c_b)$ is compared to $n(c)$, the multiplicity which gives the centrality c defined by Eq. 8. It is found that $\bar{n}(c_b)$ deviates from $n(c)$ only above $n \sim 170$ which corresponds to 1.5% centrality. Fig. 11 shows an example of the experimentally determined centrality with ALICE V0 scintillation counters. The centrality is estimated via a Glauber fit of the multiplicity distribution measured by the V0 detector and described by a Negative Binomial Distribution (NBD) [22].

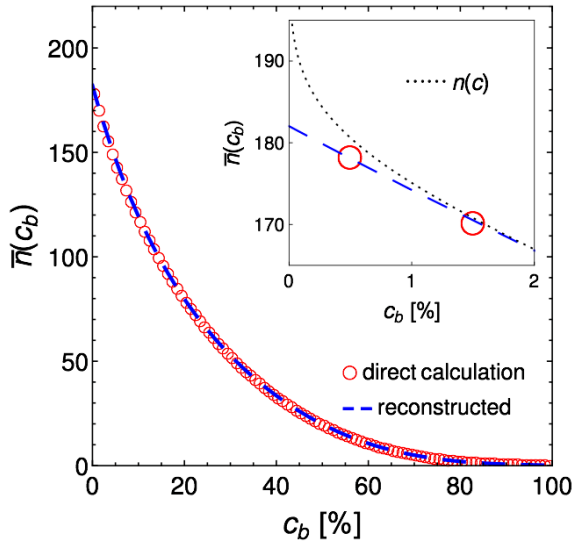

Figure 10: Mean value of n ($\bar{n}$) versus b-centrality (c_b) [20]. Red circles show result calculated directly by binning $\mathrm{T_R ENTo}$ results in c_b and dashed blue line shows result reconstructed from the fit of $P(n)$. The inset shows a zoom of the most-central collisions, where $\bar{n}(c_b)$ is compared to $n(c)$ (dotted line).

As illustrated in Fig. 9, nucleons from the two incoming nuclei can be grouped into 'participants', the nucleons which took part in the collision and 'spectators' which did not. For a given impact parameter, the Glauber model [24] gives the number of participants

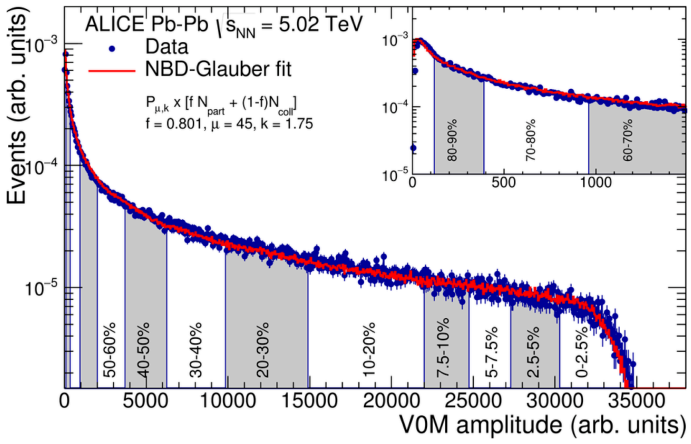

Figure 11: Distribution of the sum of amplitudes in the ALICE V0 scintillators. The distribution is fitted with the NBD-Glauber fit shown as a line [23]

N_{part}, the number of nucleon-nucleon collisions N_{coll}, and the distributions of participants and spectators.

Nucleons inside nucleus A are distributed with a density ρ by a Wood-Saxon distribution:

$$\rho_A(r) = \frac{\rho_0}{1 + \exp\left(\left[r - R_A\right]/a\right)} \tag{9}$$

where r is the distance of each nucleon from the center of nucleus A, R_A is the radius of nucleus A, and a is a diffusion parameter at the surface of nucleus A. ρ_0 is a normalization parameter so that $\int d^3r \rho_A(r) = A$.

The nuclear thickness function at impact parameter b, which represents the number of nucleons of nucleus A per unit area is given as:

$$T_A(\mathbf{b}) = \int dz \rho_A(z, \mathbf{b}) \ . \tag{10}$$

Then, the number of participants N_{part} can be expressed as:

$$\begin{aligned} N_{\text{part}} &= \int d\mathbf{s} T_A(\mathbf{s}) \left(1 - \exp\left(-\sigma_{\text{inel}}^{\text{NN}} T_B(\mathbf{s})\right)\right) \\ &+ \int d\mathbf{s} T_B(\mathbf{s} - \mathbf{b}) \left(1 - \exp\left(-\sigma_{\text{inel}}^{\text{NN}} T_A(\mathbf{s})\right)\right) \end{aligned} \tag{11}$$

where $\sigma_{\text{inel}}^{\text{NN}}$ is the inelastic nucleon-nucleon cross section.

The number of nucleon-nucleon collisions N_{coll} is:

$$N_{\text{coll}} = A\, B\, T_{AB}(b) \sigma_{\text{inel}}^{\text{NN}} \tag{12}$$

where A, B are the mass number of nucleus A and B, and $T_{AB}(\mathbf{b}) = \int T_A(\mathbf{s})T_B(\mathbf{s}-\mathbf{b})d^2s$. From geometry considerations, the number of collisions $N_{\rm coll}$ scales as:

$$N_{\rm coll} \propto N_{\rm part}^{4/3} \ . \tag{13}$$

1.4.3 Collision geometry - Event plane

The plane defined by the beam axis and the impact parameter vector is called the 'reaction plane' (RP). In non-central heavy-ion collisions, the participants form an almond-like shape (Fig. 12). As presented in Ref. [25], [26], the n^{th}-order participant eccentricity ε_n is defined as:

$$\varepsilon_n = \sqrt{< r^2 \cos n\phi_{\rm part} >^2 + < r^2 \sin n\phi_{\rm part} >^2} / < r^2 > \tag{14}$$

where $r = \sqrt{x^2+y^2}$ and $\phi_{\rm part}$ is the azimuthal angle of a participant. The n^{th}-order participant event plane (EP) $\psi_n^{\rm part}$, which directs the minor axis of the n-gon formed by the participants region, is defined as:

$$\psi_n^{\rm part} = \frac{\text{atan}\,2\left(\left\langle r^2 \sin\left(n\phi_{\rm part}\right)\right\rangle, \left\langle r^2 \cos\left(n\phi_{\rm part}\right)\right\rangle\right) + \pi}{n} \ . \tag{15}$$

In this thesis, the direction of RP and ψ_n are referred to as 'in-plane' and the direction perpendicular to RP and ψ_n as 'out-of-plane'. In reality, the reaction plane reconstructed from the participant distribution is expressed as the superposition of the n^{th}-order event planes since the number of nucleons is finite. The 2^{nd}-order event plane corresponds to the elliptic shape of the initial collision geometry which is mainly derived from the almond-like shape of the overlap region between the two nuclei. Higher-order event planes are sensitive to the fluctuations of the initial geometry of participants. For the measurements in Pb-Pb collisions discussed in this thesis, jets are measured w.r.t the 2^{nd}-order event plane to study the initial collision geometry dependence of parton energy loss. For example, a stronger parton energy loss is expected in the out-of-plane direction than in-plane since the mean parton path-length is longer out-of-plane. The in-medium parton energy loss is described in Sec.1.5 and experimental results of the EP dependence of energy loss are shown in Sec 1.7.1.

1.5 Parton energy loss in the hot and dense QCD medium

In the QGP, the energy of hard scattered partons is suppressed due to collisional and/or radiative in-medium energy loss. As a result, the observed jet properties are modified in comparison with QCD vacuum. For example, jet $p_{\rm T}$ suppression and jet shape modifications have been observed [5, 28]. This phenomenon is called 'jet quenching'. Measurement of jet quenching in heavy-ion collisions allows to probe the entire evolution since jets originate from the hard scattered partons in the early stages of the collision. Since the elementary

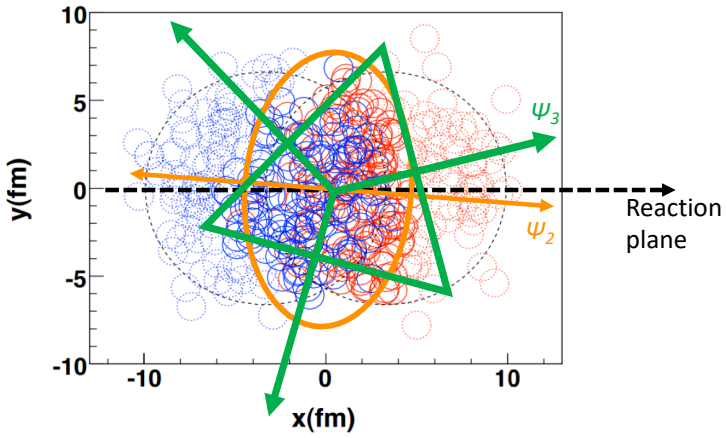

Figure 12: A sketch of a non-central Pb-Pb collision. Colored circles are nucleons. Solid circles are participants and dashed circles are spectators. The original figure which was made with a Glauber Monte-Carlo simulation was taken from Ref. [27]. The reaction plane and 2^{nd}, 3^{rd}-order event plane (ψ_2, ψ_3) are displayed.

processes involved in jet production can be described within pQCD, jets are well calibrated probes of the QGP properties.

In this section, an overview of the collisional and radiative energy loss mechanisms in QGP is given.

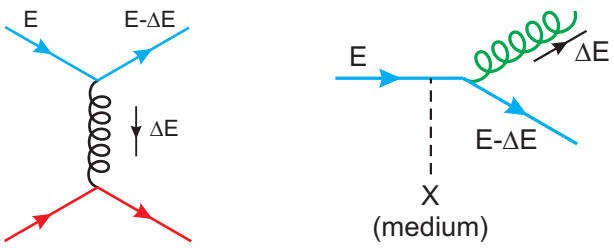

Figure 13: Left: Feynman diagram of collisional parton energy loss. Right: Feynman diagram of radiative parton energy loss. [8]

Collisional energy loss

The collisional energy loss induced by elastic scatterings within the medium dominates

at low momentum [8]. The average energy loss per parton scattering is given as:

$$\left\langle \Delta E_{coll}^{1scat} \right\rangle \approx \frac{1}{\sigma T} \int_{m_D^2}^{t_{max}} t \frac{d\sigma}{dt} dt \tag{16}$$

where $\frac{d\sigma}{dt}$ is the cross section and t the momentum transfer. m_D is the Debye mass equal to $(4\pi\alpha_s)^{1/2}T \sim 1$ GeV at leading order pQCD calculation. The lower limit of the integrated momentum transfer t_{min} is given by the QGP Debye mass squared as:

$$t_{\min} = m_D^2(T) \sim 4\pi\alpha_s T^2 \left(1 + N_f/6\right) \ . \tag{17}$$

The upper limit t_{max} is given as:

$$t_{\max} = s \sim ET \ . \tag{18}$$

With Eq. 16, 17, 18 and taking the dominant contribution to the t-differential parton-parton elastic cross section,

$$\frac{d\sigma}{dt} \approx C_i \frac{4\pi\alpha_s^2(t)}{t^2}, \text{ with } \alpha_s(t) = \frac{12\pi}{(33 - 2n_f)\ln\left(t/\Lambda_{QCD}^2\right)} \tag{19}$$

where C_i is the colour factor for individual parton combinations ($C_i = 9/4, 1, 4/9$ for gg, gq, qq respectively). Thus, the collisional energy loss per unit length for light partons is given as:

$$-\left.\frac{dE_{\rm coll}}{dl}\right|_{q,g} = \frac{1}{4} C_R \alpha_s(ET) m_D^2 \ln\left(\frac{ET}{m_D^2}\right) \ . \tag{20}$$

The collisional energy loss per unit length for heavy-quarks is given as:

$$-\left.\frac{dE_{\rm coll}}{dl}\right|_{Q} = -\left.\frac{dE_{\rm coll}}{dl}\right|_{q} - \frac{2}{9} C_R \pi T^2 \left[\alpha_s\left(M^2\right) \alpha_s(ET) \ln\left(\frac{ET}{M^2}\right)\right] \tag{21}$$

where $C_R = 4/3, 3$ for quarks and gluons respectively. The collisional energy loss is linear with parton path-length and depends only logarithmically on the initial parton energy.

Radiative energy loss

The radiative energy loss which dominates at high momentum is induced by inelastic scatterings within the medium [8]. It is defined by analogy with the single or double-differential photon and gluon *Bremsstrahlung* spectrum and leads as follows:

$$\Delta E_{rad}^{1scat} = \int^{E} \omega \frac{dI_{rad}}{d\omega} d\omega, \text{ or } \Delta E_{rad}^{1scat} = \int^{E} \int^{k_{T,max}} \omega \frac{d^2 I_{rad}}{d\omega dk_\perp^2} d\omega dk_\perp^2 \tag{22}$$

where $\omega, k_\perp$ are the energy and transverse momentum of the radiated photon and gluon.

The total energy loss for incoherent scatterings can be expressed as $\Delta E^{tot} = N \cdot \Delta E^{1scat}$, where the opacity $N = L/\lambda$, L being the thickness of the medium and λ is

the mean free parton path-length. The energy loss per unit length, or stopping power of the medium, is given as:

$$-\frac{dE}{dl} = \frac{\left\langle \Delta E^{tot} \right\rangle}{L} \ . \tag{23}$$

In QCD, when considering partons traversing a QGP, the initial parton energy is suppressed mainly by in-medium multiple gluon emission. The radiated gluon spectrum $\omega dI_{\rm rad}/d\omega$ is calculated starting from the DGLAP splitting functions in the vacuum [29]:

$$P_{\rm q\to qg}(z) = C_F \frac{\left[1+(1-z)^2\right]}{z}, \text{ and } P_{\rm g\to gg}(z) = C_A \frac{\left[1+z^4+(1-z)^4\right]}{z(1-z)} \tag{24}$$

where the color factor $C_A = 3$, $C_F = 4/3$ and the fraction of the energy of the parent parton taken by the radiated gluon is given by $z = \omega/E$. A medium-induced enhancement of radiation is taken into account by modifying Eq. 24. The resulting spectrum of radiated gluons, $\omega dI_{\rm rad}/d\omega \propto P_{q,g\to g}(\omega/E)$, has been computed by various groups with various approximations. In several models, all medium-induced modifications are often represented by the 'transport coefficient' parameter $\hat{q} \equiv m_D^2/\lambda$. For a thin medium ($L \ll \lambda$), gluon bremsstrahlung (gluonsstrahlung) is calculated by the Bethe-Heitler (BH) expression while for the thick medium case ($L \gg \lambda$) the gluonsstrahlung is affected by the Landau-Pomeranchuk-Migdal (LPM) regime. In the LPM regime, the soft or hard gluon emission cases are differentiated according to the characteristic gluonsstrahlung energy $\omega_c = \frac{1}{2}\hat{q}L^2$. The basic QCD radiative energy loss is eventually expressed as:

" Bethe-Heitler " (BH) regime ($L \ll \lambda$)

$$\omega\frac{dI_{rad}}{d\omega} \approx \alpha_s \hat{q} L^2/\omega \Longrightarrow \Delta E_{rad}^{BH} \approx \alpha_s \hat{q} L^2 \ln\left(E/\left(m_D^2 L\right)\right) \tag{25}$$

"Landau-Pomeranchuk-Migdal" (LPM) regime ($L \gg \lambda$)

$$\omega\frac{dI_{rad}}{d\omega} \approx \alpha_s \left\{ \begin{array}{ll} \sqrt{\hat{q}L^2/\omega} \\ \hat{q}L^2/\omega \end{array} \right. \Longrightarrow \Delta E_{rad}^{LPM} \approx \alpha_s \left\{ \begin{array}{ll} \hat{q}L^2 & (\omega < \omega_c) \\ \hat{q}L^2 \ln\left(E/\left(\hat{q}L^2\right)\right) & (\omega > \omega_c) \end{array} \right) \ . \tag{26}$$

1.6 Experimental results of jet measurements in pp collisions

In this section, experimental results of jet measurements in pp collisions are summarized.

1.6.1 Charged jet cross section

Production cross section of jets is dominantly determined by perturbatively calculable partonic hard scattering cross sections. As mentioned in Sec.1.2, the jet cross section is

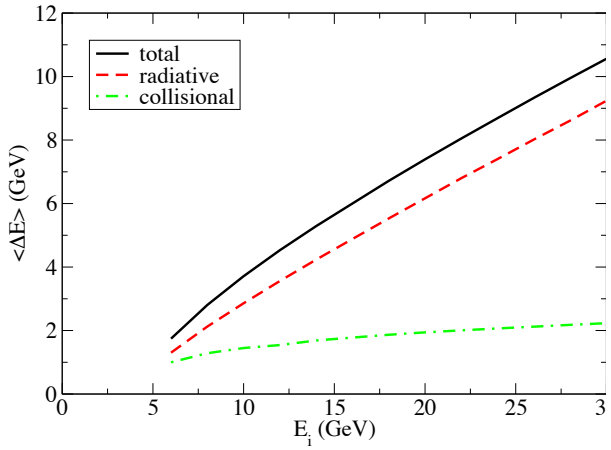

Figure 14: Comparison of the average energy loss of light quarks by radiative and collisional energy losses at RHIC energy [8]

expressed as the product of a perturbative part and non-perturbative part. Thus, measurements of jets in simple collision system, such as pp collisions, represent a good test of predictive capabilities of pQCD-based models. The charged jets differential production cross sections are shown in Fig. 15 for $R = 0.2$, 0.4 and 0.6 jets in pp collisions at $\sqrt{s} = 7$ TeV measured by the ALICE Collaboration. Here, 'charged jets' means jets reconstructed with charged hadrons only and 'R' is the jet resolution parameter, also called the jet radius. The results are compared to pQCD calculations at Leading-Order (LO) accuracy. None of the predictions give a quantitative description of the data over entire kinematic range.

Higher-order pQCD calculations give better description of the full jet cross section measurement [31]. Here, 'full jets' means jets reconstructed with neutral particles in addition to charged hadrons. Therefore, charged jet cross section may also be well described by higher-order pQCD calculations.

1.6.2 Charged jet cross section ratio

The ratio of charged jet production cross sections for $R = 0.2$, 0.4 and 0.6 jets in pp collisions at $\sqrt{s} = 7$ TeV is shown in Fig. 16. These ratios are sensitive to the jet radial shape. According to these results, high-p_{T} jets are more collimated. These results are quantitatively well described by LO pQCD calculations except in the low p_{T} region of the $\sigma(R = 0.2)/\sigma(R = 0.6)$ ratio.

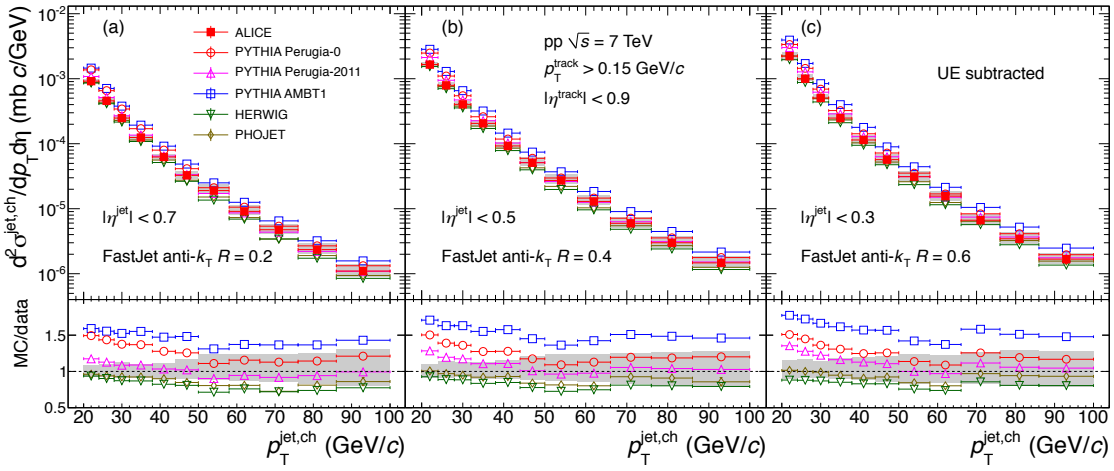

Figure 15: The differential production cross section for charged jets reconstructed with R = 0.2,0.4 and 0.6 measured by ALICE. The results are compared to some LO pQCD-based predictions [30]

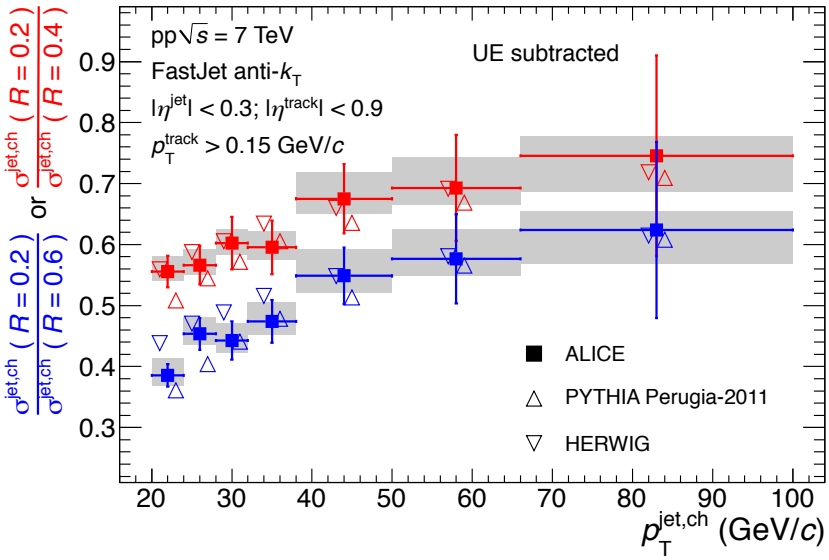

Figure 16: The ratio of charged jet cross section reconstructed with R = 0.2, 0.4 and 0.6 measured by ALICE. The results are compared to some LO pQCD-based predictions [30]

1.7 Experimental evidence of nuclear matter effects

In this section, experimental evidence of nuclear matter effects is summarized.

1.7.1 Jet quenching

Owing to in-medium partonic energy loss, as described in Sec. 1.5, jet quenching is observed in ultrarelativistic heavy-ion collisions. One of the most remarkable observation of jet quenching observation was made in di-hadron correlation measurements performed by the STAR Collaboration at RHIC (see Fig. 17).

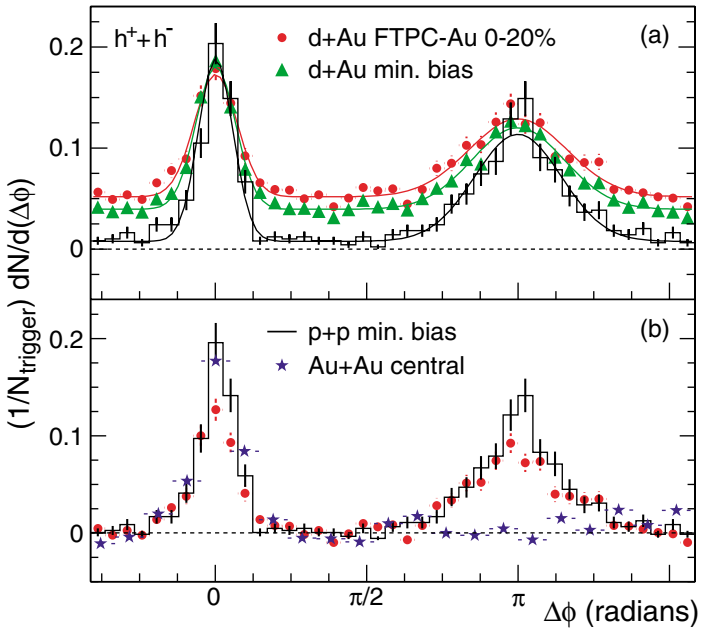

Figure 17: Two-particle correlation in pp, d+Au and Au+Au collisions at $\sqrt{s_{\rm NN}} = 200$GeV for $4 < p_{\rm T}^{trig} < 6$ GeV and $2 < p_{\rm T}^{assoc} < p_{\rm T}^{trig}$ [32].
(a): Comparison of efficiency corrected two-particle azimuthal distributions for minimum-bias and central d+Au collisions, and for pp collisions.
(b): Comparison of two-particle azimuthal distributions for central d+Au collisions, minimum-bias pp collisions and for central Au+Au collisions.

The observed back-to-back two-peak structure can be ascribed to the di-jet topology in QCD vacuum. Near-side ($\Delta\phi \sim 0$) and away-side ($\Delta\phi \sim \pi$) peaks are observed in pp and d+Au collisions as expected. However, in central Au+Au collisions, the away-side peak is not visible anymore. This result, which are interpreted as the suppression of the away-side jet production due to medium-induced parton energy loss, is considered to be the evidence

of QGP formation in central ultrarelativistic heavy-ion collisions.

The nuclear modification factor ($R_{\rm AA}$) is one of the proven observables to quantify nuclear matter effects in heavy-ion collisions. With $N^{\rm AA}$ and $N^{\rm pp}$ being the yields of a given observable with certain $p_{\rm T}$ in AA and pp collisions respectively, $R_{\rm AA}$ is defined as the ratio of the yield in AA collisions over the yield in pp collisions scaled by the number of binary nucleon-nucleon collisions $N_{\rm coll}$:

$$R_{\rm AA} = \frac{dN^{\rm AA}/dp_{\rm T}}{\langle N_{\rm coll}\rangle\, dN^{\rm pp}/dp_{\rm T}} = \frac{dN^{\rm AA}/dp_{\rm T}}{\langle T_{\rm AA}\rangle\, d\sigma^{\rm pp}/dp_{\rm T}} \ . \tag{27}$$

$R_{\rm AA} = 1$ means no observation of nuclear effects and departure of $R_{\rm AA}$ from unity suggests some nuclear matter effects. Particularly, the suppression of hard processes, such as high-$p_{\rm T}$ hadrons or jets, suggests medium-induced partonic energy loss. Note that $R_{\rm AA} = 1$ does not always mean the absence of nuclear matter effects since other effects could balance leading to $R_{\rm AA} = 1$.

Fig. 18 (Left) shows the single hadron $R_{\rm AA}$ measured by several experiments at various collision energies. A strong collision energy dependent suppression of high-$p_{\rm T}$ hadrons is observed.

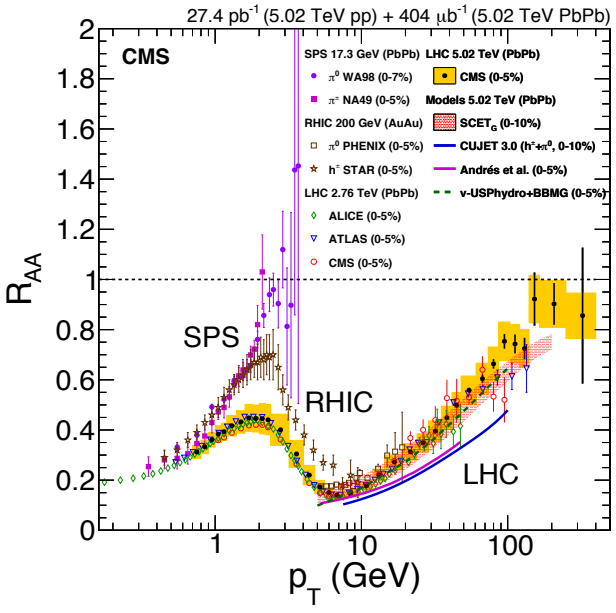

Figure 18: Comparison of the $R_{\rm AA}$ for neutral pions (π^0), charged hadrons ($h^{\pm}$), and charged particles in central heavy-ion collisions at SPS, RHIC, and LHC [33].

On the other hand, the $R_{\rm AA}$ of high-$p_{\rm T}$ photons and Z, W bosons is consistent with

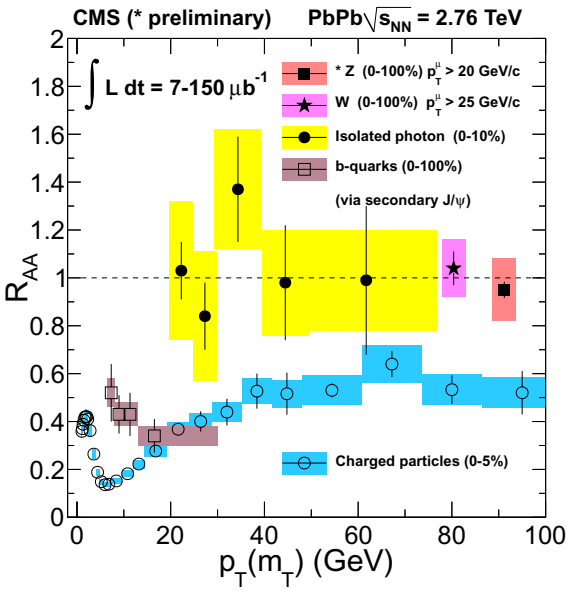

Figure 19: The R_{AA} for direct photons, $W^{\pm}$ and Z^0 bosons, charged particles and b-quarks measured from secondary J/ψ particles [34].

unity as shown in Fig. 19. This result supports the hypothesis that in-medium energy loss of color-charged partons is the dominant mechanism at work in high-p_{T} hadron suppression, color-less particles are not being suppressed in the medium.

Although single high-p_{T} hadron measurements provide valuable insights into partonic energy loss, they were shown to have severe limitations by imposing a strict separation between medium effects and jet fragmentation in their interpretation. Conversely, the measurement of fully reconstructed jets mitigates the fragmentation bias and allows to assess the parton kinematics which is required for a detailed description of jet-medium interaction. The large production cross section of high-p_{T} jets at LHC energies allows to measure fully reconstructed jets in heavy-ion collisions.

The jet R_{AA} measured at LHC are shown in Fig. 20. The jet R_{AA} shows a strong suppression which grows with the collision centrality.This result emphasizes in-medium parton path-length dependence of jet quenching. In order to study the path-length dependence of jet suppression, the jet v_2 in Pb-Pb collisions at $\sqrt{s_{\mathrm{NN}}} = 2.76$ TeV was measured by the ALICE and ATLAS Collaborations as shown in Fig. 21. These results show a positive jet v_2, which suggests a larger jet yield in-plane than out-of-plane. This behaviour is quantitatively consistent with the JEWEL model predictions [37].

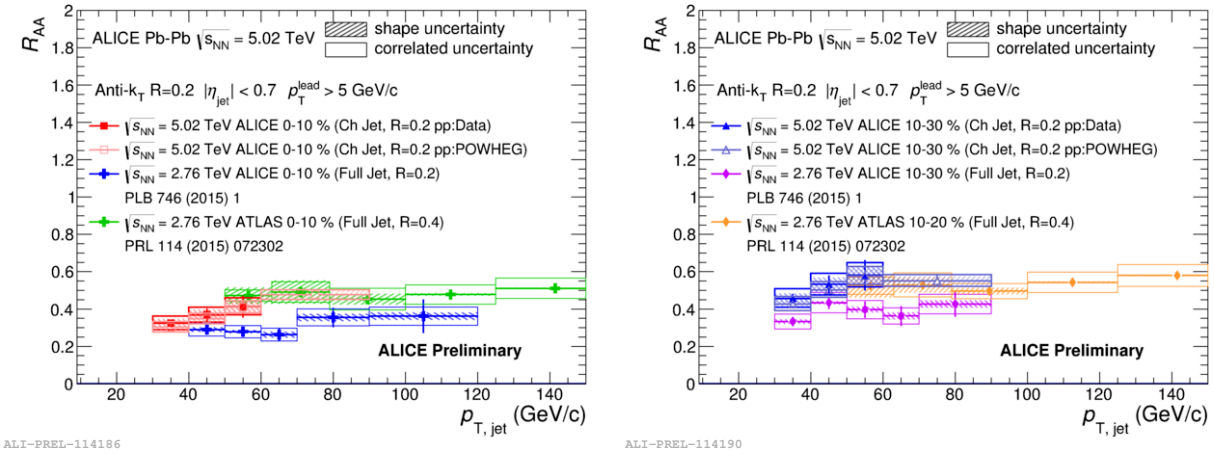

Figure 20: Comparison of charged jet R_{AA} in Pb-Pb collisions at $\sqrt{s_{\mathrm{NN}}} = 5.02$ TeV measured by ALICE and full jet R_{AA} in Pb-Pb collisions at $\sqrt{s_{\mathrm{NN}}} = 2.76$ TeV measured by ATLAS [35]
Left: Centrality range is 0-10% Right: Centrality range is 10-30%

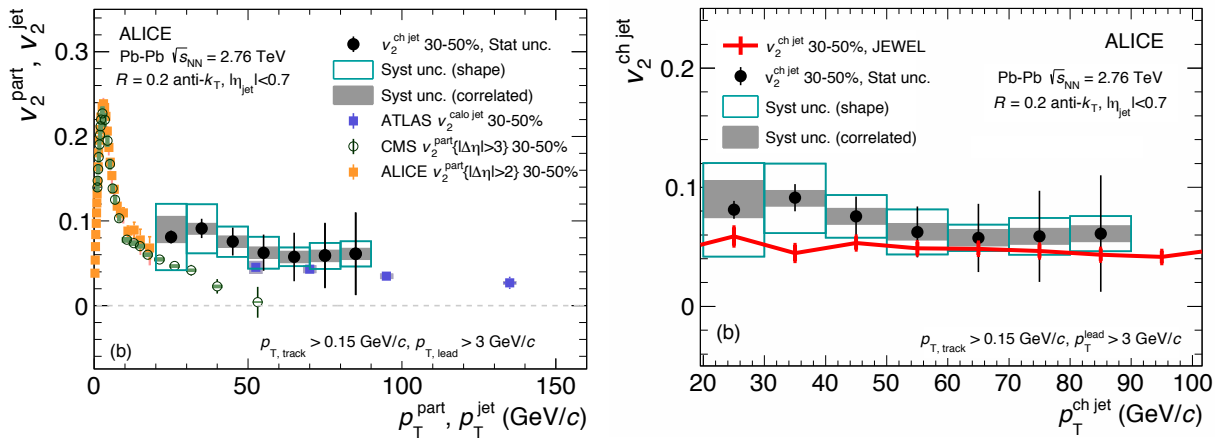

Figure 21: Left: Elliptic flow coefficient v_2 of charged particles (orange, green) and R = 0.2 full jets measured within $|\eta| < 2.1$ (blue) superimposed on the results of R = 0.2 charged jets v_2 within $|\eta| < 0.7$ (black) in mid-central collisions (30-50%)
Right: v_2 of $R = 0.2$ charged jets predicted by JEWEL (red) for mid-central collisions (30-50%) compared to data (black). [36]

Another interesting question related to jet quenching is the understanding of how the suppressed parton energy is transported and re-distributed in the medium. The jet radial profile in pp and Pb-Pb collisions at $\sqrt{s_{\rm NN}} = 5.02$ TeV measured by the CMS Collaboration with jet-track(-hadron) correlations is shown in Fig. 22,

$$\mathrm{P}(\Delta \mathrm{r}) = \frac{1}{\delta \mathrm{r}} \frac{1}{N_{\rm jets}} \Sigma_{\rm jets} \Sigma_{\rm tracks \in (\Delta r_a, \Delta r_b)} p_{\rm T}^{\rm track}, \Delta \mathrm{r} < 1 \tag{28}$$

where r is the distance between the jet axis and the tracks. These results show the suppression of high-$p_{\rm T}$ hadrons in Pb-Pb collisions in comparison with the pp case. An enhancement of low-$p_{\rm T}$ hadrons can also be observed at large radial distance from jet axis, suggesting that the parton energy deposited in the medium is re-distributed in the form of low-$p_{\rm T}$ hadrons at large radial distance. A model calculation including a hydrodynamical medium response (see [38] and references therein) reproduced this observation as shown in Fig. 23, where the jet shape is given by:

$$\rho(\Delta \mathrm{r}) = \frac{\mathrm{P}(\Delta \mathrm{r})}{\sum_{\rm jets} \sum_{\rm tracks} p_{\rm T}^{\rm track}} \tag{29}$$

and P(Δr) is defined in Eq. 28. This result suggests that the understanding of the non-static hydrodynamical evolution of the medium will be important to reveal the mechanism of the energy flow in the medium.

1.7.2 Azimuthal anisotropic flow

In non-central ultrarelativistic heavy-ion collisions, a QGP is formed in the almond shaped overlap region of the two colliding nuclei as shown in Fig. 24 (Left). During the collective expansion of the QGP, this initial spatial anisotropy of the overlap region is converted into a momentum anisotropy of the final state hadrons as shown in Fig. 24 (Right).

The azimuthal momentum distribution of final-state particles in an event can be expanded into a Fourier series as:

$$\frac{dN}{d\phi} \propto 1 + 2\left(v_1 \cos\left[\phi - \psi_{r,n}\right] + v_2 \cos\left[2\left(\phi - \psi_{r,n}\right)\right] + \cdots\right) \tag{30}$$

where ϕ is the azimuthal angles of the particles in momentum space and N is the yield of particles. ψ_r and ψ_n are the azimuthal angle of the reaction plane and the n^{th}-order event plane respectively. The Fourier coefficients of n^{th}-order harmonics are expressed as:

$$v_n = \left\langle \cos\left[n\left(\phi - \psi_{r,n}\right)\right] \right\rangle \ . \tag{31}$$

Non-zero v_n means an anisotropic particle production with respect to $\psi_{r,n}$. The azimuthal anisotropic particle production in heavy-ion collisions was observed as shown in Fig. 25.

This phenomenon is currently understood as a hydrodynamical evolution of the medium

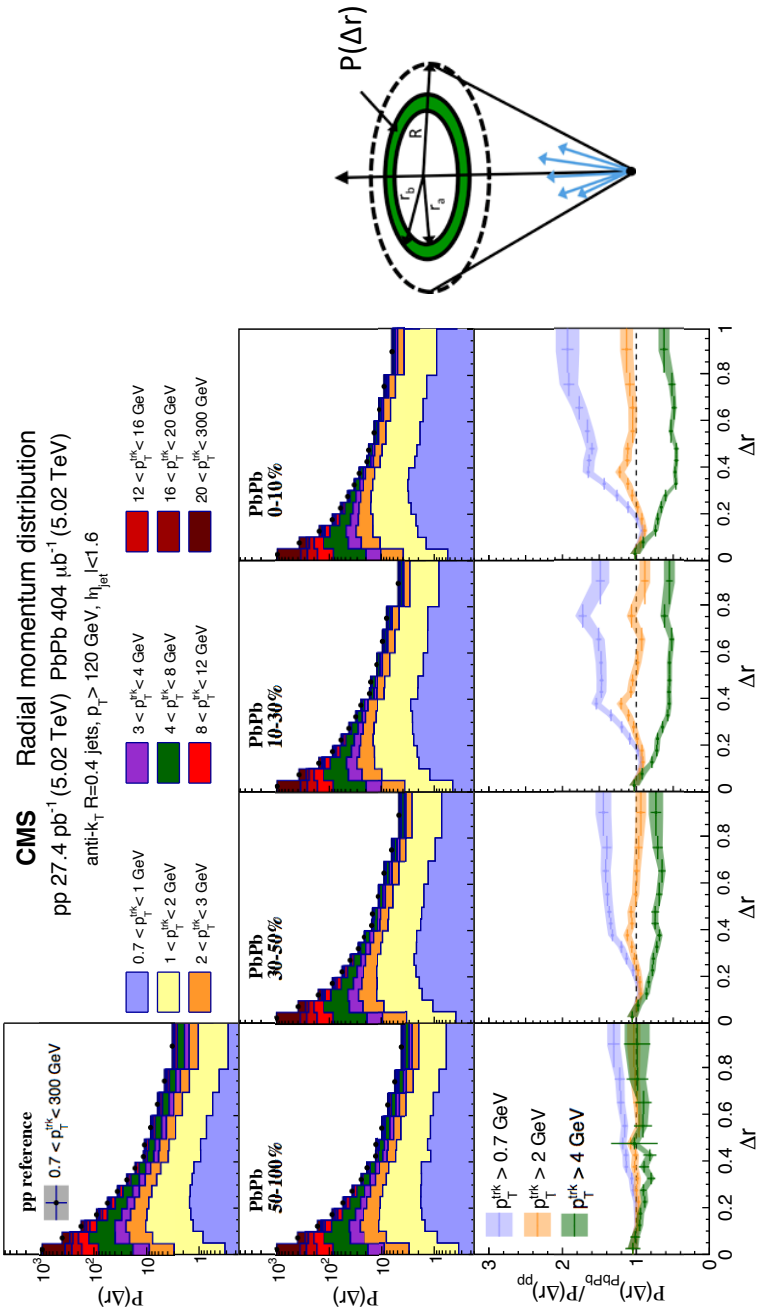

Figure 22: The radial jet momentum distribution P(Δr) of jets in pp (top left) and Pb-Pb (middle row) collisions at $\sqrt{s_{\mathrm{NN}}} = 5.02$ TeV. The bottom row shows the ratio between Pb-Pb and pp data for the several intervals of $p_{\mathrm{T}}^{\mathrm{track}}$. The shaded bands are systematic uncertainties [28]

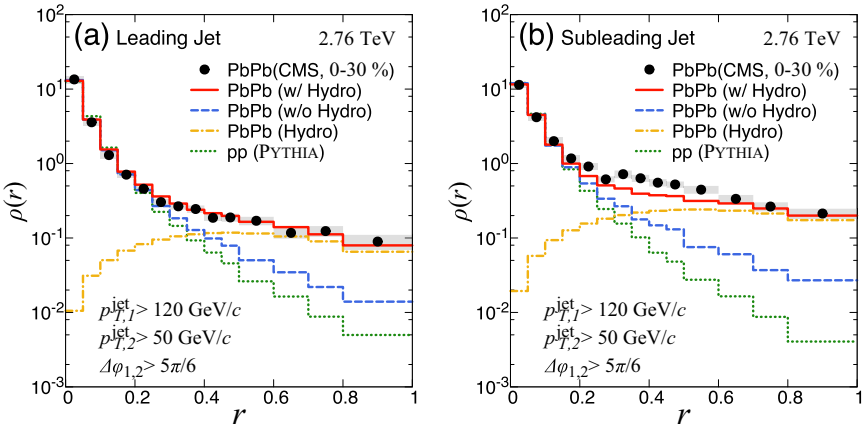

Figure 23: Jet shape function for (a) leading and (b) sub-leading jets in dijet events in central Pb-Pb and in pp collisions at $\sqrt{s_{\mathrm{NN}}} = 2.76$ TeV [38]

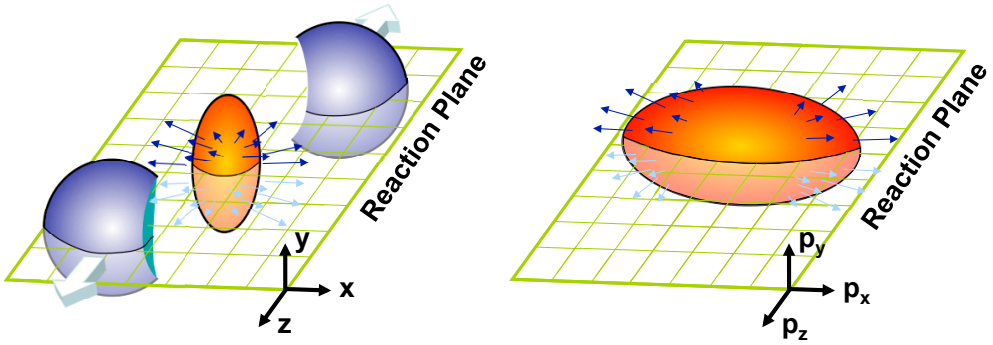

Figure 24: Left: Initial overlap of two nuclei in an off-center collision in coordinate space. Right: Collective elliptic expansion into the direction of reaction plane in momentum space.

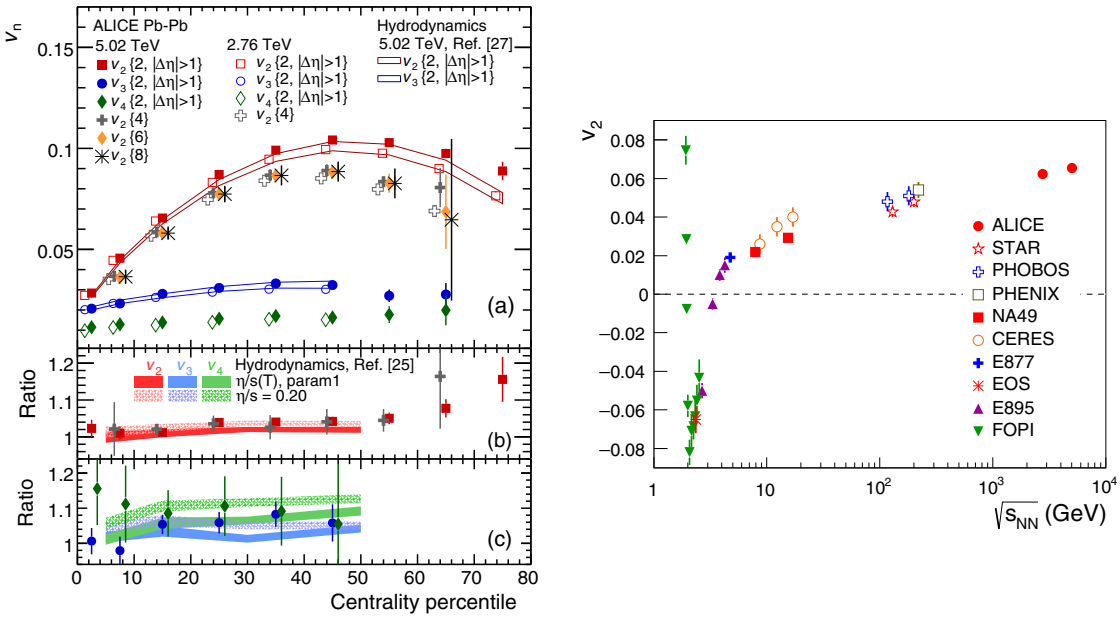

Figure 25: The experimental results of anisotropic flow coefficients (v_n) [39]
Left: (a) Anisotropic flow coefficients v_n integrated over $0.2 < p_{\mathrm{T}} < 5.0$ GeV/c, as a function of event centrality for the two-particle and multi-particle cumulant methods.
(b),(c) are the ratios to the various hydrodynamic calculations. Ref.[25],[27] in the figure correspond to Ref.[40],[41] respectively.
Right: Comparison of the integrated elliptic flow results from various experiments at various collision center-of-mass energies.

dominantly driven by the pressure gradient in the medium. The difference of the pressure gradient in-plane and out-of-plane leads to the azimuthal anisotropy of particle production. This process mainly plays a role for soft (low-p_{T}) particle production and is the main source of background for jet measurements in heavy-ion collisions.

1.8 Thesis motivation

In this thesis, measurements of charged jets in pp and Pb-Pb collisions at $\sqrt{s_{\rm NN}} = 5.02$ TeV with the ALICE detector are performed for a twofold purpose.

1.) As a test of pQCD calculation

Jet production, which is one of the most fundamental QCD processes, is calculable within perturbation theory as mentioned in Sec. 1.1.1, 1.2. However, final-state observables include non-perturbative effects which can only be extracted experimentally. Some models are often combined with pQCD calculations to account for these non-perturbative effects. In the studies discussed in this thesis, the measurements of charged jet differential production cross sections for $R = 0.2$, 0.3, 0.4 and 0.6 in pp collisions at $\sqrt{s} = 5.02$ TeV were compared to Leading-Order (LO) and Next-to-Leading-Order (NLO) pQCD-based model predictions.

2.) Exploration of jet quenching effect in ultrarelativistic heavy-ion collisions

The strength of jet suppression and the modification of jet radial profile as a function of centrality have been measured in Pb-Pb collisions at $\sqrt{s_{\rm NN}} = 5.02$ TeV. These studies control in-medium mean path-length of partons to a certain extent by selecting centrality. However, the mean path-length largely fluctuates even in mid-central collisions of similar centralities due to the large eccentricities of the initial collision system which leads to large differences of parton path-length in-plane and out-of-plane. In this thesis, $R = 0.2$ charged jet production in mid-central (30-50%) Pb-Pb collisions at $\sqrt{s_{\rm NN}} = 5.02$ TeV is measured w.r.t the 2^{nd}-order event plane. A measurement of charged jet v_2 is performed to study the path-length dependence of jet energy suppression in-plane and out-of-plane. Charged jet-hadron correlations ares also studied to measure the modification of jet radial profiles and jet energy suppression and redistribution.

Chapter 2 Experimental apparatus

2.1 The Large Hadron Collider (LHC)

The Large Hadron Collider (LHC) is the world's largest particle accelerator [42]. It was built at CERN for the purpose of high-energy particle and nuclear physics experiments. So far, proton-proton (pp), proton-lead (pPb), lead-lead (Pb-Pb), and xenon-xenon (Xe-Xe) collisions were provided by the LHC.Maximum center-of-mass energies of $\sqrt{s} = 13$ TeV in pp collisions and $\sqrt{s_{\mathrm{NN}}} = 5.02$ TeV in Pb-Pb collisions were achieved.

The LHC is the last ring of the CERN accelerator complex as illustrated in Fig. 26.

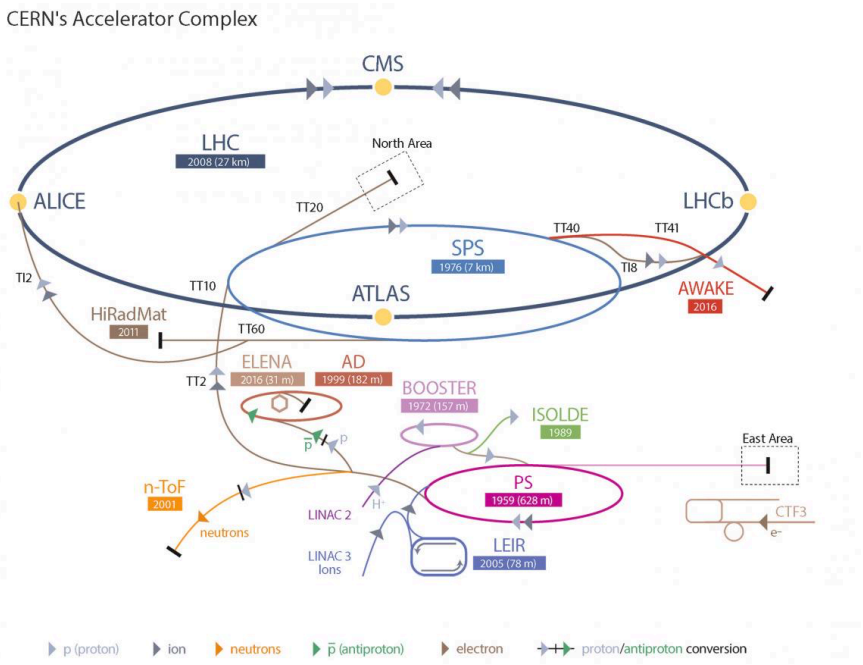

Figure 26: Sketch of the CERN accelerator complex

To reach the LHC energies, the particle beams are pre-accelerated before injection into the LHC ring by an accelerator chain which consists of LINAC, storage ring, and synchrotron. The proton beams are accelerated by LINAC 2 up to an energy of 50 MeV and the lead-ion beams are accelerated by LINAC 3 up to an energy of 4.2 MeV/n. Proton beams are then

transfered to the PS Booster (synchrotron) and lead-ion beams to the LEIR (Low-Energy Ion Ring). The beam energy is then pushed up to 25 GeV by the Proton Synchrotron (PS). Finally, the beams are subjected to further acceleration at the Super Proton Synchrotron (SPS) up to 450 GeV and then injected to the LHC ring.

2.2 The ALICE detector complex

The ALICE detector consists of different types of sub-detectors dedicated to various purposes as shown in Fig. 27.

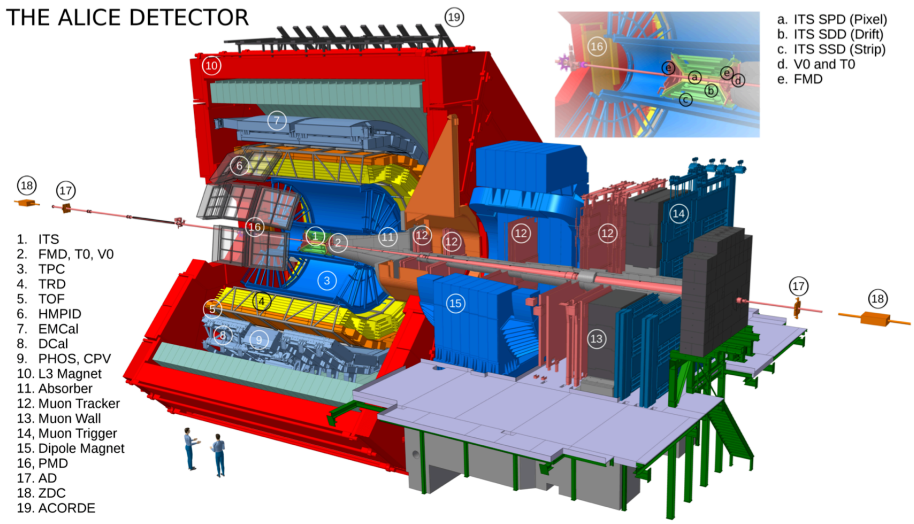

Figure 27: The ALICE detector at the LHC Run2

The ALICE detectors are classified into three groups:

- 'Central barrel detectors' for particle tracking and electro-magnetic calorimetry ($|\eta| < 1$).
- 'Muon arm' for muon tracking ($-4 < \eta < 2.5$).
- 'Global detectors' for event triggering, event characterization and classifications.

In the following sections of this chapter, the ALICE detectors used for the jet measurements are introduced.

2.2.1 VZERO (V0) detector

The VZERO (V0) detector is a multi-segmented scintillation counter. The V0 detector is one of the global detectors installed in the forward and backward rapidity regions.The

V0 covering the forward region is called 'V0A' ($2.8 < \eta < 5.1$) and the one covering the backward region is called 'V0C' ($-3.7 < \eta < -1.7$).

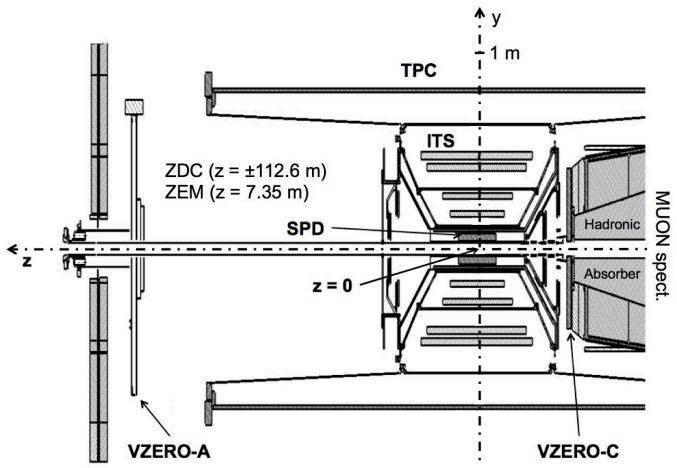

Figure 28: The installation of V0 detector in ALICE. [43]

Each of the V0 arrays is segmented in 4 rings and each ring is divided into 8 sections as shown in Fig. 29.

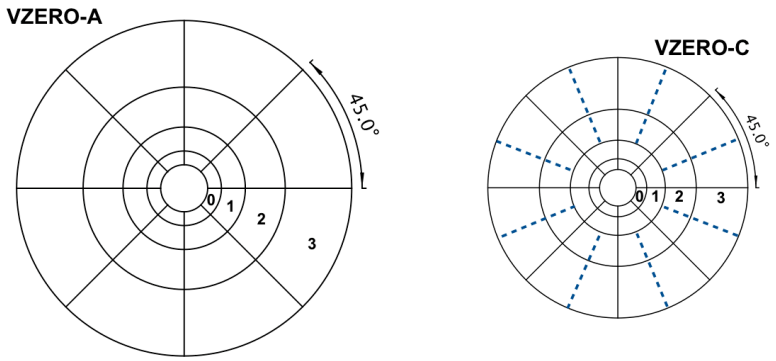

Figure 29: Sketch of V0A and V0C array segmentation. The scintillator thicknesses are 2.5 and 2 cm respectively. The two segments separated by dashed lines are connected to the same PMT [43].

The design of the V0 elementary cells is shown in Fig. 30. Wave-Length-Shifting (WLS) fibers are embedded on both faces of the V0A segment or glued along their radial edges for V0C rings 0-1.

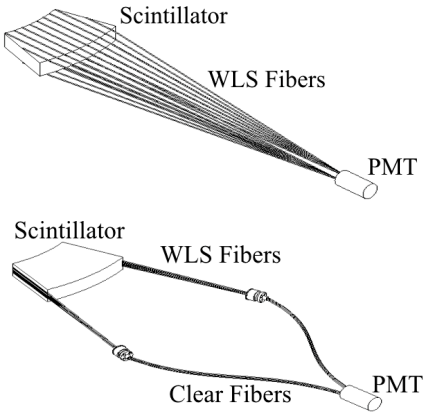

Figure 30: Design of the V0A and V0C rings 0-1 (bottom) elementary cell. Two scintillating sets (scintillator and WLS fibers) are connected to a single PMT through four clear fiber beams for V0C rings 2-3. [43]

In this study, the V0 detector is used for the following purposes:

- Minimum-bias trigger (coincidence between V0A and V0C).
- Multiplicity measurement for centrality determination
  The resolution of the centrality determination is 0.5-2% as shown in Fig. 31.
- Measurement of event plane from the multiplicity distribution
  The event plane resolution is shown in Fig. 32. For example, the resolution for ψ_2 (R_2 in Fig. 32) is about 60-80% in mid-central Pb-Pb collisions.
- Pileup removal.

2.2.2 Inner Tracking System (ITS)

The Inner Tracking System (ITS) consists of 3 different types of silicon detectors.

The innermost two layers of the ITS are 'Silicon Pixel Detectors' (SPD). Each SPD module is composed of a two-dimensional sensor matrix of reverse-biased silicon diodes. The pixel size is 50 μm (intheplaneperpendiculartothebeamaxis, $r\phi$)$\times$425 μm (alongthebeamaxis, z). A pair of hits on each of the two SPD layers is called a 'tracklet' and is used for primary vertex determination and multiplicity measurements. SPD also contribute to the L0 trigger for pileup removal.

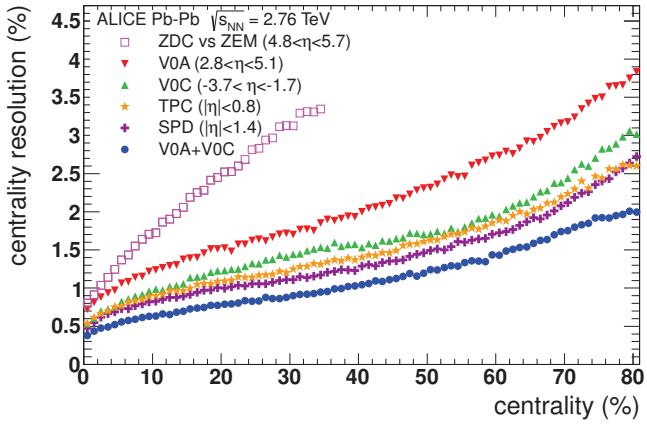

Figure 31: Resolution of centrality measured by ALICE detectors in Pb-Pb collisions at $\sqrt{s_{\mathrm{NN}}}$ = 2.76 TeV. [44]

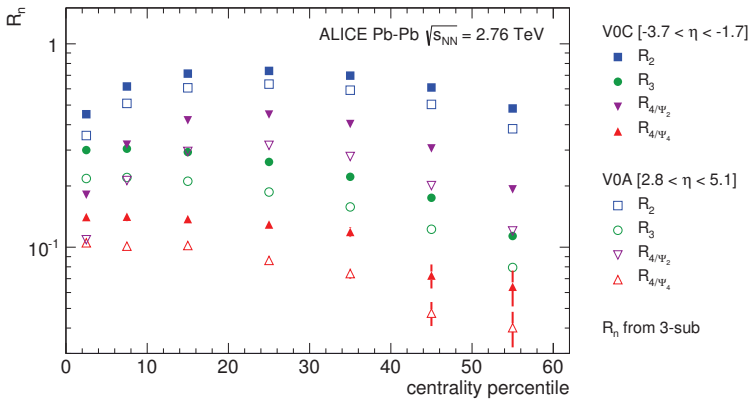

Figure 32: Event plane resolution measured by V0A and V0C in Pb-Pb collisions at $\sqrt{s_{\mathrm{NN}}}$ = 2.76 TeV. [44]

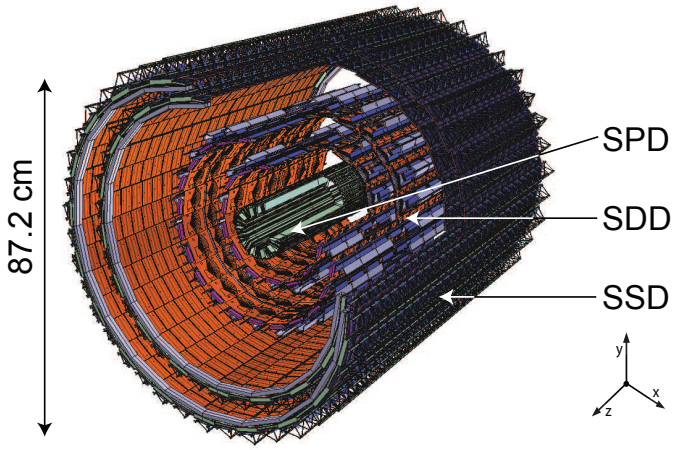

Figure 33: Sketch of ITS [45].

The intermediate two layers are 'Silicon Drift Detectors' (SDD). The sensitive area of an SDD sensor is split into two drift regions by a central cathode. Each drift region is equipped with anodes for charge collection. Two-dimensional position can be reconstructed with the drift time of the charges and the Anode segmentation.

The outer two layers are 'Silicon Strip Detectors' (SSD). Each SSD module consists of a 1536 strip double-sided silicon sensor connected through aluminum-kapton micro-cables to twelve front-end chips. The pitch of the strips is 95 μm and the P-N-side stereo angle is 35 mrad. It allows a two-dimensional measurement of the track position with a good ghost hit rejection

In this study, the ITS is used for the following purposes:

- Primary vertex reconstruction
  Primary vertex (the position of the initial collision) is reconstructed from SPD tracklets. The primary vertex reconstructed with SPD is referred to as $z^{\mathrm{SPD}}_{\mathrm{vertex}}$. The resolution of the primary vertex reconstruction is of the order of 150-200 μm in pp collisions as shown in Fig. 34.

- Background event removal
  An event is identified as a pileup event and rejected if multiple vertices are reconstructed within this event. Additionally, out-of-bunch pileup events are rejected based on online-vs-offline SPD Fast-OR (FO) correlations.

- Tracking

Charged particle tracks are reconstructed from hits in the ITS over the pseudo-rapidity range $|\eta| < 0.9$. The reconstructed ITS track segments are combined with TPC (see Sec.2.2.3) track segments to improve the tracking resolution and reduce fake tracks.

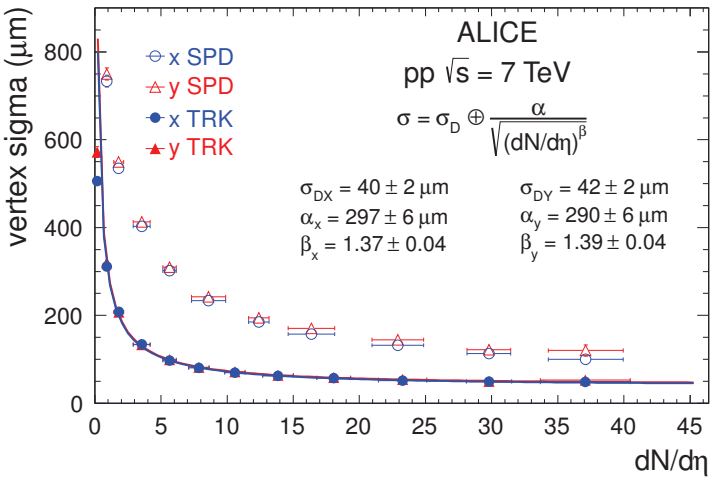

Figure 34: Resolution of vertex determination [44].

2.2.3 Time Projection Chamber (TPC)

The Time Projection Chamber (TPC) is the main charged particle tracking detector of the ALICE experiment. A sketch of the TPC is shown in Fig. 35 (left). The TPC is 510 cm along the beam axis and has a diameter of 469 cm providing a drift volume of 88 m^3. The drift volume is filled with a light sensitive medium (gas). The gas mixture during LHC Run1 was Ne(90%):CO_2(10%) and changed to Ar(90%):CO_2(10%) during LHC Run2 to enable a more stable detector response. The drift volume is divided into two regions by a central electrode made of aluminized mylar foil which generates a drift field of 400 V/cm. The maximum drift time is about $\sim$ 100 μs. The TPC has 557,568 readout pads and corresponding front-end electronics (FEE) readout channels.

In this study, the TPC is used for the following purposes:

- Tracking

  Charged particle tracks are reconstructed from x-y hits on the readout pads and the drift time for z position. The full tracking range of the TPC covers a pseudorapidity range of $|\eta| < 0.9$. The reconstructed tracks are combined with ITS track segments

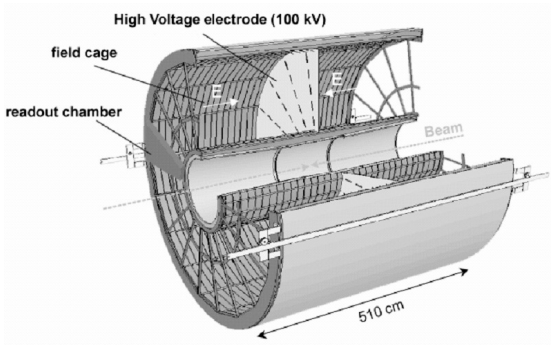

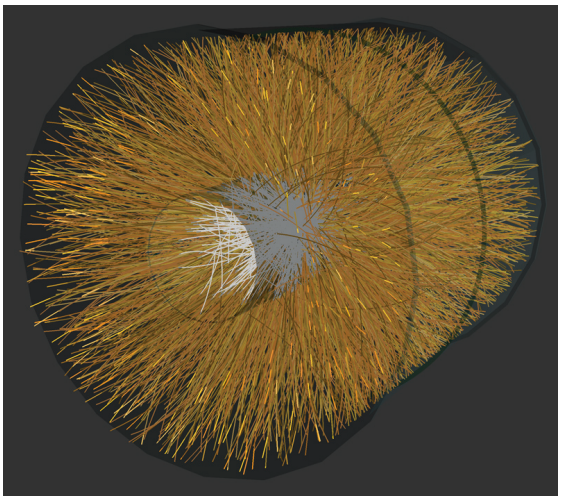

Figure 35: Left: Sketch of TPC [46]. Right: 3D view of TPC tracks reconstructed from a central Pb-Pb collision [47]

to improve tracking resolution and to reduce fake tracks. The tracking efficiency is shown in Fig. 36 and the tracking p_{T} resolution is shown in Fig. 37

- Primary vertex reconstruction
  Primary vertex is reconstructed from ITS+TPC tracks. In this thesis, the z coordinate of the primary vertex reconstructed with ITS+TPC tracks is referred to as $z_{\mathrm{vertex}}^{\mathrm{track}}$ and hereafter 'primary vertex' refers to the track vertex hereafter otherwise not specified. The resolution of the primary vertex position in the transverse plane is of the order of 100 μm as shown in Fig. 34.

- Background event removal
  Out-of-bunch pileup events are rejected if the number of TPC clusters is too large in comparison with the number of primary tracks.

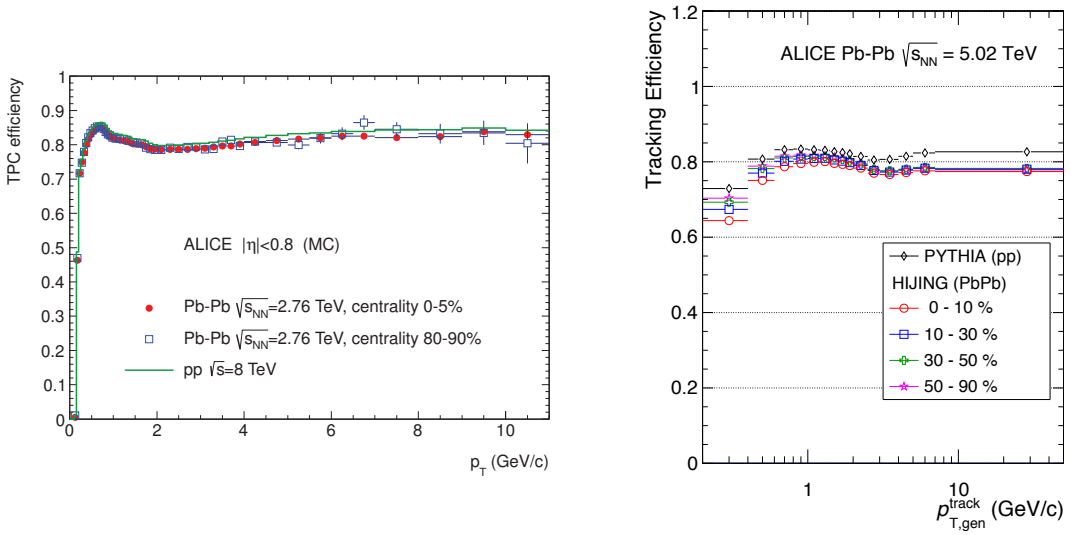

Figure 36: Left: Tracking efficiency with only TPC [44], Right: Tracking efficiency with ITS+TPC [5].

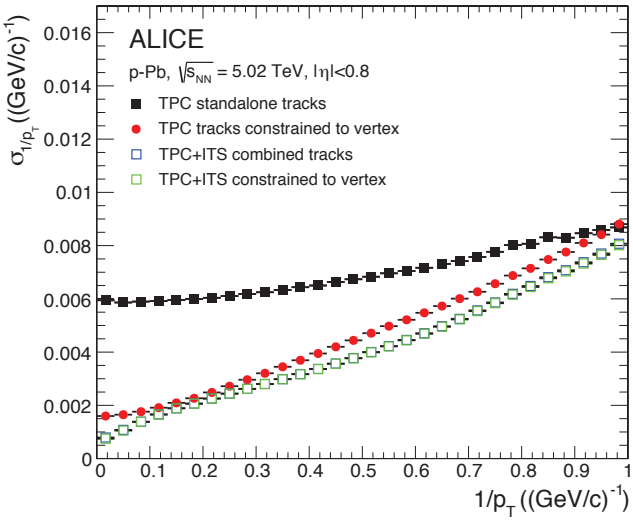

Figure 37: Tracking p_{T} resolution [44].

2.2.4 Electromagnetic Calorimeters (EMCal, DCal, PHOS)

ALICE has three electromagnetic calorimeters located inside the central barrel: EMCal (ElectroMagnetic Calorimeter), DCal (Di-jet Calorimeter) and PHOS (PHOton Spectrometer).

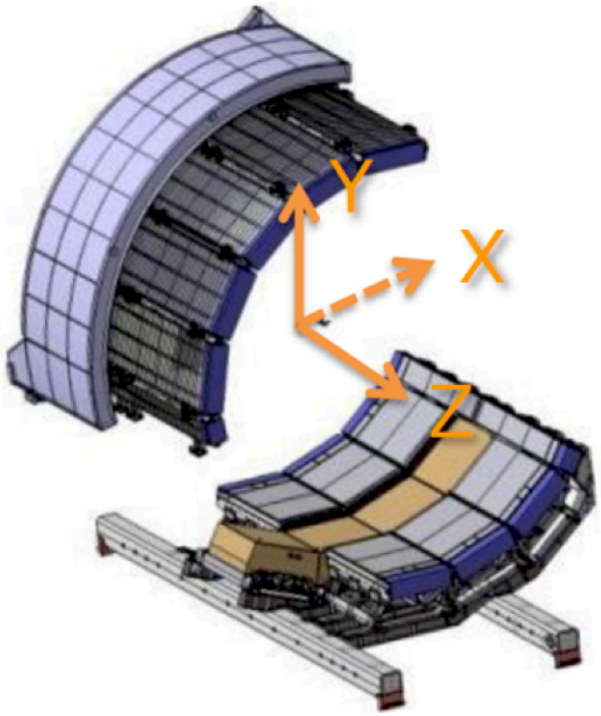

Figure 38: Electromagnetic calorimeters (EMCal, DCal and PHOS) [5].

EMCal and DCal are sampling calorimeters. Their main purpose is to measure the high-energy photons and electrons. The size of each cell, which consists of 77 lead-scintillator layers, is $(\Delta x, \Delta y, \Delta z) = (60\text{ mm}, 60\text{ mm}, 246\text{ mm})$ and $(\Delta\phi, \Delta\eta) = (0.0143, 0.0143)$. An EMCal and DCal cell is called a 'tower'. 4 towers compose 1 'module'. 12 modules compose 1 'strip' and 24 strips compose 1 'Super Module' (SM) as shown in Fig. 39 (left).

EMCal is composed of $10+2\times(1/3)$ SMs and DCal is composed of $6\times(2/3)+2\times(1/3)$ SMs. EMCal and DCal are made of $10+2\times(1/3)$ SMs and $6\times(2/3)+2\times(1/3)$ SMs respectively, corresponding to a total of 12,288 EMCal towers and 5,376 DCal towers. The coverage of EMCal is $80^\circ < \phi < 187^\circ$, $|\eta| < 0.7$ while DCal covers $260^\circ < \phi < 327^\circ$, $|\eta| < 0.7$.

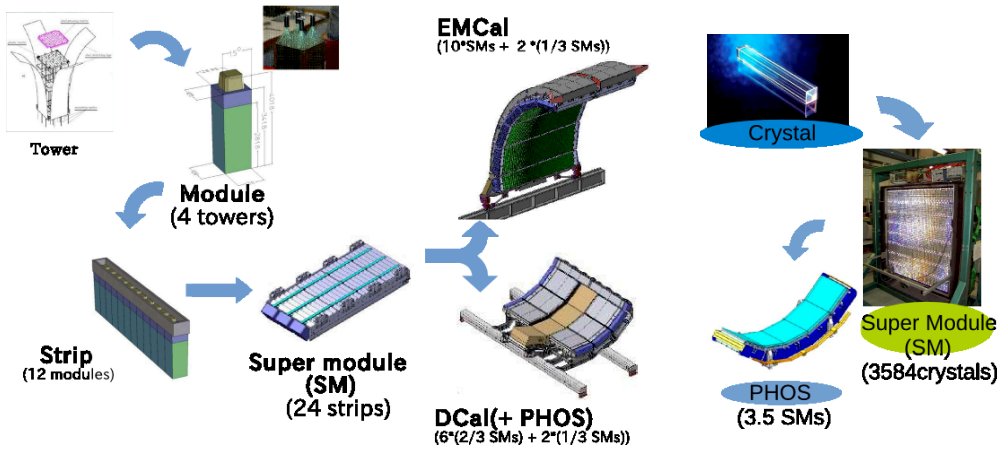

Figure 39: Components of EMCal, DCal (left) and PHOS (right).

PHOS is an homogeneous type of electromagnetic calorimeter. The main purpose of PHOS is to measure the photons with high energy and position resolution. Each cell is made of lead tungstate ($PbWO_4$) with the size of $(\Delta x, \Delta y, \Delta z) = (22\text{ mm}, 22\text{ mm}, 180\text{ mm})$ and $(\Delta\phi, \Delta\eta) = (0.004, 0.004)$. Each PHOS cell is called 'crystal'. 3584 crystals compose 1 SM. PHOS consists of 3.5 SMs and covers $250° < \phi < 320°$, $|\eta| < 0.13$.

Chapter 3 describes the upgrade of the calorimeter trigger system for high-p_{T} photon, electron, and jet identification carried out during LHC Long-Shutdown 1 (LS1, 2013-2015) and in the early period of LHC Run2 (2015).

2.2.5 Time-Of-Flight (TOF) detector

Multigap-Resistive Plate Chambers (MRPC) are used for the ALICE Time-Of-Flight (TOF) detector. The main purpose of the TOF detector is to provide PID information. Fig. 40 shows the layout of MRPC module.

The whole TOF detector is segmented into 1593 strips and each strip covers 120×7.4 cm^2. The strips are mounted in 87 separate modules which are grouped into 18 sectors covering 2π in azimuth. The coverage in pseudo-rapidity is $|\eta| < 0.9$. The gas mixture is $C_2H_2F_4 : SF_6 = 97\% : 3\%$. In Pb-Pb collisions at $\sqrt{s}_{NN} = 5.02$ TeV, a time resolution of 56 ps was achieved as shown in Fig. 41.

In this study, the TOF detector is used to remove background events by the correlation of ITS+TPC and ITS+TPC+TOF tracks.

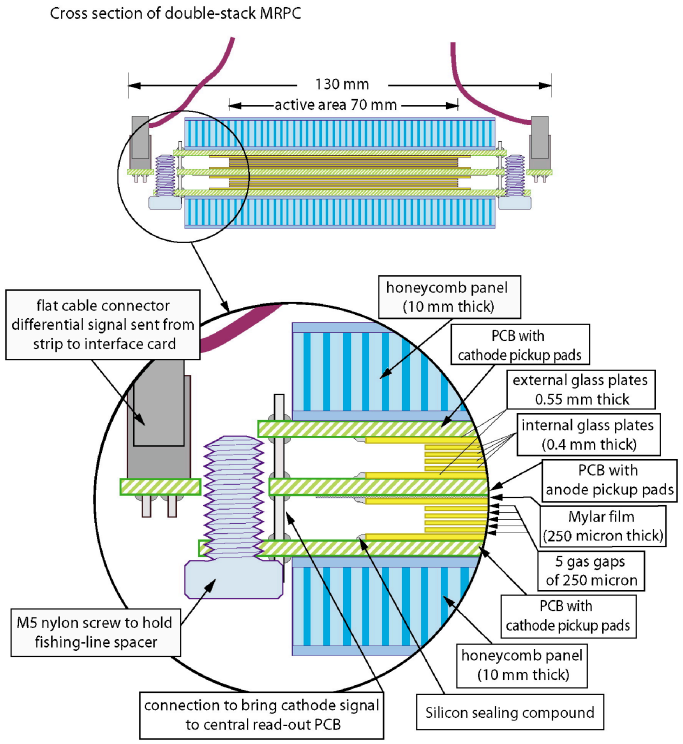

Figure 40: Cross-section of the MRPC strip for the ALICE TOF [48].

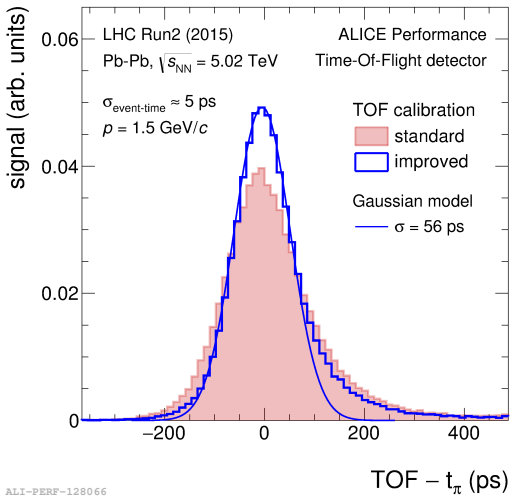

Figure 41: Time resolution of the ALICE MRPC TOF [49].

Chapter 3 Development of the Level-1 trigger system for the ALICE ElectroMagnetic Calorimeters

DCal (Sec.2.2.4) was installed during the LHC Long Shutdown 1 (LS1: 2013-2015) to enhance the jet measurement capabilities of the ALICE detector. DCal, which enlarges the acceptance opposite in azimuth of EMCal, allows di-jet measurements with fully reconstructed jets (neutral+charged constituents). This increases the acceptance by about 44% and the di-jet energy resolution (the definition is given in Fig. 42) by 10% as shown in Fig. 42.

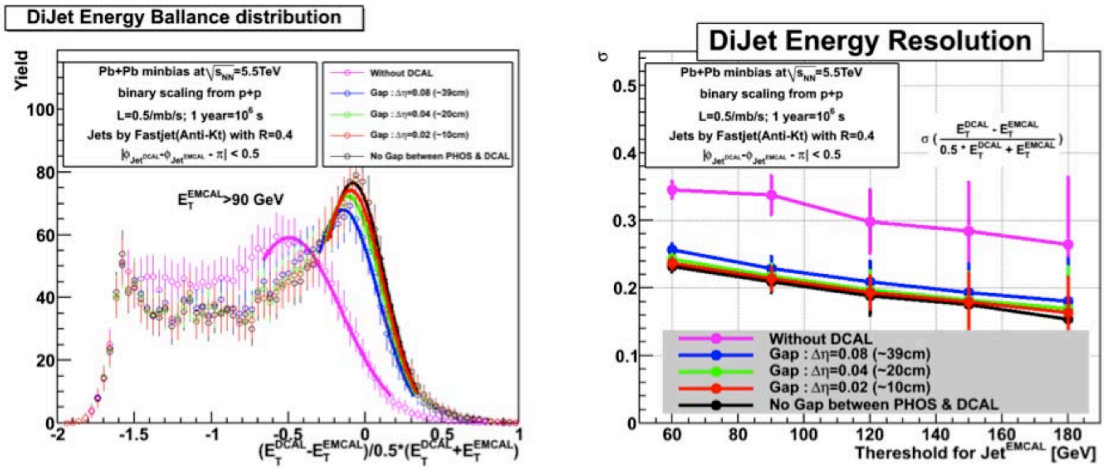

Figure 42: Di-jet energy balance and di-jet energy resolution obtained from simulation. [50]

Efficient event triggering is essential for the measurement of rare probes, such as high-p_{T} jets, In order to use effectively the limited bandwidth of the Data Acquisition (DAQ) system. In this chapter, the development of the trigger system for the ALICE calorimeters (EMCal, DCal and PHOS) is described. The firmware development and commissioning had been done in cooperation with H. Yokoyama [5].

3.1 Overview of the trigger system

The detectors can be classified into 'trigger detectors' which generate trigger signals and 'readout detectors' which collect the data. Some detectors belong to both categories.

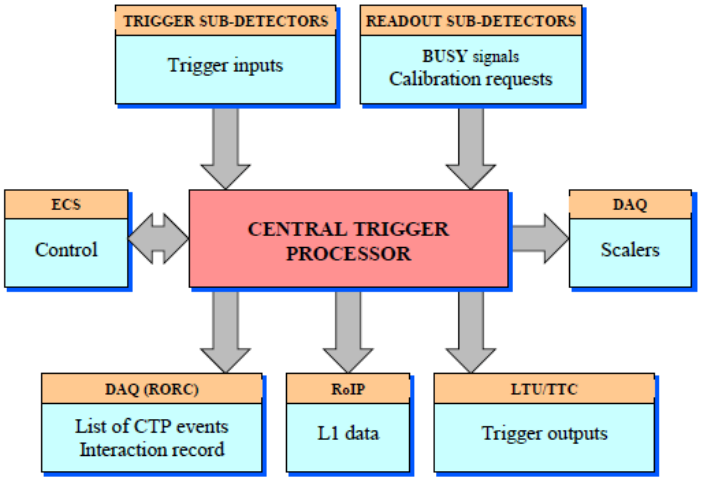

Figure 43: Overview of ALICE trigger system layout

Fig. 43 shows an overview of the the trigger system layout which is steered by the 'Central Trigger Processor' (CTP). Trigger signals from individual detectors are processed by the CTP. There are 3 hardware trigger levels: Level-0 (L0), Level-1 (L1), and Level-2 (L2). Which gradually reduce event rates. L0 triggers are issued by trigger detectors which are fast enough. L1 triggers are primarily issued by relatively slow detectors or after some data processing to select any specific events using a longer latency than that of L0. Thus, some detectors can contribute to both L0 and L1 triggers. The L0 and L1 latencies are 800 ns and 6.1 μs respectively. L2 triggers are mainly used for pileup event protection, mainly come from long drift time of TPC and its latency is $\sim$100 μs. Fig. 44 shows a typical example of trigger sequence.

EMCal, DCal and PHOS can contribute to both to L0 and L1 triggers. In this thesis, we focused on the development of the L1 trigger system, which aims at enriching data sets with high-p_{T} photons, electrons, and jets.

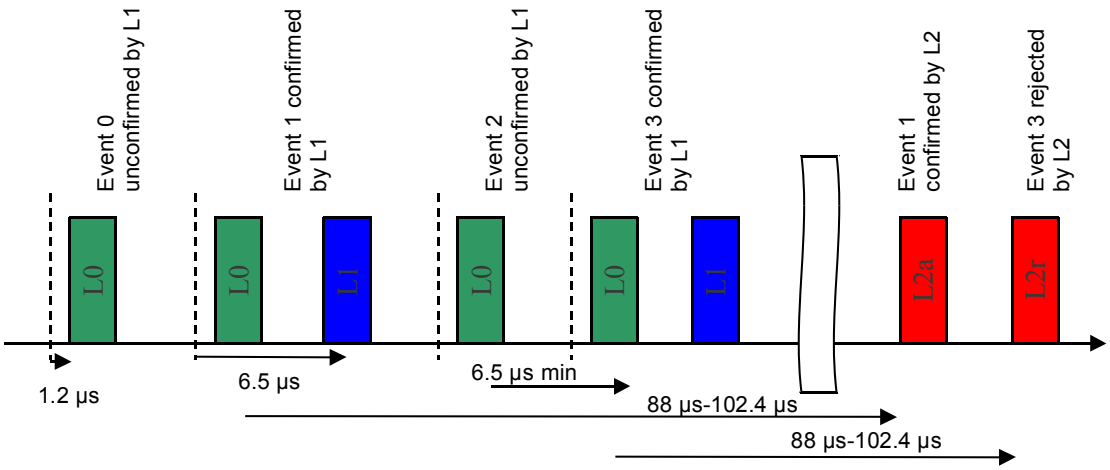

Figure 44: An example of trigger sequence [51].

Fig. 45 shows an overview of the trigger electronics configuration for EMCal, DCal, and PHOS. Fig. 46 shows the EMCal electronics chain. Raw signals from individual towers are read out by the Front-End Electronics (FEE), where the analog sum of 2×2 cells, called 'FastOR', is calculated. Signals from twelve (EMCal, DCal) or fourteen (PHOS) FEE are sent to one 'Trigger Region Unit' (TRU) where each FastOR is shaped and digitized. TRU process FastOR signals to provide the L0 decision.

The L0 and FastOR time sum (simply called 'FastOR' hereafter) signals from all TRUs are sent to the 'Summary Trigger Unit' (STU). The TRUs are connected to the STU by category 7 Ethernet cables and the signals are transmitted by Low Voltage Differential Signaling (LVDS). TRU data word length is 12 bit. When taking data, one word of header (0xAAA) is sent at the first in order to recognize that a new frame is being sent. The inter-packet, which is a known word like '0xC03', is sent for synchronization while no data are being transferred. The typical serial data frame is shown in Fig. 48. STU calculates the coincidence of L0 from TRUs and processes FastORs to provide the L1 decision. Finally, all trigger signals are sent to CTP and FastOR signals are transmitted to DAQ. These electronics mentioned above are operated based on the LHC clock of 40 MHz (corresponds to 25 ns cycle).

3.2 Trigger algorithm

The L1 trigger calculation relies on a 'sliding window' algorithm. The whole detector acceptance is scanned by a 'patch'. A trigger is fired if the sum pf the FastOR signals within

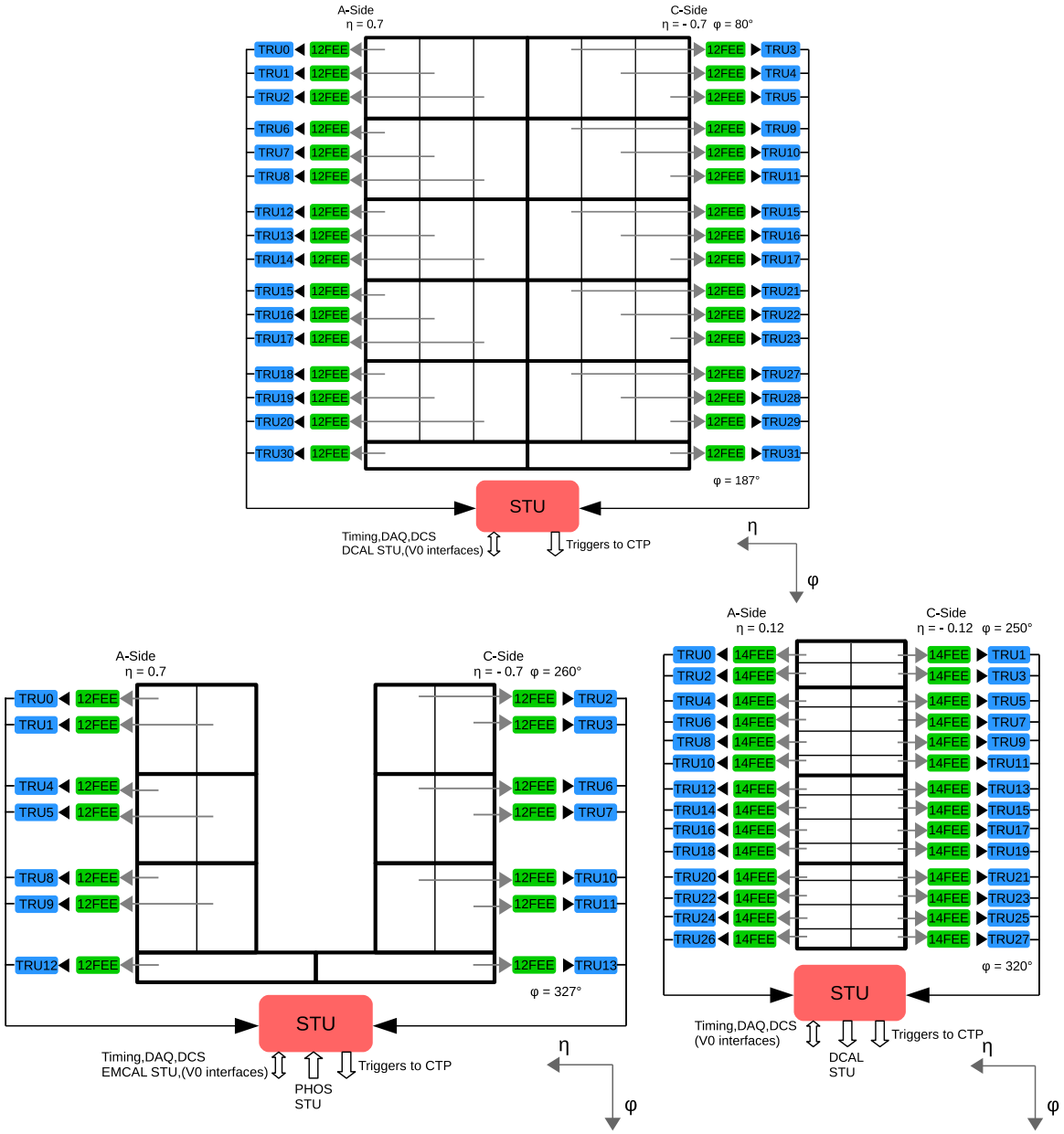

Figure 45: Overview of the configuration of the trigger electronics for ALICE EMCal (top), DCal (bottom left), and PHOS (bottom right)

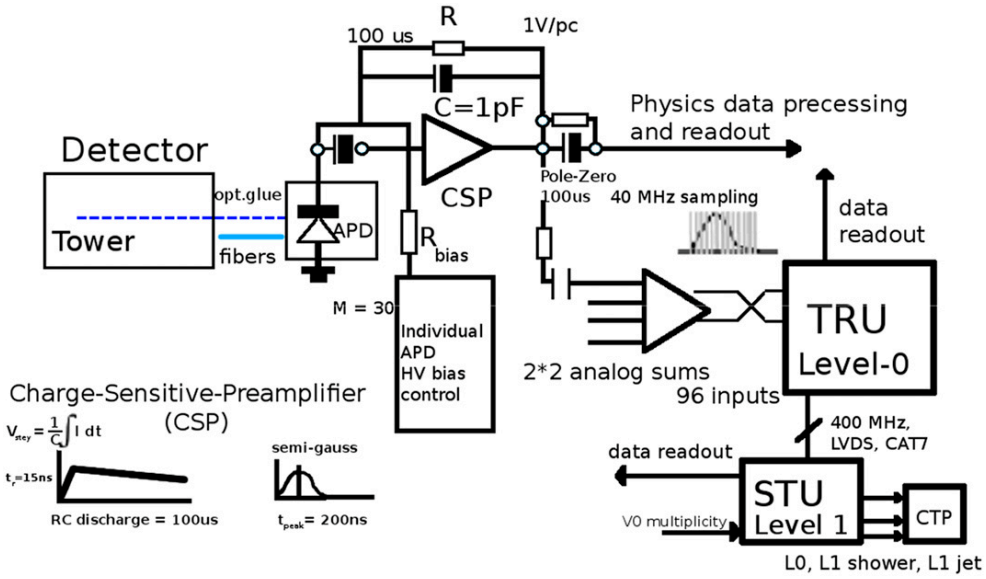

Figure 46: Flow of the signals for the trigger processing

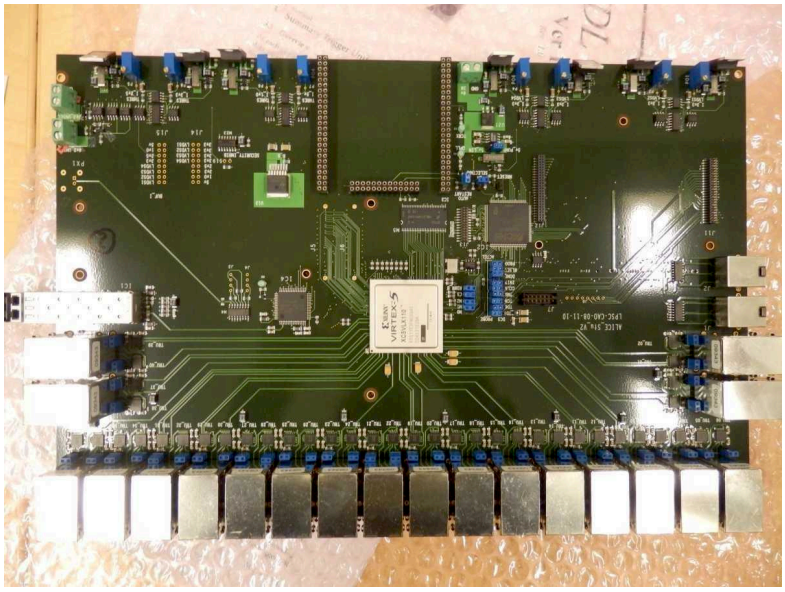

Figure 47: Top view of the Summary Trigger Unit (STU) board

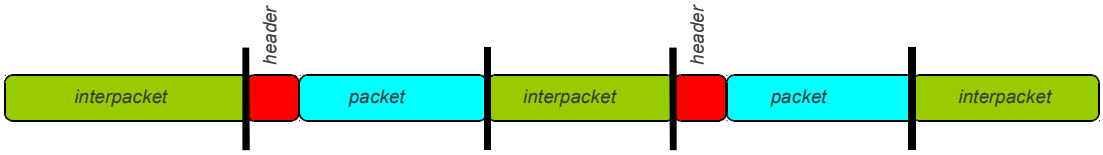

Figure 48: A typical serial data frame [51].

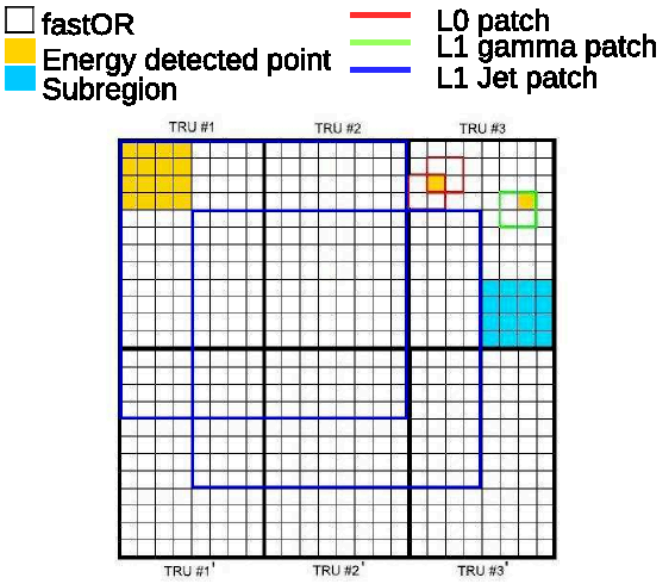

Figure 49: Trigger patches for L0 and L1 trigger. Each small square corresponds to one FastOR region

a patch exceeds a given programmable threshold. Fig. 49 shows the different trigger patch types used for L1 calculation. The patch for the L1-γ trigger, which aims at triggering on events containing a high-p_{T} photon or electron, consists of 2×2 FastORs region. 4×4 FastORs compose one 'Subregion' and the patch for the L1-Jet trigger, which aims at triggering on high-p_{T} jet events, consists of 2×2 or 4×4 subregions.

In heavy-ion collisions, the underlying event energy density is fluctuating considerably event-by-event due to the large soft background, therefore the trigger threshold should also vary on an event-by-event basis. In the trigger algorithm developed in this work, the underlying event density is estimated on the opposite-side calorimeters in azimuth and subtracted from each patch energy to deal with this event-by-event large fluctuations as follows:

1.) Calculate the summed energy in each subregion.

2.) Find the median value among all subregions

3.) Exchange the calculated median value between opposite-side calorimeters in azimuth.

4.) Subtract the median value (estimated underlying event energy) from each L1 patch.

5.) Compare the resulting L1 patch amplitude to threshold.

The flowchart of the trigger processing in EMCal and DCal is shown in Fig. 50.

A STU firmware version using the energy measured by the PHOS calorimeter in combination with DCal one has been developed. However, after some data analysis, it was discontinued due to the large energy scale difference between DCal and PHOS. Therefore, the underlying event energy estimate in heavy-ion collisions is performed without PHOS for LHC Run 2.

3.3 List of tasks carried out

a.) STU firmware upgrade

- Adaptation to the new detector configuration (Fig. 51)
  The calorimeter region readout by one TRU has been changed since the size of the DCAL SM is 2/3 of the EMCal one. Besides, the firmware has been revised to cope with the data flow related to the new detector mapping.
- Update of trigger algorithm in heavy ion collisions
  The background subtraction algorithm has been upgraded as described in Sec. 3.2. The results of its performances will be presented in the following section.

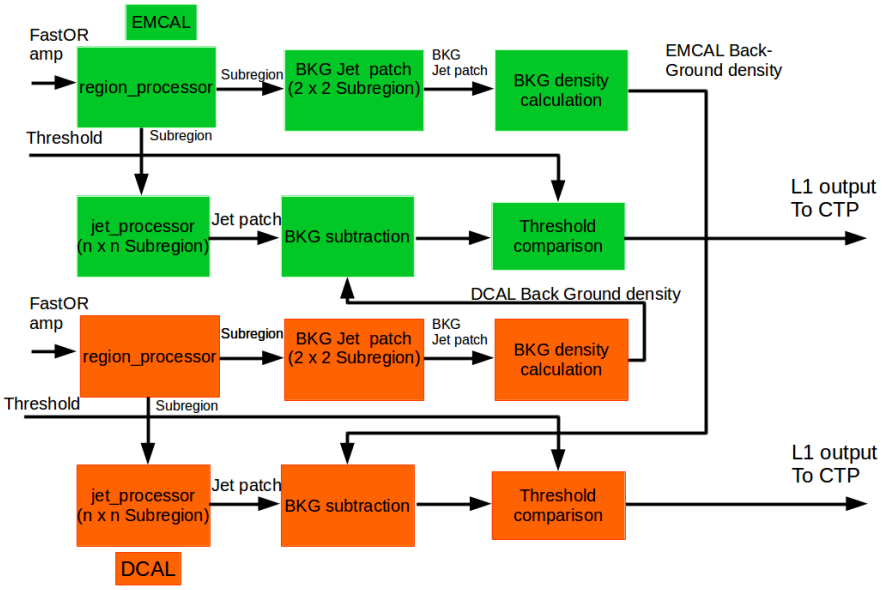

Figure 50: Flowchart of the STU L1-Jet trigger processing in heavy-ion collisions

– Update of the Common Data Header (CDH) version of the readout data stream
All data from each detector includes a Common Data Header (CDH) at the beginning of data payload. The CDH version has been updated to the new convention adopted for LHC Run 2 by ALICE (Fig. 52).

– Upgrade of the error monitoring counter for TRU-STU communication
The old firmware for LHC Run 1 had a 16 bit error counter to detect communication errors between TRU-STU and STU-STU (Fig. 53). The old error counter overflows every $25(\text{ns}) \times 65535 \sim 1.6$ (ms). For the LHC Run 2, the number of bit length assigned to the error counter has been extended to 32 bits and a 32 bits trial counter, which counts the number of test packets (inter packets), has been implemented (Fig. 54). The new error counter overflows every $25(\text{ns}) \times 4294967295 \sim 107$ (s). A precise data communication error rate estimation has been enabled by this upgrade.

The firmware has been written in Hardware Description Language (VHDL) and has been developed from the LHC Run1 version. The firmware is implemented as a digital circuit in the Virtex®-5 FPGA device (the product of Xilinx, inc.), which equips the STU board. The ISE® Design Suite, which is the IDE (Integrated Development

Environment) for the products of Xilinx inc., has been utilized for the development and compilation of the firmware, and for the simulation of the logic.

b.) Tests in laboratory

The firmware has been installed on a testbench at CERN. In order to validate the trigger algorithm and output data.

c.) Commissioning tasks at LHC Point 2

The firmware has been developed in the actual environment at LHC Point 2. Commissioning tasks have been performed before the 2015 Pb-Pb run. The STU routine operation through on-line Detector Control System (DCS) has been developed during this commissioning.

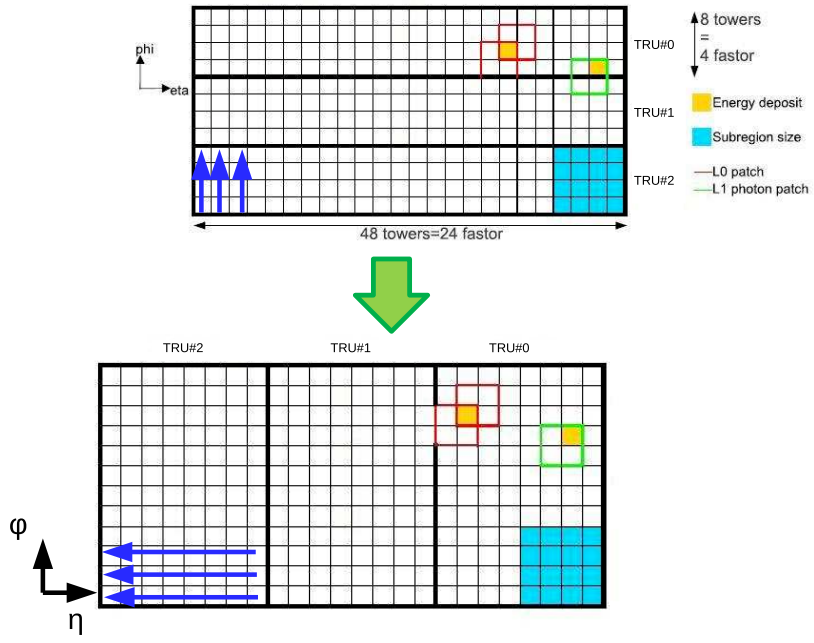

Figure 51: Modification of readout region by one TRU. This picture shows an example for one SM of EMCal.

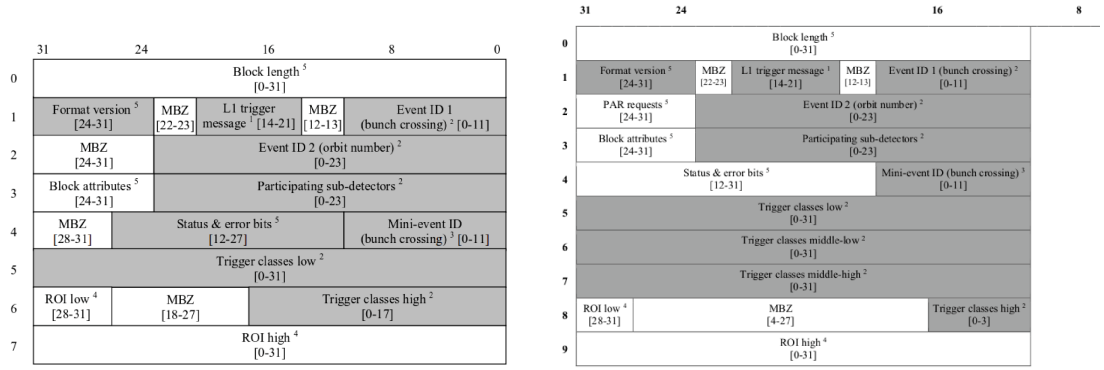

Figure 52: The old (left, [52]) and new (right, [53]) CDH.

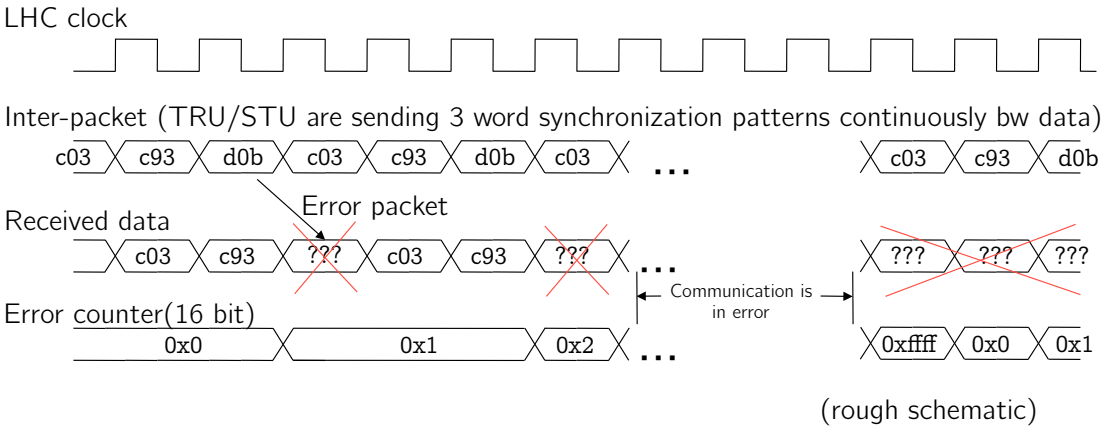

Figure 53: An example of the old error counter operation.

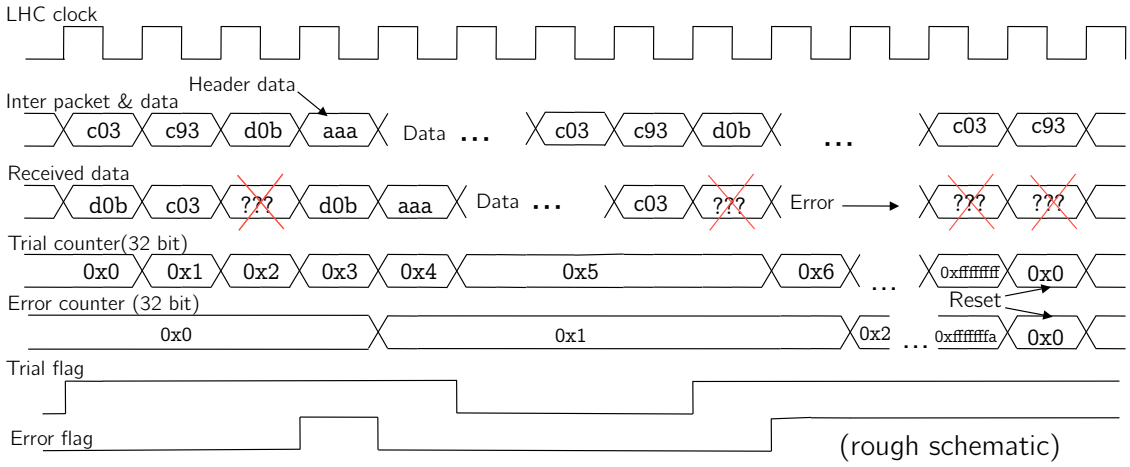

Figure 54: An example of the new error counter operation.

3.4 Trigger performance

In this section, trigger system performance evaluated with the data recorded during LHC Run2 are shown. Fig. 55 shows the correlation of the underlying event energy density. In this figure, clear positive correlation has been observed and the values are reasonably consistent. This result supports that the underlying event energy density have been calculated reasonably and the data exchange between EMCal ans DCal STUs have been performed correctly. Fig. 56 shows the rejection factor of L1-jet trigger, which represents the capability to control event rates, For example, a 20 GeV threshold results in a ∼100-1000 of event rejection (event rate is decreased by a factor ∼ 1/100 - 1/1000). Fig. 57 shows the rejection factor of L1-jet trigger as a function of estimated underlying event density and threshold. In this figure, it is found that the L1-jet trigger gives stable rejection factor over widen underlying event energy density range, which correlates to centrality. This results implies that, in case event-by-event underlying event subtraction is enabled, the kinematic cutoff for jets by the L1 trigger will be more stable for wide centrality range than the case without event-by-event underlying event subtraction. Fig. 58 shows the L1-jet trigger turn-on curve, which represents how rapidly full selection efficiency is reached, in Pb-Pb collisions at $sqrts_{\mathrm{NN}} = 5.02$ TeV as a function of the energy of a online jet trigger patch, where 'online' means the energy was estimated based on the raw amplitudes from each cell without offline calibration. The turn-on curve is calculated as a ratio of the trigger patch energy in the event triggered by both L1-jet and MB over the one in the MB triggered event. The turn-on curve shows a sharp rising and reaches plateau reasonably. Fig. 59 shows the enhancement

of EMCal L1-jet trigger for R = 0.2, 0.3, 0.4, and 0.5 full jets in pp collisions at $\sqrt{s}$ = 13 TeV and Fig. 60 shows the one of EMCal L1-gamma trigger for the EMCal clusters, which corresponds to energy deposit of a particle, in pPb collisions at $\sqrt{s_{\rm NN}}$ = 8.16 TeV. The EMCal L1-jet trigger enhances the full jet yields per trigger by a factor 2000-8000 and the EMCal L1-gamma enhances the high-energy cluster yields by a factor 200-800 for these dataset, in comparison with the yields in minimum-bias triggered events. Fig. 61 shows the $p_{\rm T}$ spectra of reconstructed PHOS clusters in central (0-5 %, left) and peripheral (60-80 %, right) Pb-Pb collisions at $\sqrt{s}$ = 5.02 TeV with minimum-bias and L1-gamma trigger. Both results show the sharp rising around the threshold. However, the heights of plateaus, which gives the photon enhancement factor provided by the trigger system, are different between these two centrality intervals. The enhancement factor is $\sim$ 100 for central events and $\sim$2000-3000 for peripheral events. This should come from the fact that the background subtraction is not performed for PHOS L1-gamma trigger, resulting in larger patch energies in central collisions.

As shown in Fig. 55-Fig. 61, the L1 trigger system shows reasonable behavior and it gives good performance on the physics analysis. The new physics results utilizing the trigger data, which have been collected in 2015-2018, start to come out now (e.g. Ref. [54, 55]).

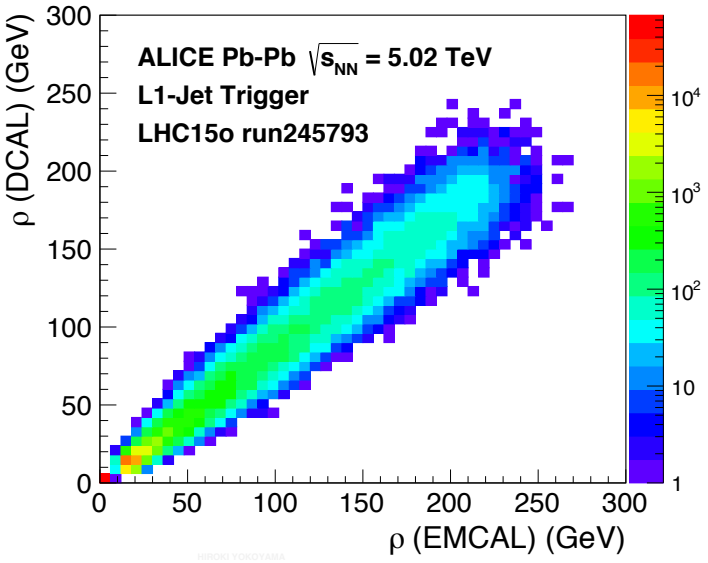

Figure 55: Correlation of underlying event energy density estimated by EMCal and DCal STUs [5].

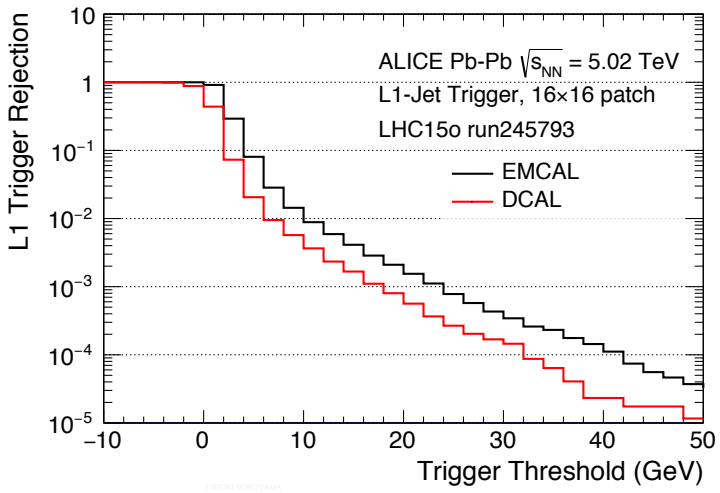

Figure 56: Rejection factor of L1-jet triggers given by DCal and EMCAL [5]

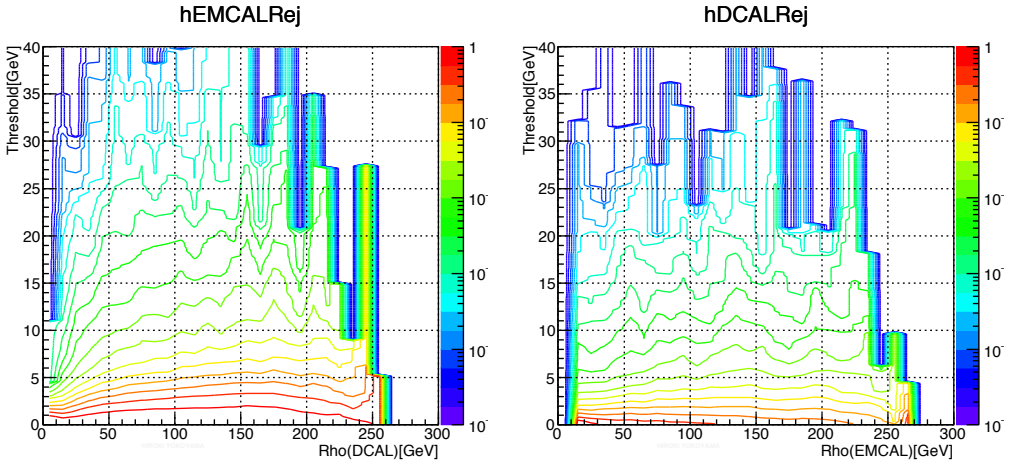

Figure 57: Rejection factor of L1-jet triggers given by EMCal (left) and DCal (right) as a function of underlying event energy density and threshold. x-axis is estimated underlying event energy density and y-axis is threshold. z-axis is rejection factor and its difference is expressed as colors.

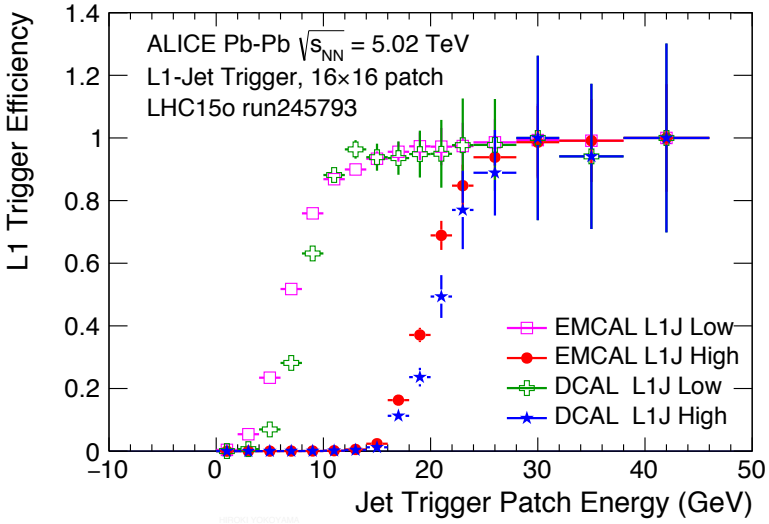

Figure 58: L1-jet trigger turn-on curves given by DCal and EMCAL [5]

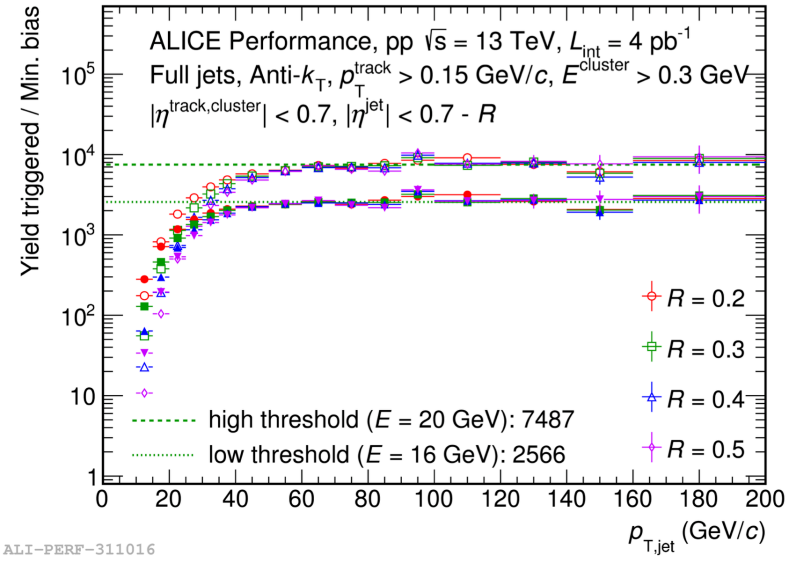

Figure 59: Enhancement of the EMCAL L1-jet trigger for full jets with various jet radii [56].

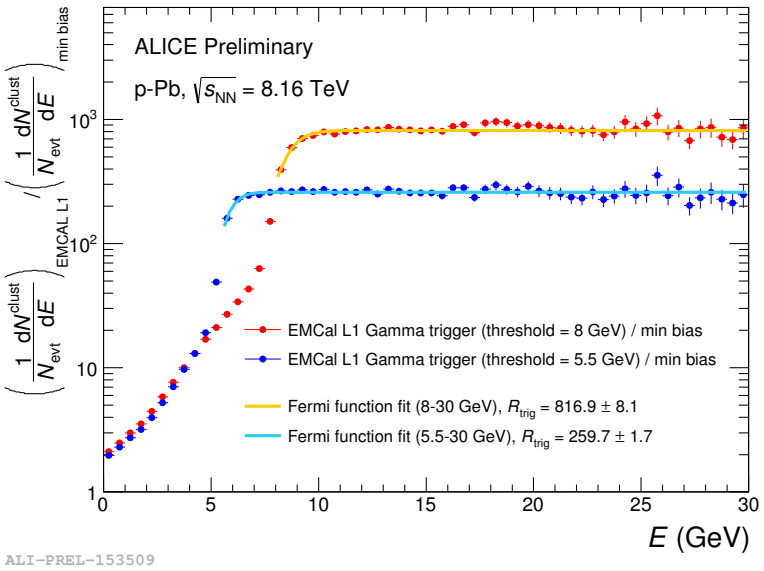

Figure 60: Enhancement of the EMCAL L1-gamma trigger as a function of reconstructed EMCal cluster energy [56].

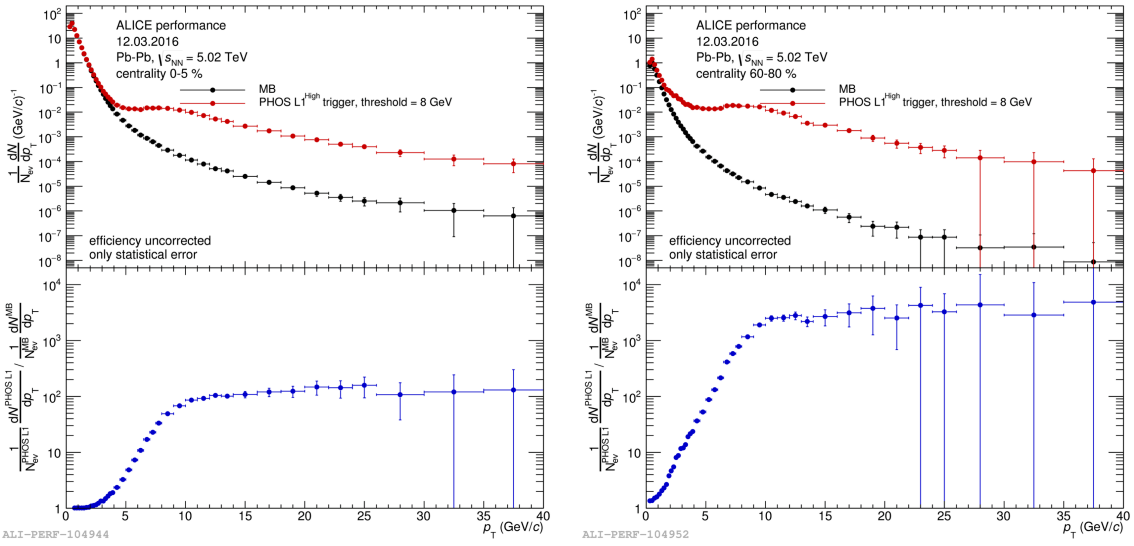

Figure 61: p_{T} spectra of reconstructed PHOS cluster in minimum-bias (black) and L1-gamma triggered event (red) are shown in the top panel. The ratio of these spectra is shown in the bottom panel [56].
Left: Central (0-5 %) Pb-Pb collisions
Right: peripheral (60-80 %) Pb-Pb collisions.

Chapter 4 Datasets and analysis methods

4.1 Data samples

For the studies presented in this thesis, the datasets of pp collisions at $\sqrt{s} = 5.02$ TeV and Pb-Pb collisions at $\sqrt{s_{\rm NN}} = 5.02$ TeV collected by the ALICE in 2015 were analyzed. Monte-Carlo (MC) full detector simulation data anchored to selected LHC periods were also analyzed to assess the corresponding detector response. pp and Pb-Pb events were generated by PYTHIA6,8 [57],[58] and HIJING [59] MC event generators respectively. The detector effects were described with GEANT3-based detailed simulations [60].

4.2 Event selections

The analyzed events were collected with a Minimum-Bias (MB) trigger. During 2015 data taking, the MB trigger was defined by the coincidence between V0A and V0C detectors. After MB trigger selection, several primary vertex quality cuts were applied:

- A primary vertex is reconstructed with at least 1 (pp) or 2 (Pb-Pb) contributors from SPD tracklets.
- $|z_{\rm vertex}^{track}| < 10({\rm pp}), 8({\rm Pb\text{-}Pb})\,{\rm cm}$.
- $|z_{\rm vertex}^{\rm track} - z_{\rm vertex}^{\rm SPD}| < 0.5({\rm pp}), 0.2({\rm Pb\text{-}Pb})\,{\rm cm}$ (see Sec. 2.2.2, 2.2.3).
  Here, the resolution on $z_{\rm vtx}^{\rm SPD}$ have to be better than 0.25 cm.

In order to remove pile-up events, multi-vertex events reconstructed by SPD were rejected in pp collisions. For the Pb-Pb collisions, optional cuts mainly related to pile-up rejection were additionally applied as follows:

- Event selection with centrality correlation
  - $\pm^{5.5}_{5}\,\sigma$ cut of V0 centrality using the correlation between V0 and SPD estimated centralities.
- Event selection related to track multiplicity, e.g.
  - $\pm 4\sigma$ cut on the multiplicity correlation of tracks reconstructed from the primary vertex + ITS + TPC + TOF hits and primary vertex + ITS + TPC tracks.

– event rejection with large number of TPC clusters

After events selection, about 10^8 pp and about 5.5×10^7 Pb-Pb (0-80% centrality) events remained. In this study, 30-50% centrality events in Pb-Pb collisions were analyzed corresponding to about 1.4×10^7 events. The centrality was determined with the V0 detector as shown in Fig. 11.

4.3 Charged particle tracking and selection

For this study, primary tracks are reconstructed with ITS+TPC detectors so-called 'global tracks'. A Kalman filter tracking method has been developed to perform the global tracking at ALICE [61]. The ALICE standard global track selection requires at least one hit in one of the two SPD layers. However, due to large dead areas in SPD, the azimuthal distribution of reconstructed tracks is not uniform. The tracking uniformity is one of the key factors to reconstruct jets with high spatial and momentum resolution. Therefore, a dedicated track selection, called 'hybrid track' selection, has been developed for jet measurements. Hybrid tracks are made up of two track classes:

- Global tracks: fully reconstructed ITS+TPC tracks with at least one SPD hit and inward track refit [61] through the ITS.
- Complementary tracks: ITS+TPC tracks with no SPD hit. Instead, the reconstructed tracks are constrained to the primary vertex and the track parameters are recalculated to improve the track spatial and momentum resolutions. The inward track refit through the ITS is still required.

The azimuthal distributions of global and complementary tracks are shown in Fig. 62. The hybrid track selection recovers track uniformity reasonably well.

The acceptance of tracks is $0 < \phi_{\rm track} < 2\pi$, $|\eta_{\rm track}| < 0.9$. A kinematic cut of $0.15 < p_{\rm T,track} < 100$ GeV/c is applied to ensure good track $p_{\rm T}$ resolution.

4.4 Jet reconstruction

Signal jets were reconstructed with the anti-$k_{\rm T}$ clustering algorithm [62] implemented in the FastJet software package [63]. Jets are reconstructed with jet resolution parameters $R = 0.2, 0.3, 0.4$, and 0.6 for pp collisions and $R = 0.2$ for Pb-Pb collisions. To evaluate event-by-event background $p_{\rm T}$ density for jets in Pb-Pb collisions, jet reconstruction with the $k_{\rm T}$ clustering algorithm is also performed with the resolution parameter of $R = 0.4$. The inputs to jet finding algorithms are all tracks passing the hybrid track selection. The pseudo-rapidity of reconstructed jet is restricted by a fiducial cut to $|\eta_{\rm jet}| < 0.9 - R$. Consequently,

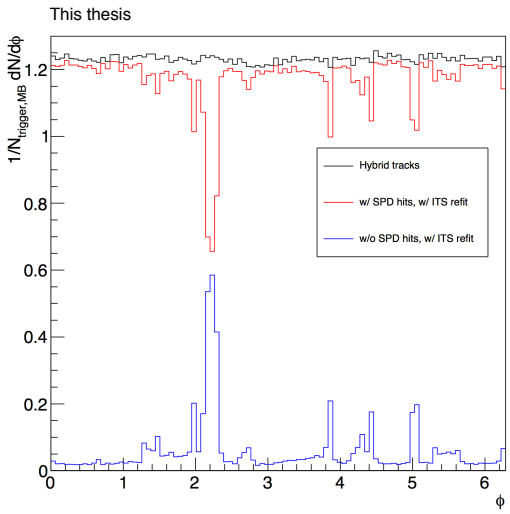

Figure 62: The azimuthal distribution of global tracks (Red: w/ SPD hits), complementary tracks (Blue: w/o SPD hits) and hybrid tracks (Black) in pp collisions at $\sqrt{s} = 5.02$ TeV

jets are contained within the fully efficient acceptance of the TPC, thus avoiding unexpected edge effects. Jet reconstruction ingredients are summarized in Table 3.

Table 3: Reconstruction conditions of jets

FastJet version	v3.1.3
Reconstruction algorithm	anti-k_{T} (Signal), k_{T} (Background for Pb-Pb)
Inputs	charged tracks (w/ hybrid track selection)
Cone radii R	0.2, 0.4 (for pp and for Background of Pb-Pb) 0.3, 0.6 (for pp)
Pseudo-rapidity	$\lvert\eta_{jet}\rvert < 0.9-R$
p_T recombination scheme	p_{T}-scheme
Ghost area units for jet are determination	0.005
Jet area cut	$\mathrm{Area}_{jet} > 0.6\pi R^2$ (for Pb-Pb)

4.5 Measurement of charged jets in pp collisions

4.5.1 Underlying event estimation in pp collisions

Jets come from hard processes but reconstructed jets include contributions from soft processes even in pp collisions. These soft contributions are classified as Underlying Event (UE). Experimentally, it is difficult to distinguish if low-p_{T} jets come from hard or soft

processes. The same underlying event definition both for experimental data analysis and theoretical calculations must be used to make a fair comparison. In this analysis, the perpendicular cone method is chosen as the UE estimator [30]. The sum of track p_{T} in a cone perpendicular to the leading jet axis is divided by jet area to obtain the jet background p_{T} density ρ on an event-by-event basis:

$$\rho = \sum_{i=0}^{n} p_{\mathrm{T}i,\mathrm{track}}^{\text{perp. cone}} / \pi R^2 \tag{32}$$

where R are the jet cone radius of signal jets and $p_{\mathrm{T}i,\mathrm{track}}^{\text{perp. cone}}$ is the transverse momenta of tracks within a cone perpendicular to the leading jet axis. The background p_{T} is subtracted jet-by-jet as follows

$$p_{\mathrm{T},jet}^{raw} - \rho \cdot A_{\mathrm{jet}} \tag{33}$$

where A_{jet} is the jet area. In this thesis, results obtained both with and without UE subtraction are shown.

4.5.2 Raw jet spectra

Fig. 63 and Fig. 64 shows the inclusive raw jet spectra without and with UE subtraction respectively. These raw spectra are distorted (folded) by detector effects such as inefficiency and finite resolution. They must be unfolded from these effects to make comparison with the theoretical predictions. With the data sample used in the present analysis, a statistical reach up to $p_{\mathrm{T,jet}}^{\mathrm{ch}} = 100\,\mathrm{GeV}/c$ is achieved. Jets are measured to very low transverse momenta similarly to the study presented in Ref. [64]. The p_{T} binning is chosen so that the number of entries exceeds ten entries per bin for all cone radii in order to ensure stable unfolding results.

4.5.3 Detector effect correction by unfolding

In order to correct the measured jet p_{T} spectra from detector effects, an unfolding method based on the Singular Value Decomposition (SVD) approach [65] is employed within the 'RooUnfold' software package [66],[67]. The basic concept of raw jet spectra spectra unfolding is explained hereafter:

The relation between the true spectrum $\mathbf{T}_t$ and the measured spectrum $\mathbf{M}_m$ can be expressed as:

$$\mathbf{M}_m = \mathbf{R}_{m,t}^{\mathrm{det}} \cdot \mathbf{T}_t \tag{34}$$

where the detector 'response matrix' (RM), $\mathbf{R}_{m,t}^{\mathrm{det}}$, represents the distortion of the observable by a detector response. The subscripts m, t are the bin number indices. If $\mathbf{R}_{m,t}^{\mathrm{det}}$ is known, the true spectrum can be estimated as the product of the inverse matrix of $\mathbf{R}_{m,t}^{\mathrm{det}}$ and

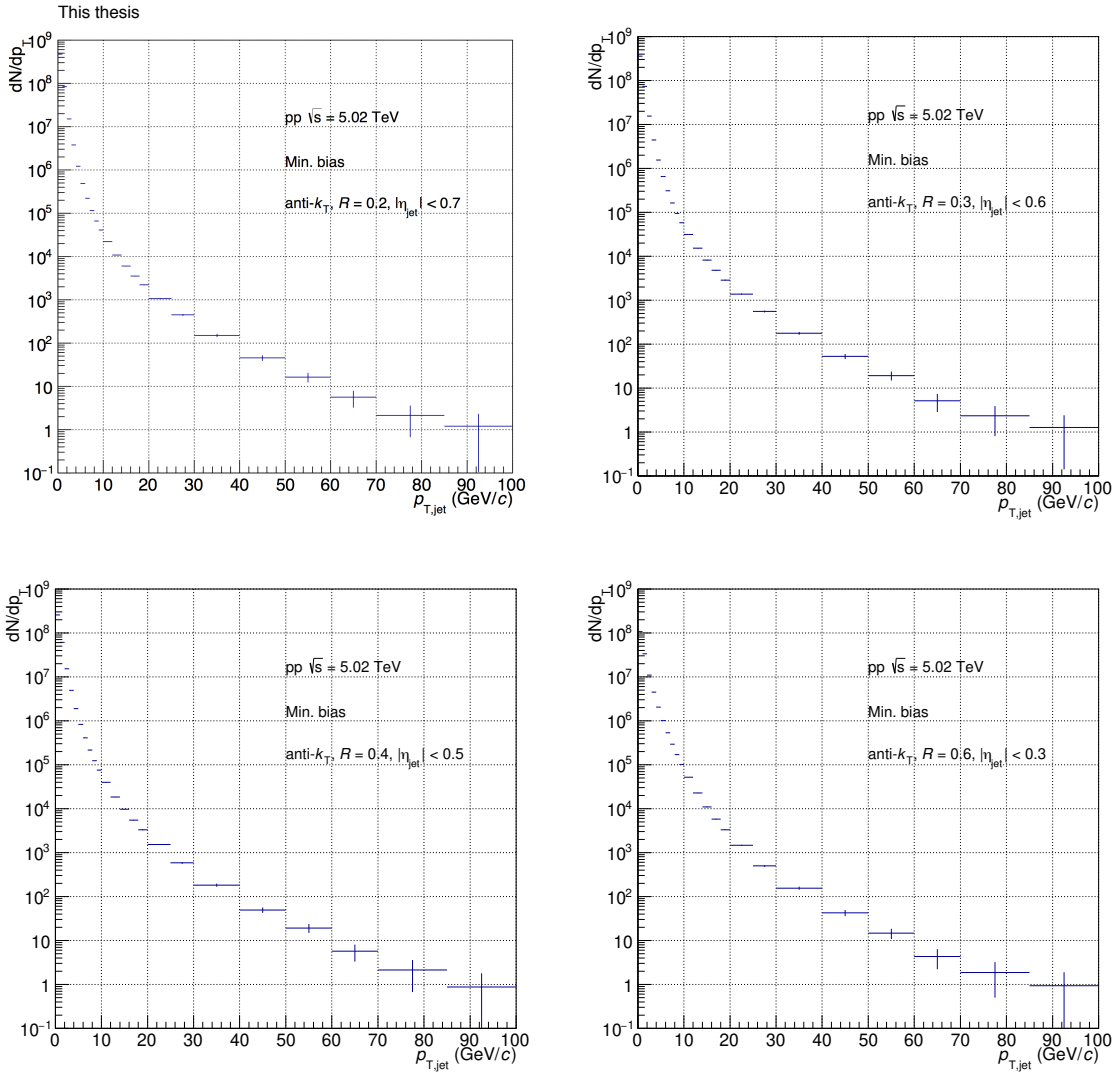

Figure 63: Charged jet raw p_{T} spectra reconstructed with R =0.2,0.3,0.4, and 0.6 in pp collisions at $\sqrt{s} = 5.02$ TeV without UE subtraction

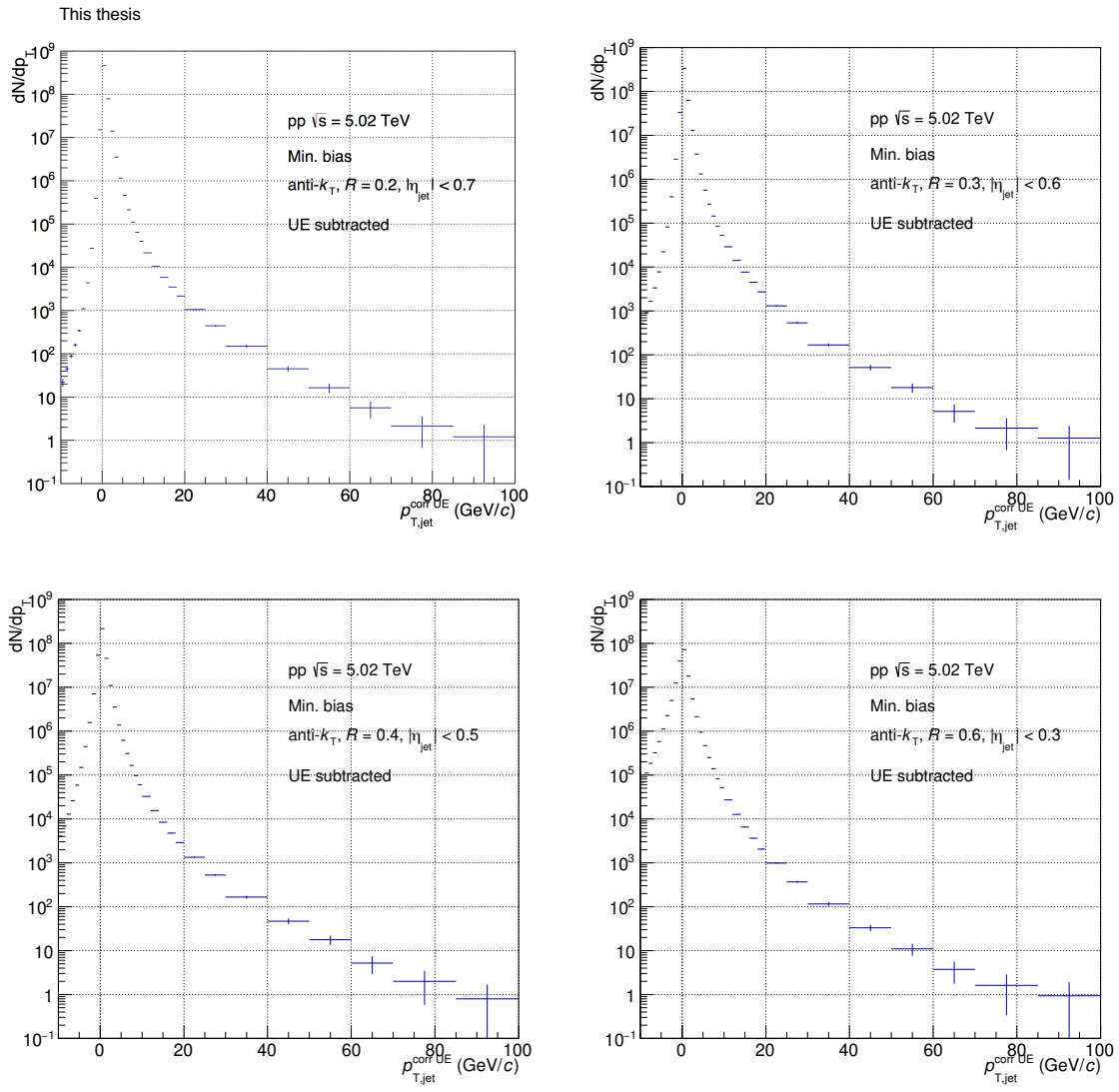

Figure 64: Charged jet raw p_{T} spectra reconstructed with R =0.2,0.3,0.4, and 0.6 in pp collisions at $\sqrt{s} = 5.02$ TeV with UE subtraction

$\mathbf{M}_m$. In this study, the detector responses were evaluated by GEANT3-based full detector simulations.

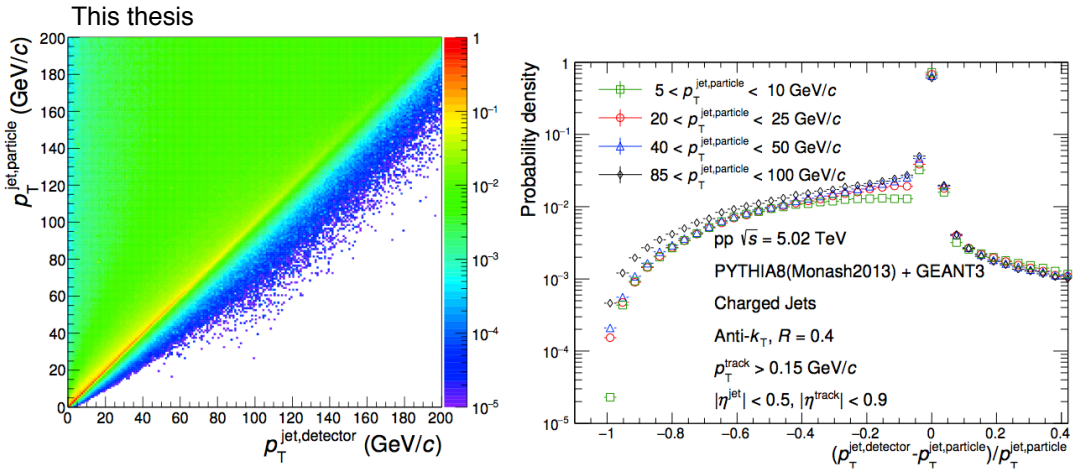

Figure 65: Left: Detector response matrix for $R = 0.4$ anti-k_{T} clusters reconstructed with charged tracks. Right: Probability distribution of the relative momentum difference of simulated ALICE detector response to charged jets in pp collisions at $\sqrt{s} = 5.02$ TeV for four different p_{T} intervals. Charged jets are simulated using PYTHIA8 Monash-2013 and reconstructed with the anti-k_{T} jet finding algorithm with $R = 0.4$.

4.5.4 Validation of the unfolding

The following tests were performed to check the validity of the unfolding solution:

- Split the available MC statistics into two exclusive sub-samples.
  One group is used to construct the response matrix and the other group is used to extract the jet spectrum folded by the detector effects. Fig. 66 shows the ratio of the unfolded spectrum over the true spectrum (left) and the ratio of the re-folded spectrum over the detector level spectrum (right). Both ratios are consistent with unity within a few percent.

- Comparison of different event generators
  The dependence of the unfolded spectrum on event generators is tested. The detector response is evaluated with PYTHIA8+GEANT3 MC dataset while the detector level jet spectrum is extracted from PYTHIA6+GEANT3. Fig. 67 shows the ratio of the unfolded spectrum over the true spectrum (left) and the ratio of the re-folded spectrum

over the detector level spectrum (right). The ratios are consistent with unity within a few percent except in the low p_{T} range ($p_{\mathrm{T}} < 20\mathrm{GeV}/c$). For the PYTHIA8+GEANT3 production, a lower limit on the hard scattering kinematic range is required to enhance the statistics of high-p_{T} jets ($p_{T,hard} > 5\mathrm{GeV}/c$). This results in the bias observed in Fig. 67 (left) at low-p_{T}.

The results of these two tests validated the unfolding procedure. In this study, the detector response extracted from a MB MC production is used to correct the jet spectra at low p_{T} ($p_{\mathrm{T}} < 20$ GeV/c) to avoid the above mentioned bias due to event generation. A high-p_{T} jet enhanced MC production is used to correct jet spectra in p_{T} region with good statistical precision ($p_{\mathrm{T}} > 20$ GeV/c).

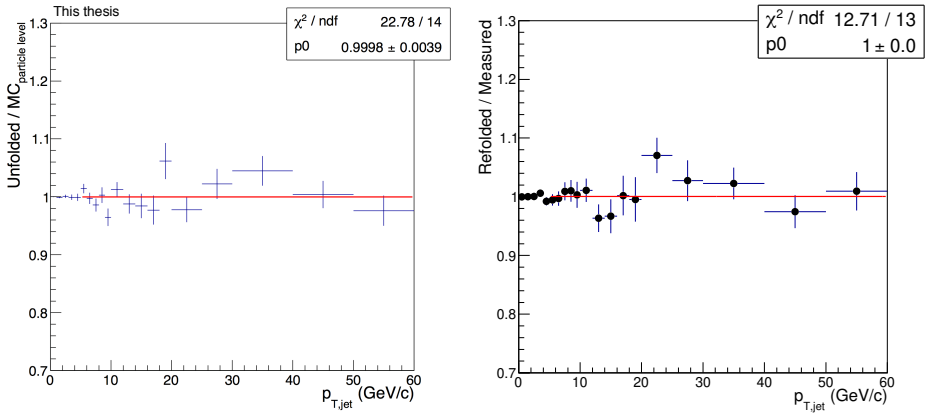

Figure 66: MC closure test results: the statistics in the PYTHIA8+GEANT3 production is divided into two sub-samples. One is used to build the response matrix and the other one is used to obtain the input spectrum.

4.5.5 Inclusive jet cross section

The inelastic double-differential jet cross section is defined as:

$$\frac{\mathrm{d}^2\sigma_{\mathrm{jet}}}{\mathrm{d}p_T\mathrm{d}\eta} = \frac{1}{\mathscr{L}_{\mathrm{int}}} \cdot \frac{N_{jet}}{\Delta p_T \Delta\eta} \tag{35}$$

where N_{jet} is the number of jets in each p_{T} bin of width Δp_{T} and $\Delta\eta$ is the pseudorapidity interval. The integrated luminosity $\mathscr{L}_{\mathrm{int}} = N^{evt}_{trig}\varepsilon_{\mathrm{vtx}}/\sigma_{\mathrm{V0}}$. Here, N^{evt}_{trig} is the number of triggered event after vertex selection (see Sec. 4.2). σ_{V0} is the measured visible inelastic cross section, which is the product of the true inelastic cross section and the MB trigger efficiency by the V0 detector, evaluated by Van der Meer (VdM) scan. The measured visible inelastic pp cross section at $\sqrt{s} = 5.02$ TeV is $\sigma_{\mathrm{V0}} = 51.2$ mb [68]. The number of

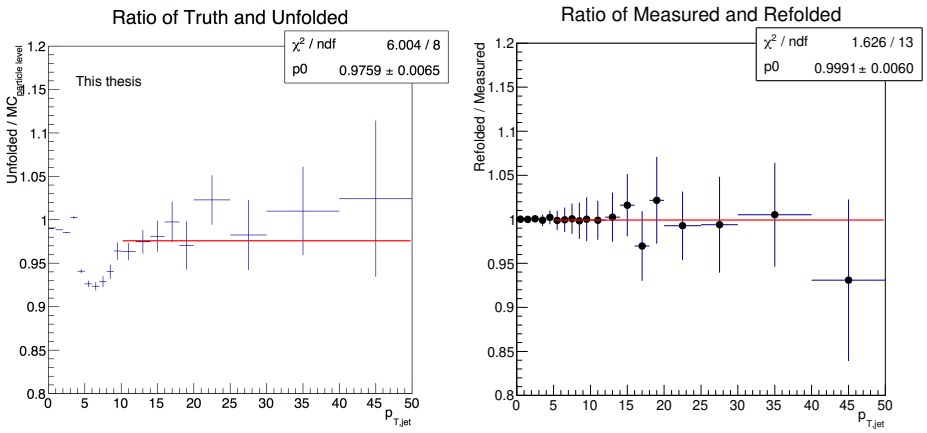

Figure 67: MC closure test results: we performed the closure test with different generators. In this figure, PYTHIA8+GEANT3 MC production is used to extract the response matrix and PYTHIA6+GEANT3 MC production is used to extract input spectrum.

triggered event in Eq. 35 has to be corrected for the vertex selection efficiency $\varepsilon_{\rm vtx}$ which imposes that all events including a jet in the acceptance must have a reconstructed vertex. The efficiency is evaluated before the vertex position cut ($|z_{vertex}| < 10$ cm) is applied, assuming a negligible vertex position dependence. In this study, $\varepsilon_{\rm vtx} \sim 1.024$ is used for the correction.

4.6 Measurement of charged jets in Pb-Pb collisions

4.6.1 Measurement of the event plane

Experimentally, the n^{th}-order event plane angle ψ_n^{meas} is determined event-by-event from the measured particle azimuthal distribution as follows:

$$Q_{n,x} = \sum_i w_i \cos\left(n\phi_i\right) \tag{36}$$

$$Q_{n,y} = \sum_i w_i \sin\left(n\phi_i\right) \tag{37}$$

$$\psi_n^{meas} = \frac{1}{n}\tan^{-1}\left(\frac{Q_{n,y}}{Q_{n,x}}\right) \tag{38}$$

where $Q_{n,x}, Q_{n,y}$ are the event flow vectors, w_i is a weight, and ϕ_i is the azimuthal angle of measured particle i. In the V0-based EP determination used in this analysis, V0C detector segments are used instead of measured particles. The weight w_i and azimuthal angle ϕ_i in Eq. 36, 37, 38 refer to the charge output of the V0 PMT and azimuthal angle of segment i respectively.

Since the relative positions of the two colliding nuclei are random, the azimuthal distribution of the event plane should be flat. However, in reality, the azimuthal distribution of the measured event planes is usually not constant related to some unphysical effects due to experimental apparatus, such as non-uniform PMT gains, offset of the beam position, and non-uniform acceptance. Calibrations were applied on the measured event plane to correct for such unphysical effects. The PMT gains were calibrated so that all PMTs have the same ADC mean value. $Q_{n,x}, Q_{n,y}$ distributions were re-centered and ψ_n^{meas} distribution is flattened [69]. Fig. 68 shows the correlation of event plane measured by V0A and V0C detectors before and after the correction. The distortion of the correlation observed before correction is fixed by the correction process.

The analytical expression of the event plane resolution is formulated in Ref. [69], [70] as:

$$\left\langle \cos\left[kn\left(\psi_n^{meas} - \psi_n^{true}\right)\right]\right\rangle = \frac{\sqrt{\pi}}{2\sqrt{2}}\chi_n e^{-\chi_n^2/4}\left[I_{(k-1)/2}\left(\frac{\chi_n^2}{4}\right) + I_{(k+1)/2}\left(\frac{\chi_n^2}{4}\right)\right] \tag{39}$$

where I_k is the modified Bessel function. The parameter χ_n is expressed as $\chi_n = v_n\sqrt{2N}$ where N is the number of particles used to measure the event plane.

The analytical expression of the distribution of the measured event plane angle w.r.t the true event plane is given in Ref. [71] as:

$$\frac{dN}{d\left[kn\left(\psi_n^{meas} - \psi_n^{true}\right)\right]} = \frac{1}{\pi}e^{-\chi_n^2/2}\left[1 + z\sqrt{\pi}[1 + \mathrm{erf}(z)]e^{z^2}\right] \tag{40}$$

where $z = \chi_n \cos kn\left(\psi_n^{meas} - \psi_n^{true}\right)$ and $\mathrm{erf}(z)$ is the error function.

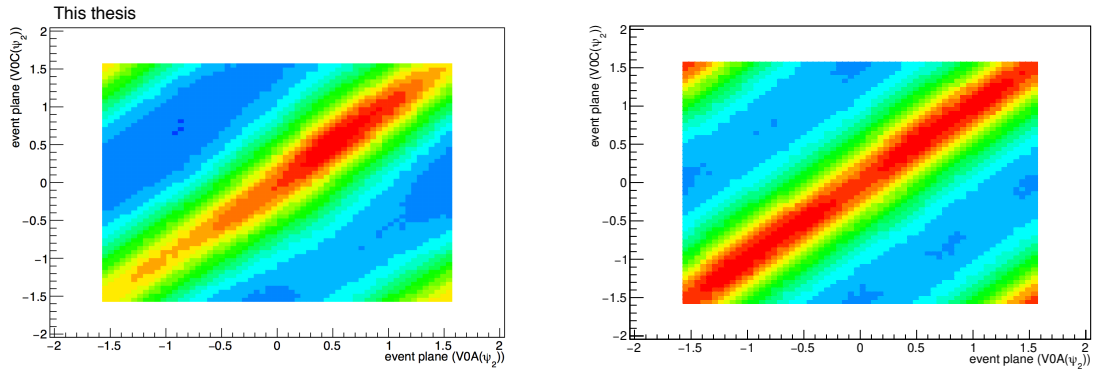

Figure 68: V0A and V0C event plane correlation before (Left) and after (Right) correction in Pb-Pb collisions at $\sqrt{s_{\rm NN}} = 5.02$ TeV

Experimentally, the correlation of event plane measured with detector A and B is calculated as:

$$\begin{aligned}\left\langle \cos\left(n\left[\psi_{n,A}^{meas} - \psi_{n,B}^{meas}\right]\right)\right\rangle &= \left\langle \cos\left(n\left[\psi_{n,A}^{meas} - \psi_{n}^{true}\right] - n\left[\psi_{n,B}^{meas} - \psi_{n}^{true}\right]\right)\right\rangle \\ &= \left\langle \cos\left(n\left[\psi_{n,A}^{meas} - \psi_{n}^{true}\right]\right)\right\rangle \left\langle \cos\left(n\left[\psi_{n,B}^{meas} - \psi_{n}^{true}\right]\right)\right\rangle \\ &= \mathrm{Res}\left\{\psi_{n,A}^{meas}\right\} \cdot \mathrm{Res}\left\{\psi_{n,B}^{meas}\right\}\end{aligned} \tag{41}$$

where $\mathrm{Res}\left\{\psi_{n,A,B}^{meas}\right\}$ is the resolution of the n^{th}-order event plane measured with the detector A,B. In symmetric collision systems, $\mathrm{Res}\left\{\psi_{n,A}\right\}$ will equal $\mathrm{Res}\left\{\psi_{n,B}\right\}$ if detector A and B cover a symmetric acceptance and have similar average multiplicity. Thus, the event plane resolution is given by:

$$\mathrm{Res}\left\{\psi_{n,A}^{meas}\right\} = \mathrm{Res}\left\{\psi_{n,B}^{meas}\right\} = \sqrt{\left\langle \cos\left(n\left[\psi_{n,A}^{meas} - \psi_{n,B}^{meas}\right]\right)\right\rangle}\,. \tag{42}$$

In ALICE, most of the forward/backward detectors have asymmetric acceptance on rapidity. In this case, the event plane resolution can be evaluated with 3 detectors which have exclusive rapidity coverages. This method is called '3-sub method'. The correlations of event plane among detectors A, B and C are expressed as:

$$\left\langle \cos\left(n\left[\psi_{n,A} - \psi_{n,B}\right]\right)\right\rangle = \mathrm{Res}\left\{\psi_{n,A}\right\} \cdot \mathrm{Res}\left\{\psi_{n,B}\right\} \tag{43}$$

$$\left\langle \cos\left(n\left[\psi_{n,B} - \psi_{n,C}\right]\right)\right\rangle = \mathrm{Res}\left\{\psi_{n,B}\right\} \cdot \mathrm{Res}\left\{\psi_{n,C}\right\} \tag{44}$$

$$\left\langle \cos\left(n\left[\psi_{n,C} - \psi_{n,A}\right]\right)\right\rangle = \mathrm{Res}\left\{\psi_{n,C}\right\} \cdot \mathrm{Res}\left\{\psi_{n,A}\right\}\ . \tag{45}$$

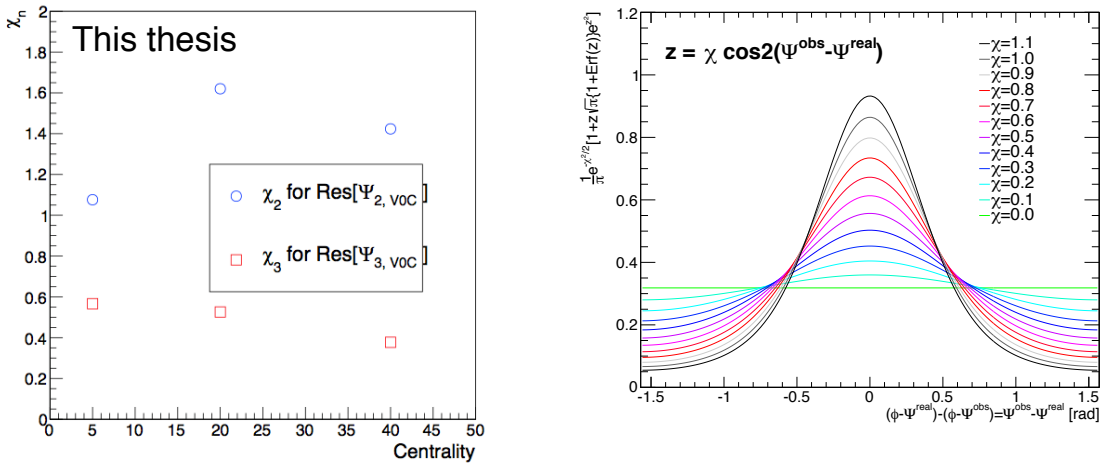

Figure 69: Left: Parameter χ_n in the mathematical expression of event plane resolution for V0C. Right: Probability distribution of $\psi_2^{\text{meas}} - \psi_2^{\text{true}}$. The figure is taken from Ref. [70]

Combining Eq. 43, 44, 45, the EP resolution measured with the detector A is given by:

$$\text{Res}\left\{\psi_{n,A}\right\} = \sqrt{\frac{\left\langle \cos\left(n\left[\psi_{n,A} - \psi_{n,B}\right]\right)\right\rangle \left\langle \cos\left(n\left[\psi_{n,C} - \psi_{n,A}\right]\right)\right\rangle}{\left\langle \cos\left(n\left[\psi_{n,B} - \psi_{n,C}\right]\right)\right\rangle}} \tag{46}$$

In the measurement presented in this work, the event plane resolution of V0C is evaluated with the 3-sub method by utilizing the event plane correlations among V0A, V0C and TPC.

Fig. 69 (Left) shows the evaluated parameter χ_n of Eq. 39. Fig. 70 shows the estimated 2^{nd}-order event plane resolution for V0C. The 2^{nd} order event plane resolution measured by V0C is about 70% for mid-central Pb-Pb collisions (30-50%).

4.6.2 Underlying event estimation in Pb-Pb collisions

Controlling the systematic uncertainties of the large underlying event (UE) estimation is one of the key elements of jet measurements in heavy-ion collisions. In this measurement, the average UE p_{T} density ρ^{avg} is estimated on an event-by-event basis as follows:

$$\rho^{\text{avg}} = median\left\{\frac{p_T^{k_{\text{T},i}}}{A_{k_{\text{T},i}}}\right\} \tag{47}$$

where $p_{\text{T}}^{k_{\text{T},i}}$ is the transverse momentum and $A_{k_{\text{T},i}}$ is the area of the cluster i reconstructed with the k_{T}-clustering algorithm.

In non-central heavy-ion collisions, the average UE p_{T} density will show large modulations w.r.t event plane because of the anisotropic particle production ascribed to flow effects. Therefore, in this measurement, the local UE density w.r.t 2^{nd} and 3^{rd} order event

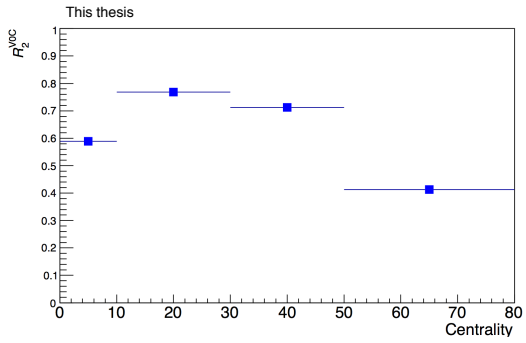

Figure 70: V0C 2nd order event plane resolution estimated with 3-sub detector method (V0C-V0A-TPC)

plane is calculated on an event-by-event basis by fitting the azimuthal distribution of low momentum tracks ($p_T < 5$ GeV/c). The local UE estimate $\rho(\phi)$ is obtained by fitting the first three terms of the Fourier decomposition:

$$\rho(\phi) = \rho_0 \left(1 + 2\left\{v_2^{obs}\cos(2[\phi - \psi_2]) + v_3^{obs}\cos(3[\phi - \psi_3])\right\}\right) \ . \tag{48}$$

Fig 71 shows an example of fitting result to the track distrabution in an event.

Using $\rho(\phi)$, the jet-by-jet local UE density ρ^{local} is calculated as follows:

$$\rho^{local} = \frac{\rho^{\mathrm{avg}}}{2R\rho_o}\int_{\phi-R}^{\phi+R}\rho(\phi)d\phi \tag{49}$$

The estimated local UE is subtracted jet-by-jet in a similar way as Eq. 33. This local UE estimation method is firstly proposed for the measurement of azimuthal anisotropy of charged jet production in $\sqrt{s_{\mathrm{NN}}} = 2.76$ TeV Pb-Pb collisions [36].

4.6.3 Charged jet yield with respect to event plane

Fig. 72 shows the measured raw jet p_{T} spectra w.r.t the 2^{nd}-order V0C event plane with average UE subtraction (left) and with local UE subtraction (right).

The low-p_{T} region dominated by UE becomes reasonably uniform w.r.t the ψ_2 plane after local UE subtraction. The detector level jet spectra are divided into two classes w.r.t ψ_2 as shown in Fig. 73.

The measured jet spectra are unfolded by the SVD approach in a similar way to the jet spectra in pp collisions (Sec. 4.5.3). In heavy-ion collisions, the large UE fluctuations are not negligible and have to be corrected for in the unfolding procedure. Thus, the relation between the true spectrum $\mathbf{T}_t$ and the measured spectrum $\mathbf{M}_m$ is expressed as:

$$\mathbf{M}_m = \mathbf{R}_{m,t}^{\mathrm{bkg+det}} \cdot \mathbf{T}_t = \mathbf{R}_{m,d}^{\mathrm{bkg}} \cdot \mathbf{R}_{d,t}^{\mathrm{det}} \cdot \mathbf{T}_t \tag{50}$$

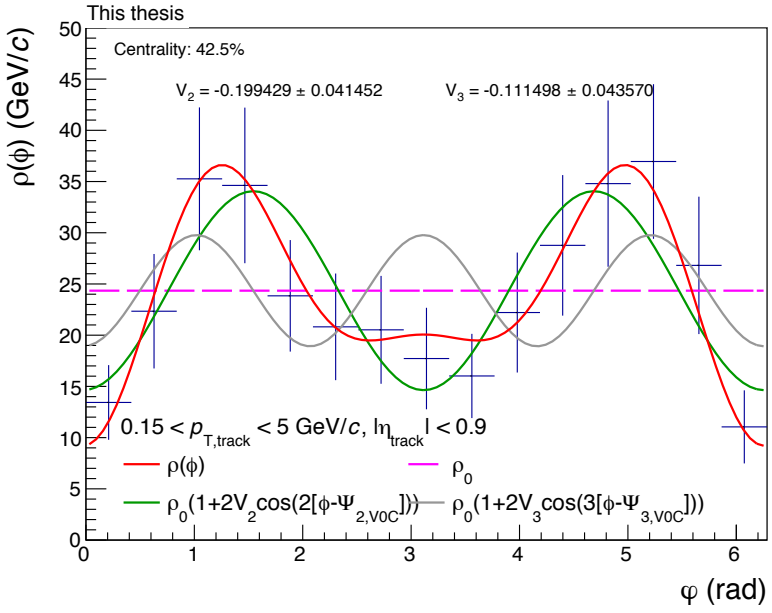

Figure 71: A event fitting result to the track distribution with Eq. 48 in mid-central Pb-Pb collisions at $\sqrt{s_{\rm NN}} = 5.02$ TeV.

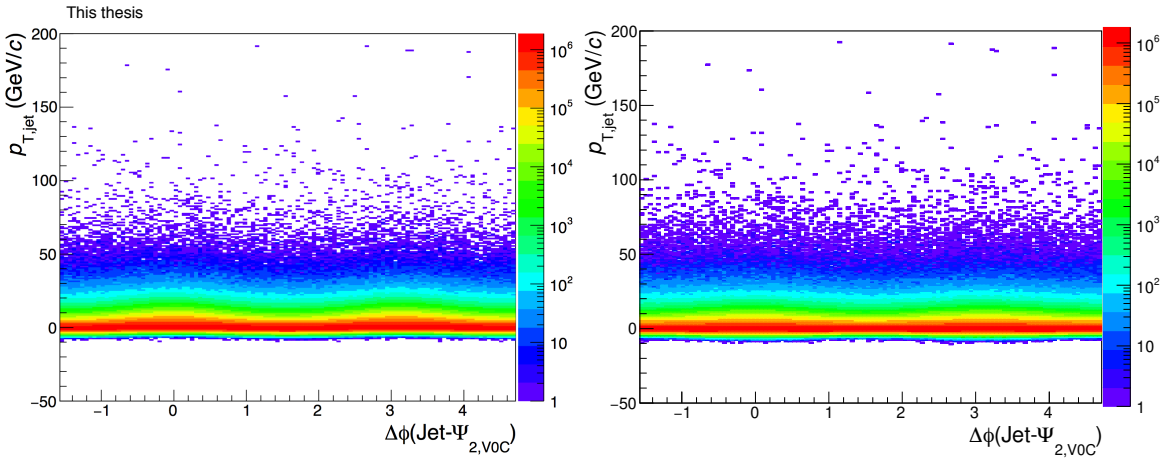

Figure 72: The raw jet $p_{\rm T}$ spectra w.r.t the 2^{nd} order V0C event plane in 30-50% centrality Pb-Pb collisions at $\sqrt{s_{\rm NN}} = 5.02$ TeV.
Left: average UE subtracted,
Right: local UE subtracted.

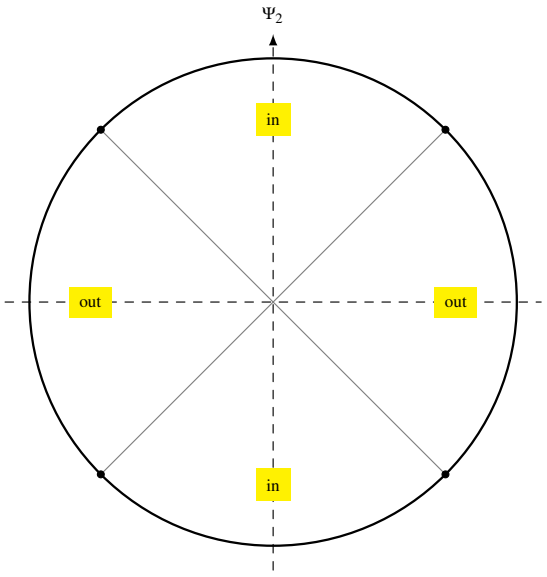

Figure 73: Definition of in-plane and out-of-plane directions in this jet v_2^{jet} measurement.

where $\mathbf{R}_{m,d}^{\text{bkg}}$ is the response matrix of the UE fluctuations.
In this study, the UE fluctuations were estimated by the Random Cone (RC) method [72] as:

$$\delta p_{\text{T}} = \sum_{i}^{RC} p_{\text{T},i}^{\text{track}} - \rho^{local} \pi R^2 \tag{51}$$

where $\sum_i^{RC} p_{\text{T},i}^{\text{track}}$ is the sum of track p_{T} within a RC and R is the jet resolution parameter. In this study, one RC per event is thrown into the data.

The jet yield w.r.t event plane is expressed as:

$$\frac{dN}{d\left(\varphi_{\text{jet}} - \psi_n\right)} \propto 1 + \sum_{n=1}^{\infty} 2 v_n^{\text{jet}} \cos\left[n\left(\varphi_{\text{jet}} - \psi_n\right)\right] \ . \tag{52}$$

Using the in-plane and out-of-plane directions defined in the Fig. 73, the jet yields in-plane and out-of-plane w.r.t event plane can be written as:

$$\begin{aligned} N_{in} &= \int_{\frac{-\pi}{4}}^{\frac{\pi}{4}} \frac{dN}{d\left(\varphi_{\text{jet}} - \psi_n^{meas}\right)} d\left(\varphi_{\text{jet}} - \psi_n^{meas}\right) + \int_{\frac{3\pi}{4}}^{\frac{5\pi}{4}} \frac{dN}{d\left(\varphi_{\text{jet}} - \psi_n^{meas}\right)} d\left(\varphi_{\text{jet}} - \psi_n^{meas}\right) \\ N_{out} &= \int_{\frac{\pi}{4}}^{\frac{3\pi}{4}} \frac{dN}{d\left(\varphi_{\text{jet}} - \psi_n^{meas}\right)} d\left(\varphi_{\text{jet}} - \psi_n^{meas}\right) + \int_{\frac{5\pi}{4}}^{\frac{7\pi}{4}} \frac{dN}{d\left(\varphi_{\text{jet}} - \psi_n^{meas}\right)} d\left(\varphi_{\text{jet}} - \psi_n^{meas}\right) \end{aligned} \tag{53}$$

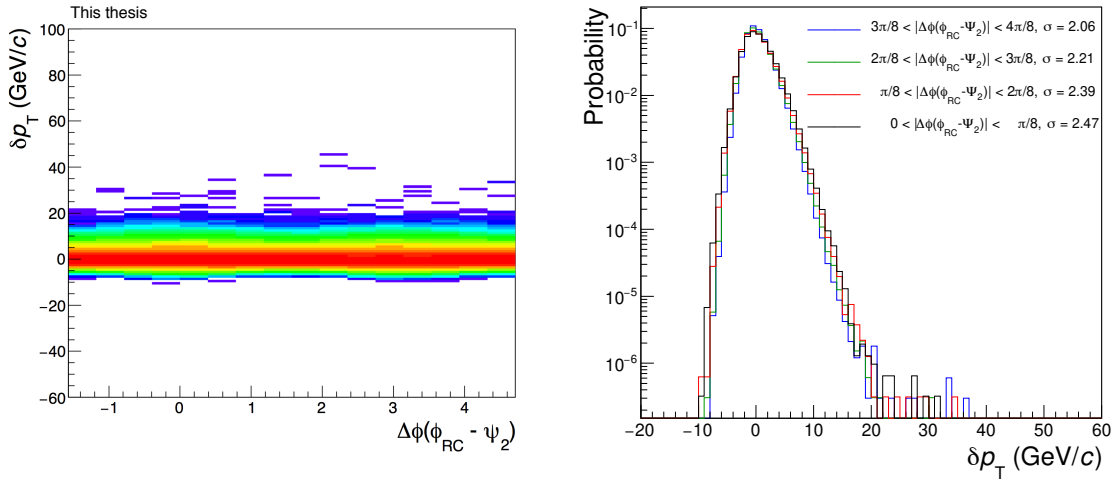

Figure 74: The δp_T distribution estimated with the RC method in 30-50% centrality Pb-Pb collisions at $\sqrt{s_{\rm NN}} = 5.02$ TeV.
Left: the 2-dimensional δp_T distribution w.r.t 2^{nd}-order V0C event plane,
Right: projections of the 2-dimensional δp_T distribution w.r.t 2^{nd}-order V0C event plane in several intervals of the angle between event plane and RC axis.

Considering only the 2^{nd}-order Fourier coefficient, the integrals can be evaluated as:

$$\begin{aligned} N_{in} &= a\left(\pi + 4v_2^{\text{jet, obs}}\right) \\ N_{out} &= a\left(\pi - 4v_2^{\text{jet, obs}}\right) \end{aligned} \tag{54}$$

where N_{in}, N_{out} are the jet yields in each $p_{\rm T}$ bin, and a is a normalization constant.

Using Eq. 54, the jet elliptic azimuthal anisotropy, $v_2^{\rm jet}$, is calculated as:

$$v_2^{\rm jet} = \frac{1}{\text{Res}\left\{\psi_2^{meas}\right\}} \frac{\pi}{4} \frac{N_{in} - N_{out}}{N_{in} + N_{out}} \ . \tag{55}$$

Using Eq. 55, the $v_2^{\rm jet}$ in mid-central (30-50%) Pb-Pb collisions is measured as a function of unfolded jet $p_{\rm T}$ spectra.

4.6.4 Charged jet-hadron correlations with respect to event plane

The two-dimensional yield of associated tracks is measured to assess jet-like correlations in Pb-Pb collisions, for the purpose of studying jet suppression and by medium response in jet-like events. The correlation function $C(\Delta\varphi, \Delta\eta)$ is given by the ratio of the jet-track pairs distribution within the same event over the one in a mixed event:

$$C(\Delta\varphi, \Delta\eta) = \frac{N_{\rm mix}^{\rm pair}}{N_{\rm same}^{\rm pair}} \left(\frac{d^2 N_{\rm same}}{d\Delta\eta d\Delta\varphi} / \frac{d^2 N_{\rm mix}}{d\Delta\eta d\Delta\varphi} \right) \tag{56}$$

where $N_{same}^{\rm pair}, N_{mix}^{\rm pair}$ are the total number of pairs of trigger-jet and associated tracks in a same and in a mixed event. N_{same}, N_{mix} are the associated jet-track pairs per bin in a same

and in a mixed event. $\Delta\varphi = \varphi^{\text{assoc}} - \varphi^{\text{trig}}, \Delta\eta = \eta^{\text{assoc}} - \eta^{\text{trig}}$ where φ^{trig}, φ^{assoc} are the azimuthal angle of the trigger jet and the associated track and η^{trig}, η^{assoc} are the pseudo-rapidity of the trigger jet and the associated track respectively. In this study, in order to construct a mixed event distribution, trigger and associates were taken from different events and therefore uncorrelated. Therefore, any structure to the correlations in the mixed event is due to detector effect instead of physics. The correlation functions are normalized to have an average value of one. In reality, the same-event distribution is smeared due to the limited detector acceptance. The mixed-event distribution of associated tracks yields should equal the product of single jet and track probabilities since pairs of triggered-jet and track in mixed events have no physical correlation but is again affected by the limited detector acceptance. Therefore, the physical correlation can be extracted by taking the ratio of the same- and mixed-event trigger-associate track distributions as shown in Eq. 56.

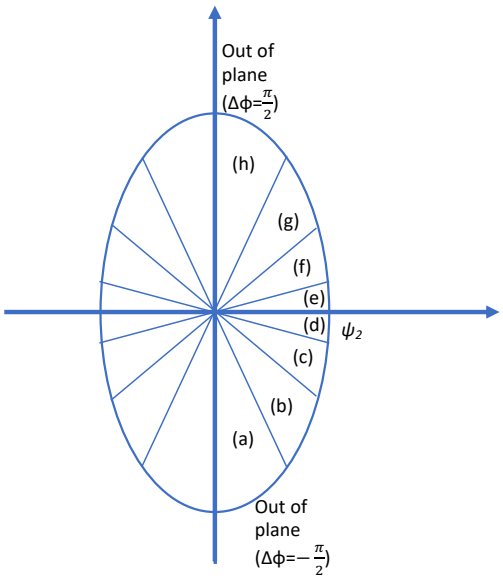

Figure 75: Classification of trigger jet events w.r.t V0C event plane. $\Delta\phi = \phi_{\text{jet}} - \psi_{2,\text{V0C}}$

In this measurement, jets with $p_{T,\text{jet}} > 20$ GeV/c after local UE subtraction were selected as triggers. In order to avoid the trivial autocorrelation among the jet axis and the jet constituent tracks, jet axis is recalculated by using the constituent tracks which has $p_{\text{T,track}} > 4$ GeV/c. The recalculated axis is determined as the center of transverse momenta of constituent tracks. In this study, two associated tracks p_{T} ranges were selected: $0.7 < p_{\text{T}}^{assoc} < 2$ GeV/c and $2 < p_{\text{T}}^{assoc} < 4$ GeV/c.

The near-side ($|\Delta\varphi| < 0.8$, $|\Delta\eta| < 0.8$) jet-hadron correlations are studied by dividing the sample into 8 classes according to the trigger jet azimuthal angle w.r.t 2^{nd}-order event plane (ψ_2) as shown in Fig. 75. In this study, $|\phi_{\rm jet} - \psi_2| < \frac{\pi}{4}$ is defined as 'in-plane', $|\phi_{\rm jet} - \psi_2| > \frac{3\pi}{8}$ is defined as 'out-of-plane' and $\frac{\pi}{4} < |\phi_{\rm jet} - \psi_2| < \frac{3\pi}{8}$ is defined as 'mid-plane'.

Fig. 76, 77 show the measured near-side jet-hadron correlation functions for $0.7 < p_{\rm T}^{assoc} < 2$ GeV/c and $2 < p_{\rm T}^{assoc} < 4$ GeV/c respectively. In the correlation plots, the near-side jet peak can be seen on top of the background distribution, that dominantly comes from flow effects associated with the event plane. The flow background distribution must be subtracted from the correlation functions in Fig. 76, 77 to isolate the correlations from hard components. In this study, the flow background distributions were determined at $1 < |\Delta\eta| < 1.5$ of the correlation functions which is called the 'side-band' region. For the 1-dimensional correlation function in azimuth, $C(\Delta\varphi)$, projection of side-band distribution is scaled by the ratio of integration intervals. The scaled side-band distribution is subtracted from the near-side distribution bin-by-bin. In this study, the scale factor is (Near-side integration interval)/(Side-band integration interval) = $(0.8\times2)/(0.5\times2) = 1.6$. For the 1-dimensional correlation function in eta, $C(\Delta\eta)$, flat background is assumed and only the background level is estimated by constant fitting to the side-band region after the scaling. Fig. 78, 79, 80, 81 shows the one-dimensional near-side peak distributions before background subtraction, the background distributions and the background subtracted distributions.

The shape, peak position w.r.t jet axis, and width of the background subtracted near-side jet peak correlation functions are discussed in this thesis.

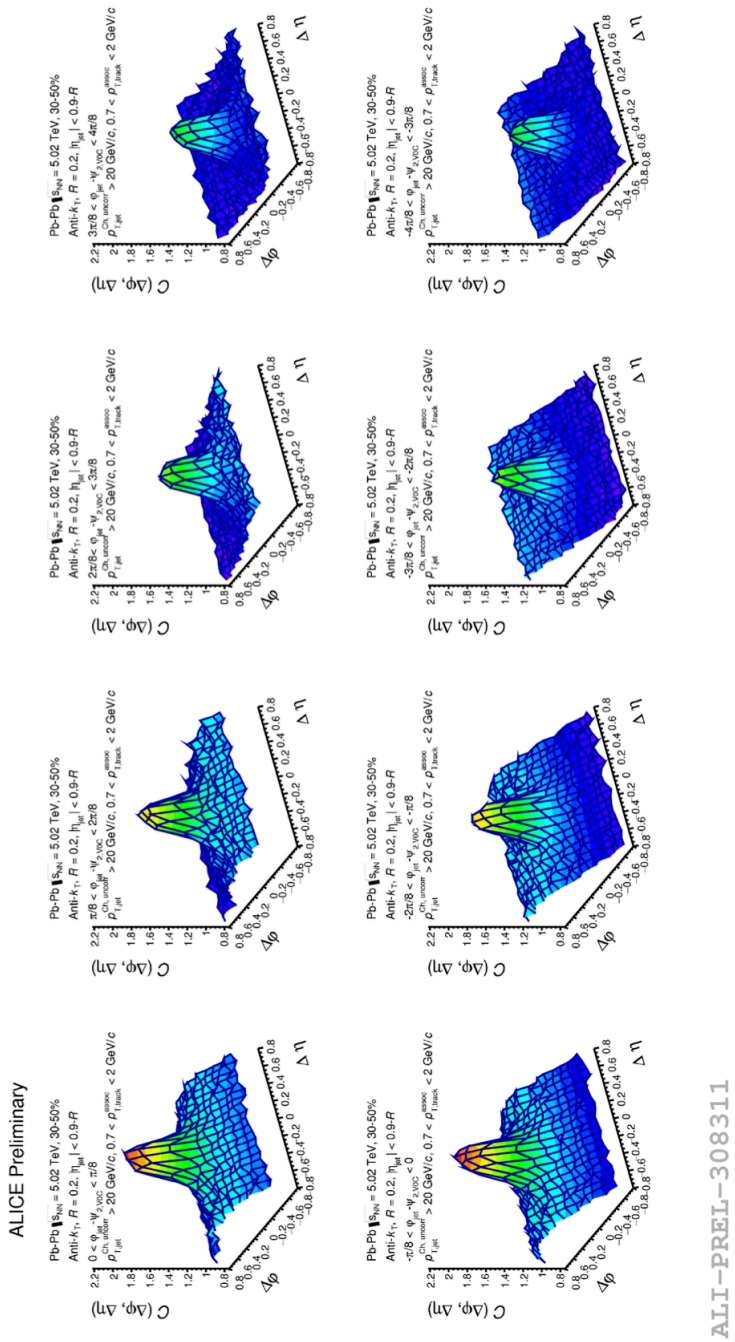

Figure 76: Near-side jet-hadron correlation functions w.r.t V0C event plane for $p_{\mathrm{T,jet}}^{\mathrm{trigger}} >$ 20 GeV/c, $0.7 < p_{\mathrm{T}}^{assoc} < 2$ GeV/c.

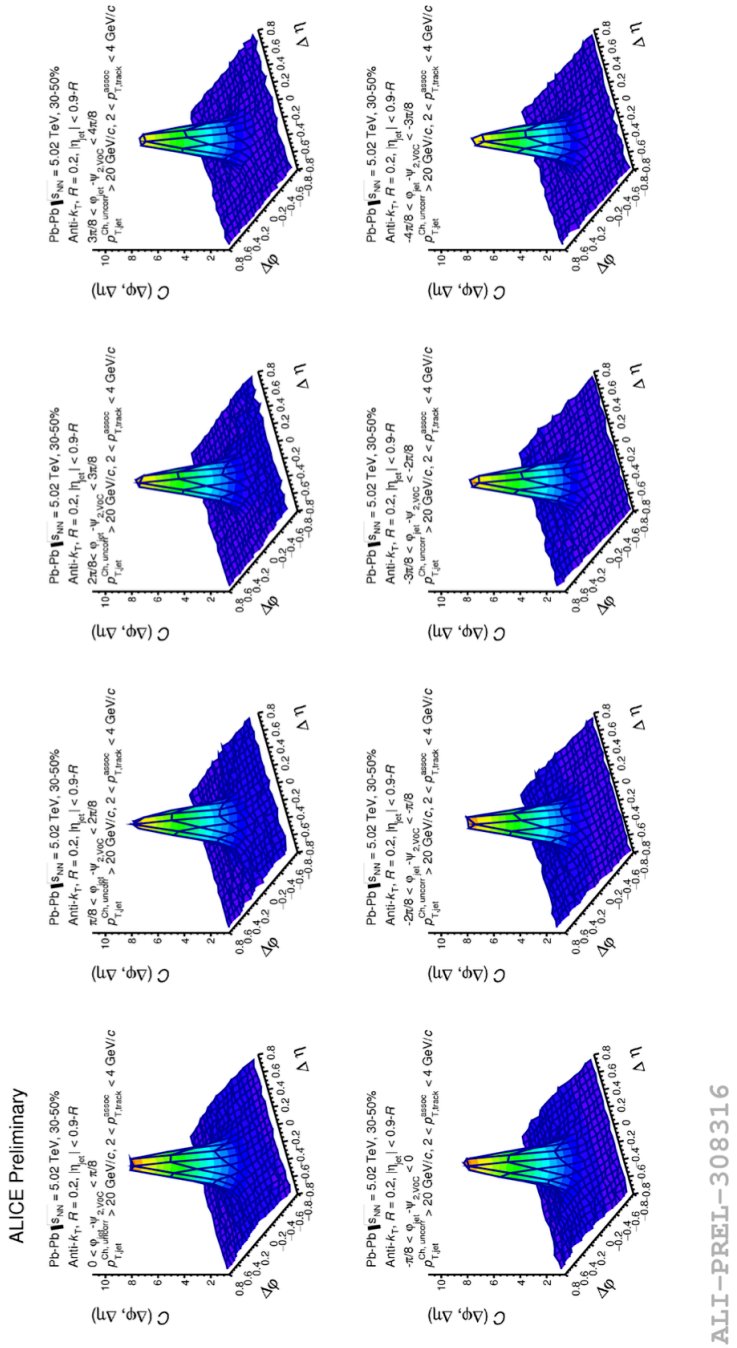

Figure 77: Near-side jet-hadron correlation functions w.r.t V0C event plane for $p_{\mathrm{T,jet}}^{\mathrm{trigger}} >$ 20 GeV/c, $2 < p_{\mathrm{T}}^{assoc} < 4$ GeV/c.

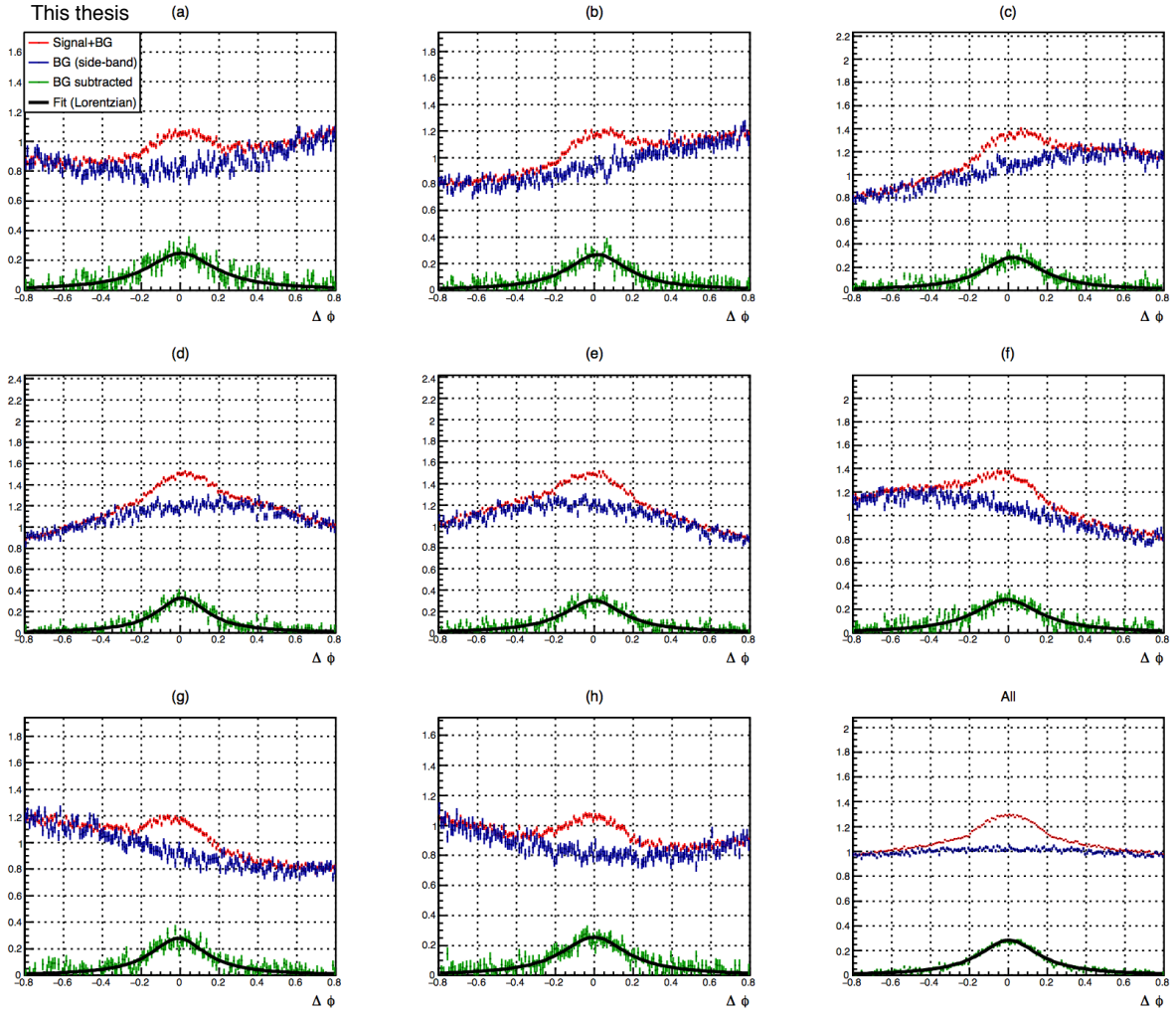

Figure 78: Near-side correlation functions as a function of $\Delta\phi$. Flow background unsubtracted distribution (Red), background distribution estimated in the side-band regions (Blue) and background subtracted distribution (Green). The unit of Y-axis is a.u. $p_{\mathrm{T,jet}}^{\mathrm{trigger}} > 20$ GeV/c, $0.7 < p_{\mathrm{T}}^{assoc} < 2$ GeV/c. The characters on top of each panel ((a)-(h)) correspond to trigger jet event classes given in Fig. 75

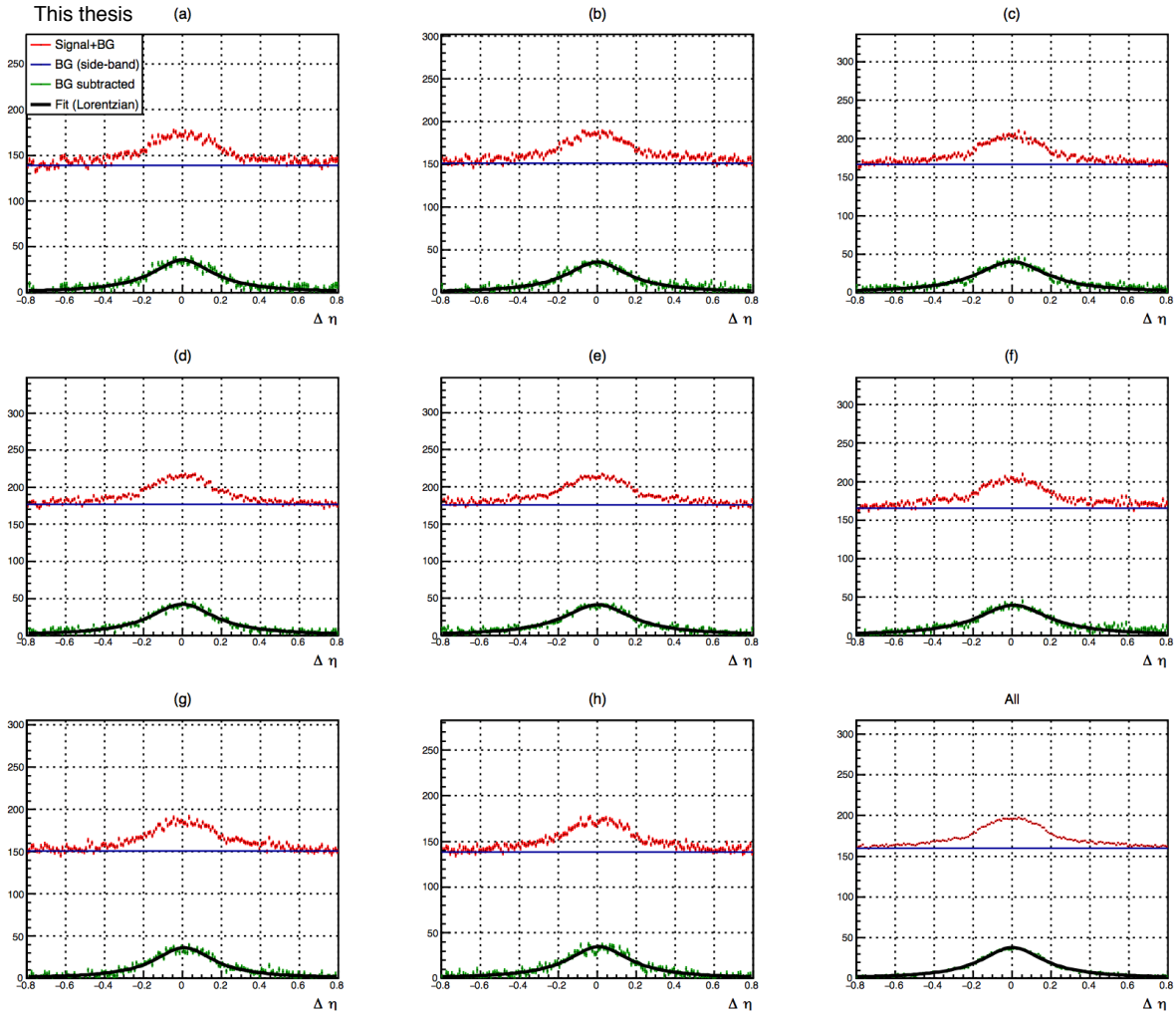

Figure 79: Near-side correlation functions as a function of $\Delta\eta$. Flow background unsubtracted distribution (Red), background distribution estimated in the side-band regions (Blue) and background corrected distribution (Green) are shown. The fitting results with Lorentzian function to the background corrected distributions are shown as black lines. The unit of Y-axis is a.u.
$p_{\mathrm{T,jet}}^{\mathrm{trigger}} > 20$ GeV/c, $0.7 < p_{\mathrm{T}}^{assoc} < 2$ GeV/c. The characters on top of each panel ((a)-(h)) correspond to trigger jet event classes given in Fig. 75

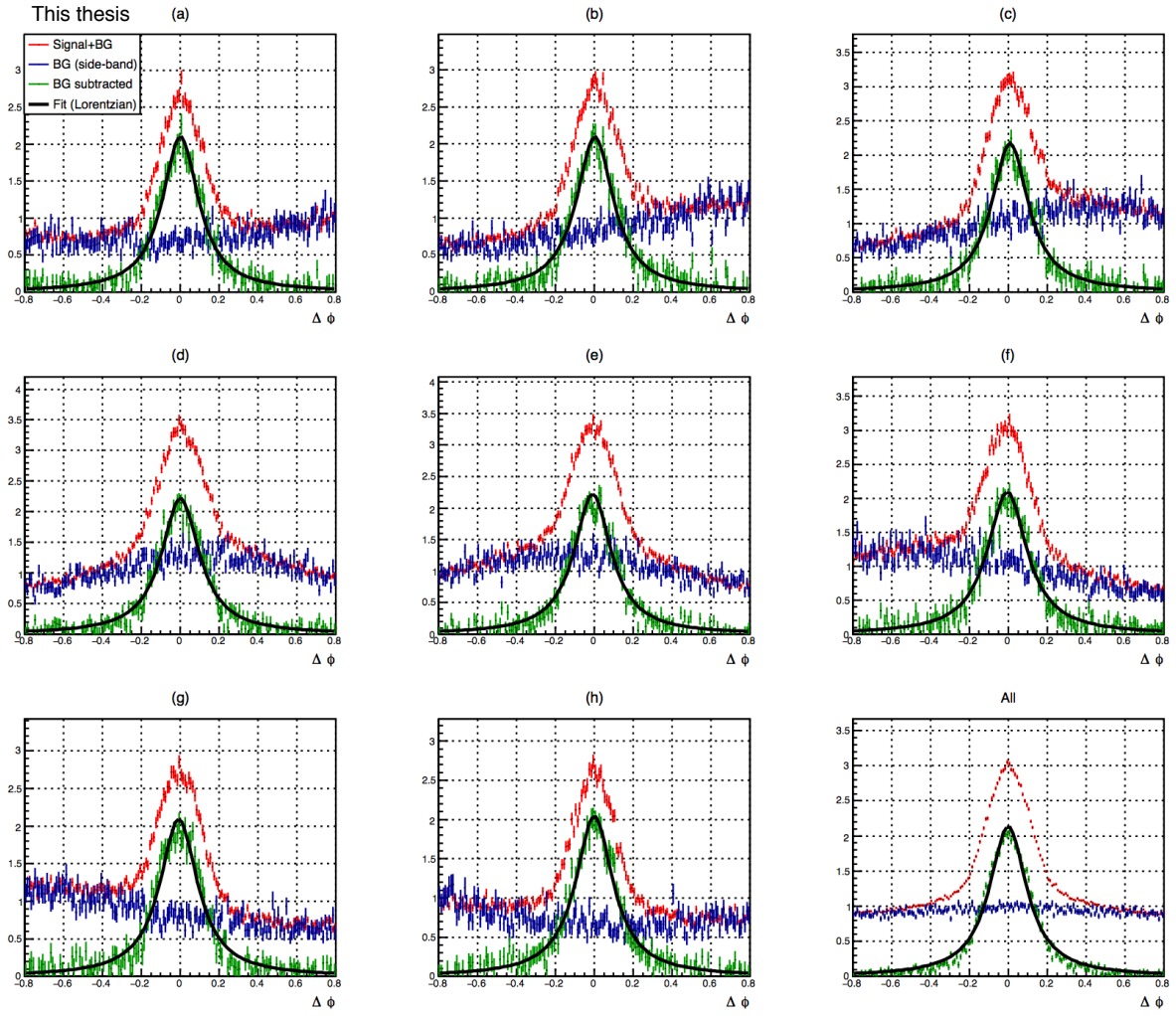

Figure 80: Near-side correlation functions as a function of $\Delta\phi$. Flow background unsubtracted distribution (Red), background distribution estimated in the side-band regions (Blue) and background subtracted distribution (Green). The fitting results with Lorentzian function to the background corrected distributions are shown as black lines. The unit of Y-axis is a.u.
$p_{\mathrm{T,jet}}^{\mathrm{trigger}} > 20$ GeV/c, $2 < p_{\mathrm{T}}^{assoc} < 4$ GeV/c. The characters on top of each panel ((a)-(h)) correspond to trigger jet event classes given in Fig. 75

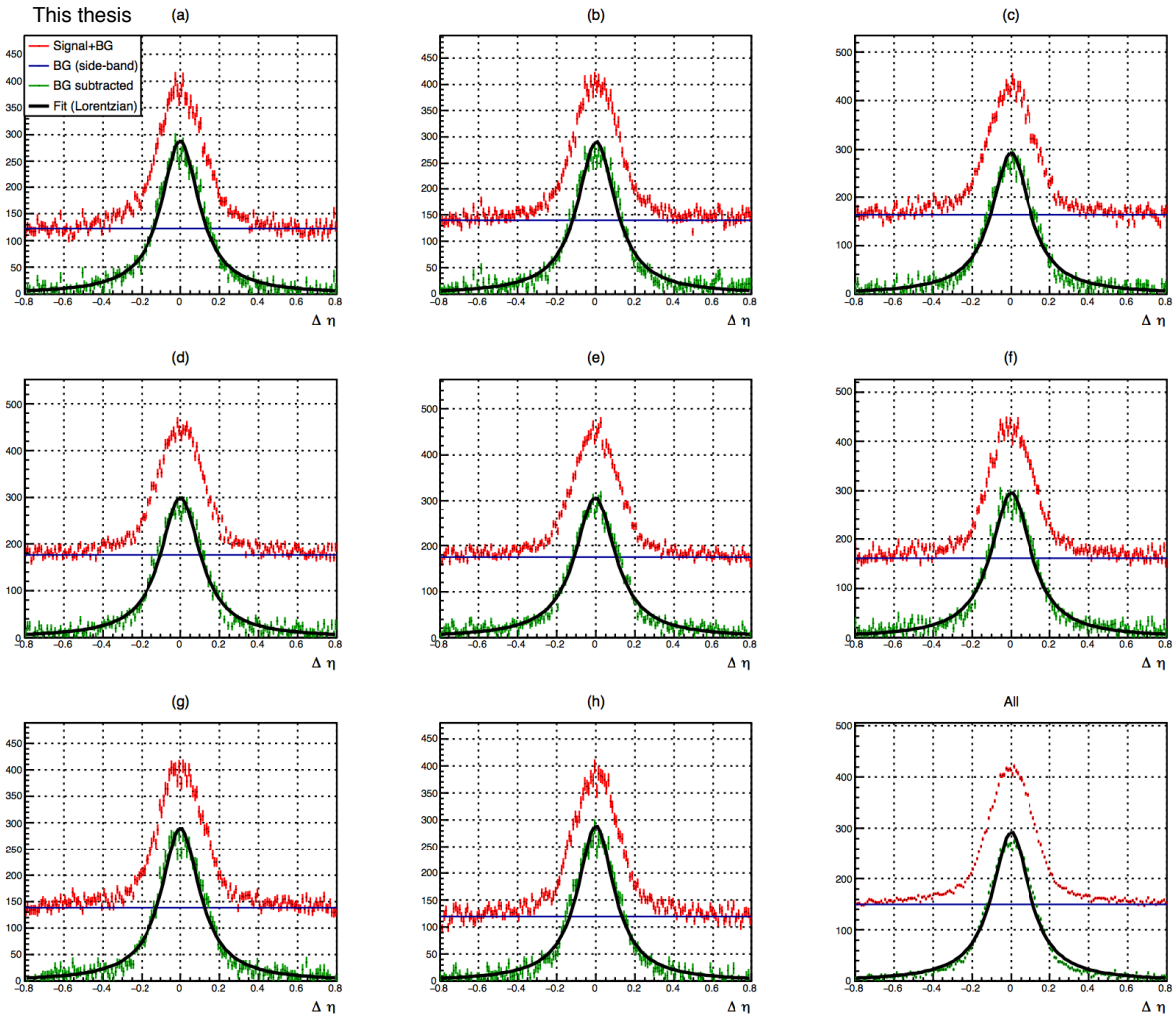

Figure 81: Near-side correlation functions as a function of $\Delta\eta$. Flow background unsubtracted distribution (Red), background distribution estimated in the side-band regions (Blue) and background corrected distribution (Green) are shown. The unit of Y-axis is a.u. $p_{\mathrm{T,jet}}^{\mathrm{trigger}} > 20$ GeV/c, $2 < p_{\mathrm{T}}^{assoc} < 4$ GeV/c. The characters on top of each panel ((a)-(h)) correspond to trigger jet event classes given in Fig. 75

Chapter 5 Systematic uncertainties

5.1 Systematics for charged jet production cross section in pp collisions

The systematic uncertainties from the following sources are considered:

- Tracking efficiency
- Tracking resolution
- Contribution from secondary particles
- Underlying event subtraction
- Unfolding
  - Choice of method
  - Choice of regularization parameter
  - Choice of event generator
- Cross section normalization

Systematics: Tracking efficiency and track momentum resolution

The measured jet spectra are corrected for tracking efficiency and momentum resolution by unfolding. A fast simulation is performed to propagate the uncertainty on the single track efficiency to the jet spectrum measurement. 'True' information of the charged final-state particles is extracted from PYTHIA events, and the particles are reduced according to a tracking efficiency parameterized as function of particle p_{T} (Fig. 82) derived from the full MC simulation. The track p_{T} is smeared with a parameterized p_{T} resolution of $\sigma(1/p_{\mathrm{T}}) = 0.002$ $(\mathrm{GeV}/c)^{-1}$. The fast simulation reproduces reasonably well the tracking efficiency obtained from the full simulation as shown in Fig. 83.

The systematic uncertainty on tracking efficiency due to hybrid track cuts used in this analysis is studied through cut variations. The cut parameters are consistently varied within the data and the full detector simulation, and the impact on the track spectra of these variations are monitored. The matching efficiency between ITS and TPC is estimated by turning on and off the matching requirement for both the data and the full detector simulation, and the impact on the track spectra of the requirement is monitored. The

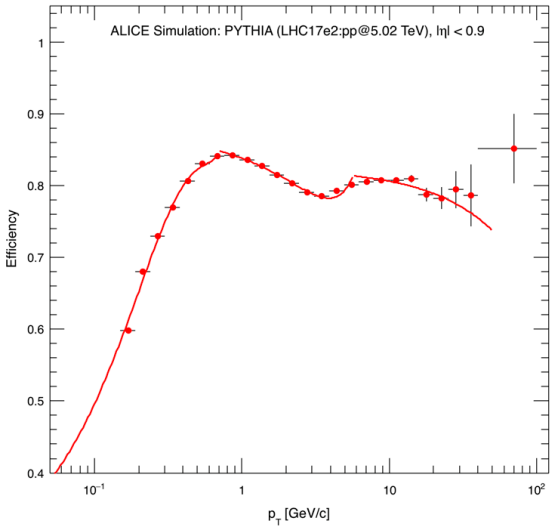

Figure 82: Parameterized tracking efficiency from full detector simulation

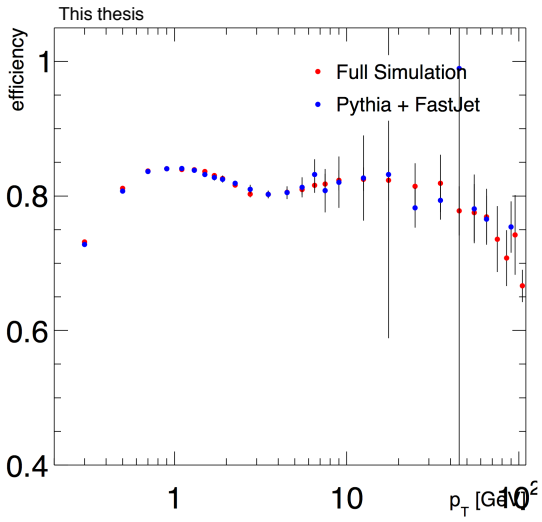

Figure 83: Comparison of tracking efficiencies from ALICE full simulation and fast simulation

combined uncertainty on single tracking efficiency due to the cut variations and the ITS-TPC matching efficiency is estimated to be 3% as a total. The uncertainty on momentum resolution is studied by comparing the tracking resolution obtained in MC and Data. A 10% uncertainty, the maximum deviation between MC and Data is assigned as Systematics on the tracking resolution for the fast-simulation study.

The systematic uncertainty from the tracking efficiency uncertainty for different jet radii is shown in Fig. 84. It increases with jet p_{T} and reaches a value of to about 10% at the highest jet p_{T} analyzed. The systematic uncertainty from p_{T} resolution uncertainty is of the order of 1-2%, as shown in Fig. 85.

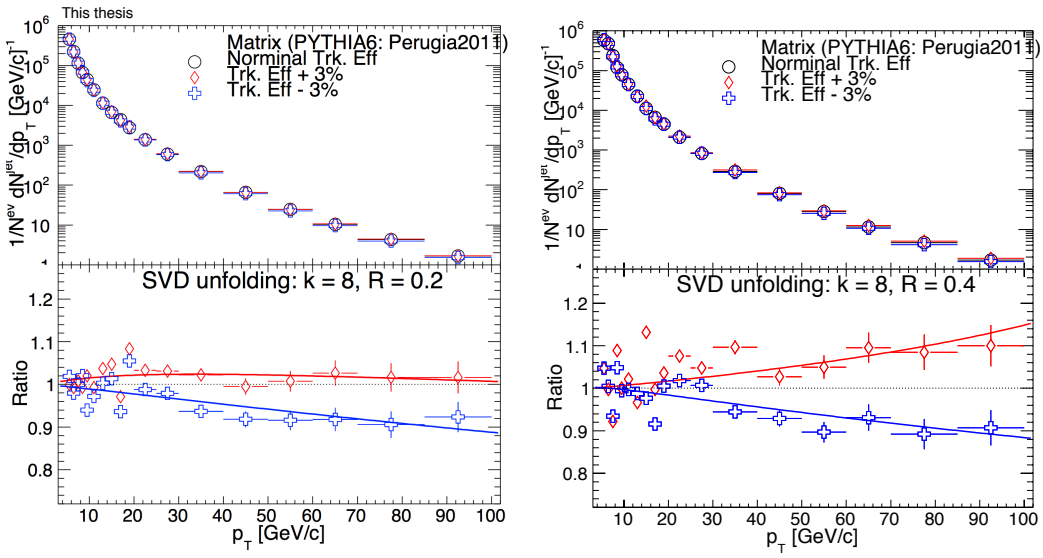

Figure 84: Systematic uncertainty from tracking efficiency uncertainty of ±3% for jet cone R = 0.2 (left), R = 0.4 (right)

Systematics: Contribution from secondary particles

Secondary particles are predominantly produced by weak decays of strange particles (e.g. K_s^0 and Λ), photon conversions or hadronic interactions in the detector material, and decays of charged pions. Conversion and hadronic interaction products are not part of the jet fragmentation. Neutral strange particles stem from fragmentation, but are not relevant for our analysis of charged particle fragmentation, but are not relevant for our analysis of charged particle fragmentation. Their decay products are considered as a contamination for our measurement.

Although in order to select primary particles preferentially the track cuts are applied on

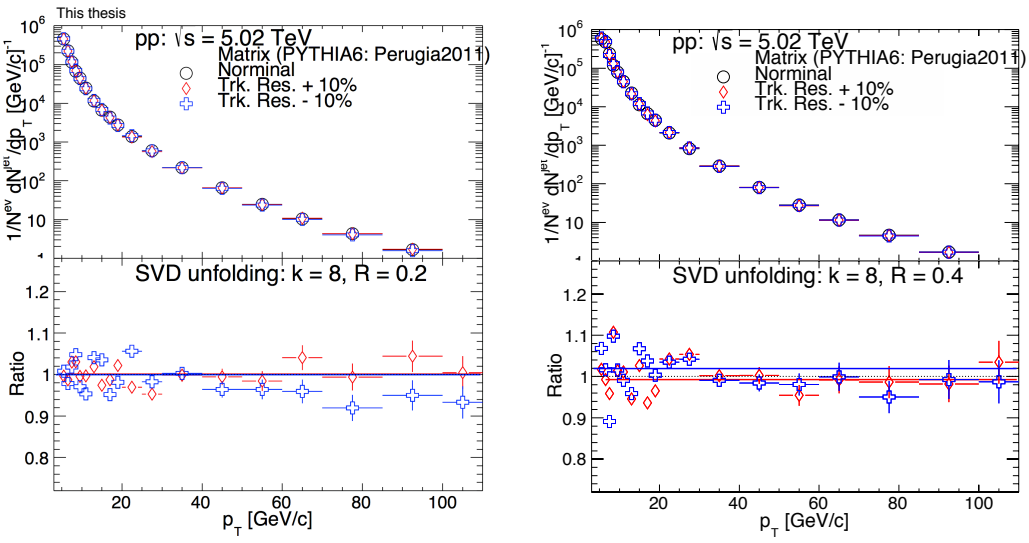

Figure 85: Systematic uncertainty from tracking resolution uncertainty for jet cone R = 0.2 (left), R = 0.4 (right)

Distance of Closest Approach (DCA) to the primary vertex, the measurements should be corrected for a small residual contamination from secondary particles. Secondary particles contribute both to the measured jet energy and jet spectra. In the MC simulations, only physical primaries are used for jet reconstruction. The jet energy scale is therefore corrected implicitly by the unfolding procedure.

We estimated the uncertainty from the contribution from secondary particles to match a jet transverse momentum scale uncertainty of 0.5%, using the same value as given in the LHC Run1 pp charged jet analysis published by ALICE [73]. To propagate this uncertainty to the measured cross section, a fit is performed with function made of double odified Tsallis functions:

$$f(x) = (p_2 + p_3 \cdot x)(1 + x/(p_0 \cdot p_1)^{-p_1} + (p_6 + p_7 \cdot x)(1 + x/(p_4 \cdot p_5)^{-p_5} \qquad (57)$$

where p_0-p_7 are free parameters and x correspons to jet p_{T}. The result of this fit is shown in Fig. 86, for R=0.2 (left) and R=0.4 (right). The ratio of the data to the fit is presented in Fig. 87 . For both values of R, the fit function gives a good description of the spectra.

To evaluate the impact of the energy scale uncertainty on the jet cross section, the arguments of the fit function are shifted by ±0.5% and use the observed variation of the spectrum is used as systematic error. The original and shifted fit functions are shown in

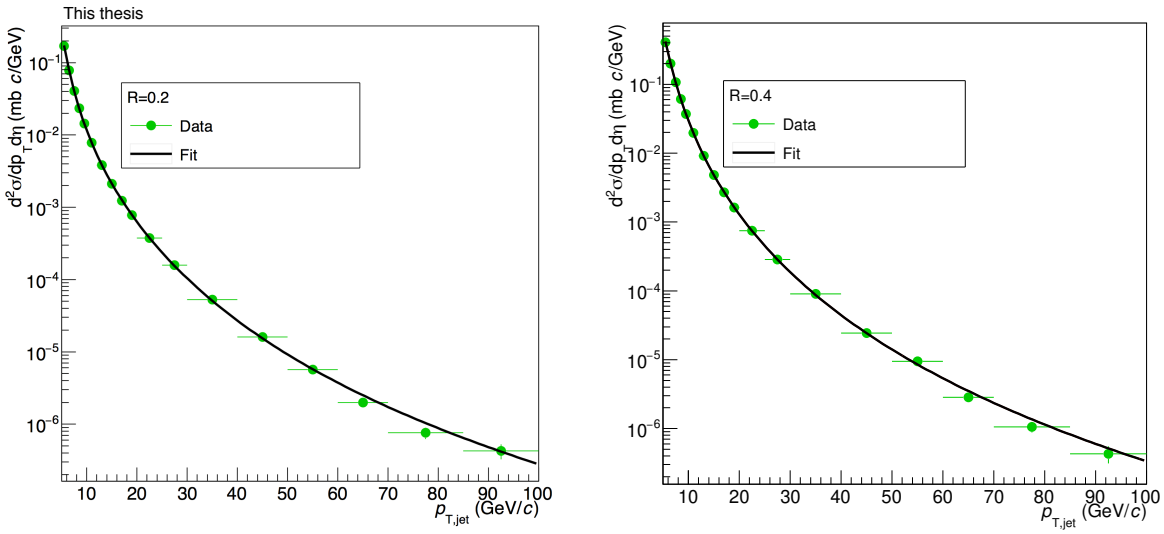

(a) Raw jet spectrum and fit R=0.2

(b) Raw jet spectrum and fit R=0.4

Figure 86: Raw jet spectra fitted with a sum of two Tsallis functions.

Fig. 88. The resulting systematic uncertainty is about 2%, with a modest increase as a function of jet p_{T}, as shown in Fig. 89.

Systematics: underlying event subtraction

The systematics associated with the measurement of the underlying event (UE) is estimated to account for 5%, as quoted in Ref. [30]. To propagate this uncertainty to the measured jet cross section, a double-Tsallis fit (see Eq. 57) is performed. The UE subtraction is modeled as a jet p_{T} shift of the spectrum. The estimated raw underlying event p_{T} density as function of leading jet p_{T} is shown in Fig. 90.

The UE 'unsubtracted' (raw) and 'subtracted' (shifted) fit functions are shown along with the measured spectra in Fig. 91. The ratio of both functions is shown in Fig. 92, and compared with the ratio of the measured spectra. The effect of the UE subtraction increases with decreasing jet p_{T}. The exact magnitude of the shift is adjusted via a constant 'fudge factor' tuned to reproduce the data spectral ratio well, and indeed, this results show a good agreement between fit+shifted result and measured result. The systematic uncertainty is evaluated by changing the spectral shift of the fitted function by the underlying event uncertainty of $\pm$ 5%. The resulting variation of the jet cross section is 1-1.5% at the low p_{T}, and decrease with increasing jet p_{T}. For example, the systematic uncertainties from

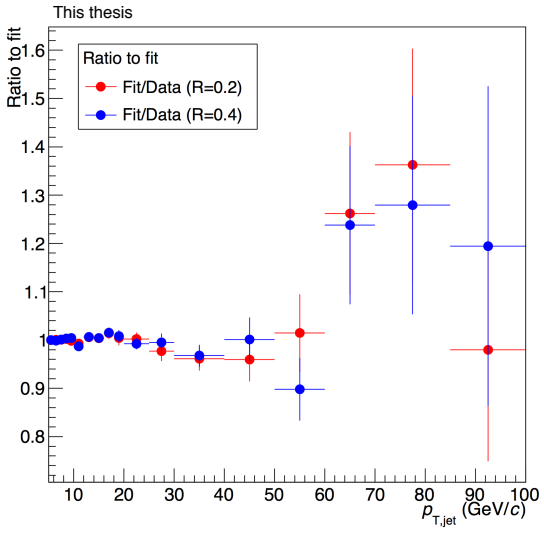

Figure 87: Ratio of spectra to fit

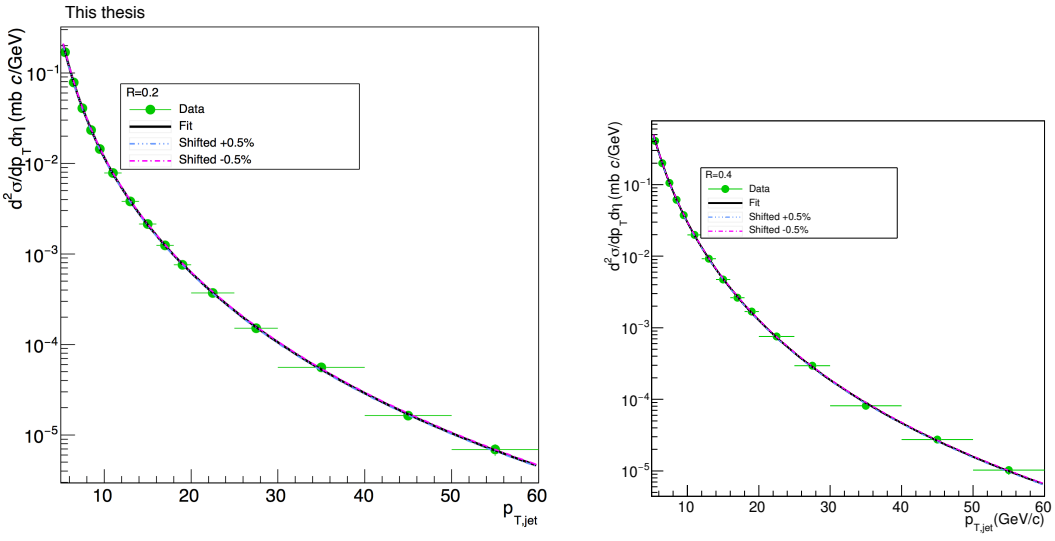

(a) Secondary:Shifted and unshifted fit spectrum R=0.2(b) Secondary:Shifted and unshifted fit spectrum R=0.4

Figure 88: Shifted and unshifted fit spectrum assuming secondary contribution

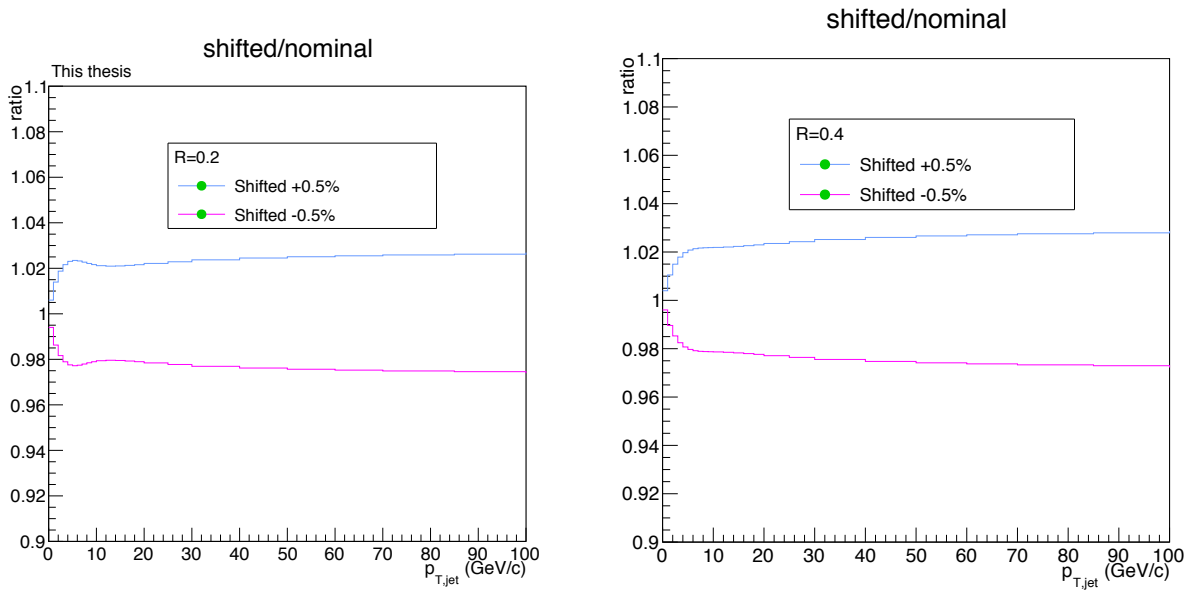

(a) Secondary:Systematic uncertainty R=0.2

(b) Secondary:Systematic uncertainty R=0.4

Figure 89: Systematic uncertainty from secondary contribution to jet spectra

UE subtraction for R=0.2 and 0.4 jets are shown in Fig. 93.

Systematics: Unfolding

Choice of method

As a cross-check and validation of the unfolding method, we compared our results by SVD unfolding with the results obtained with the iterative Bayes method implemented in RooUnfold. The iterative Bayes unfolding is regularized by choosing a number of iterations for unfolding procedure. The ratio of spectra unfolded with the iterative Bayes method for different choices of the regularization parameter to the default (SVD) is shown in Fig. 94. Since the different methods are applied to the same raw input spectra, and hence numerator and denominator of the ratio are strongly correlated, we used binomial errors for statistical uncertainties. Within uncertainties, the solutions from both unfolding methods are in excellent agreement. To smoothen the statistical fluctuations in the determination of the systematic error, we fitted bin-by-bin the absolute deviation from 0 and used a linear fir function, resulting in an uncertainty of a few percent.

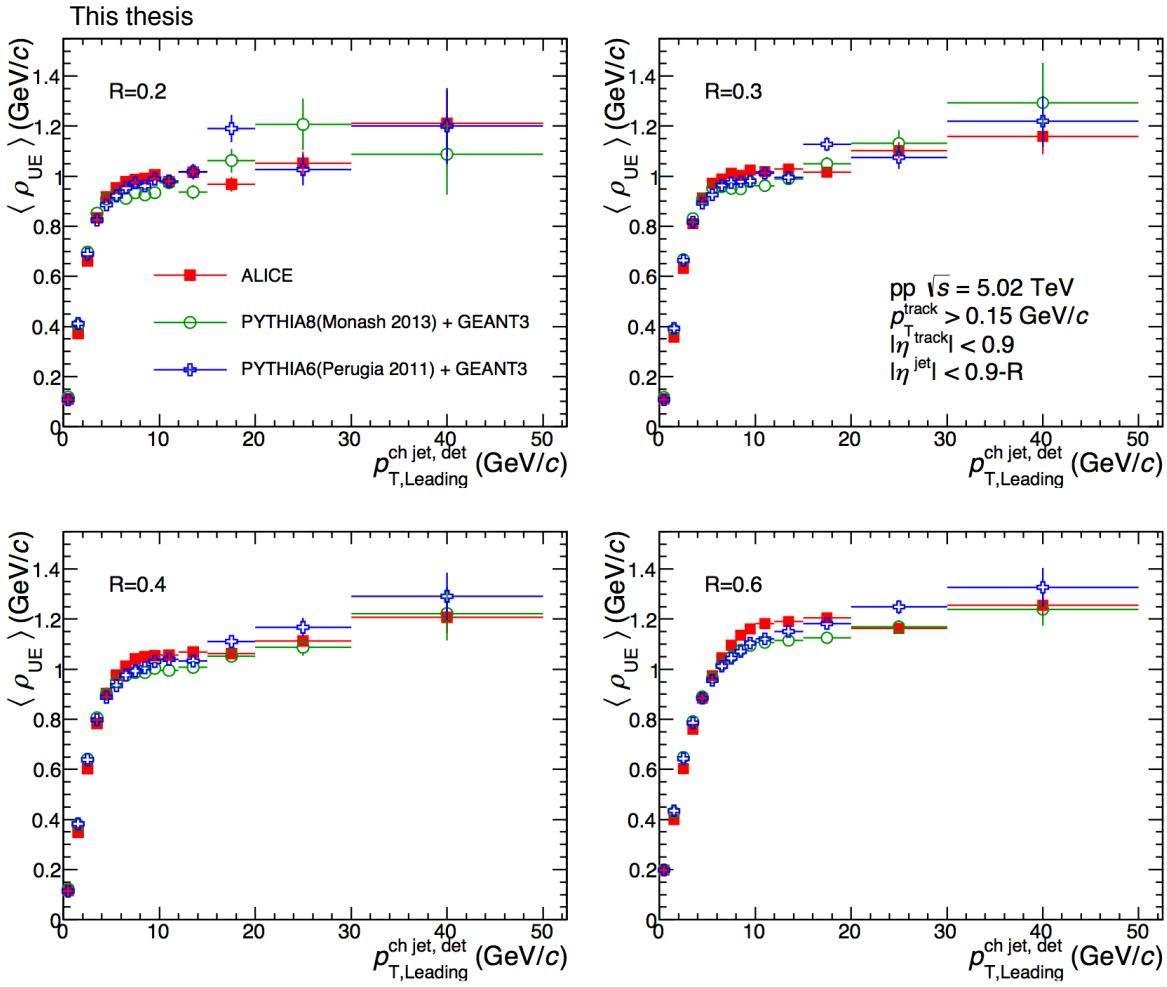

Figure 90: The average of underlying event p_{T} density estimated by the perpendicular cone as a function of leading jet p_{T}.

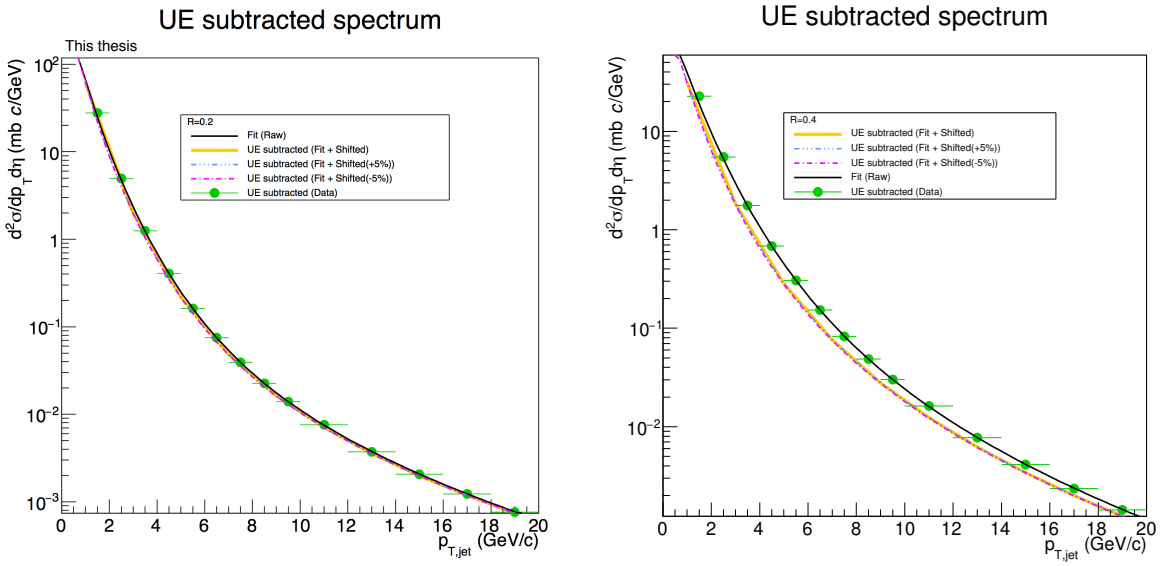

(a) UE:Shifted and unshifted fit spectrum R=0.2 (b) UE:Shifted and unshifted fit spectrum R=0.4

Figure 91: Shifted and unshifted fit spectra assuming uncertainty on UE measurement

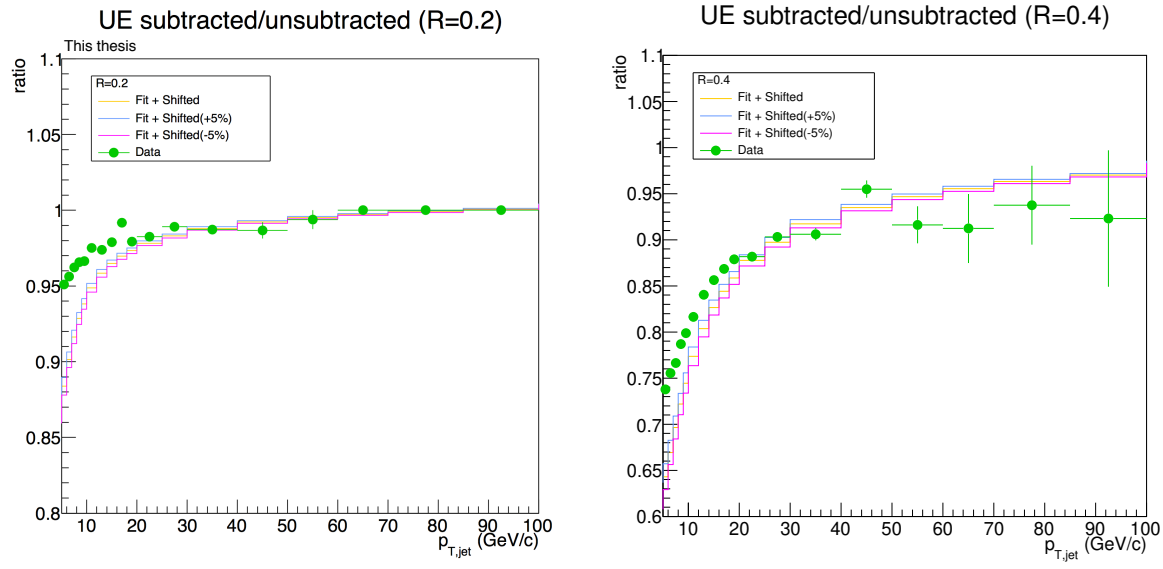

(a) UE:Ratio of shifted to unshifted spectrum R=0.2 (b) UE:Ratio of shifted to unshifted spectrum R=0.4

Figure 92: Ratio of shifted to unshifted fit spectra

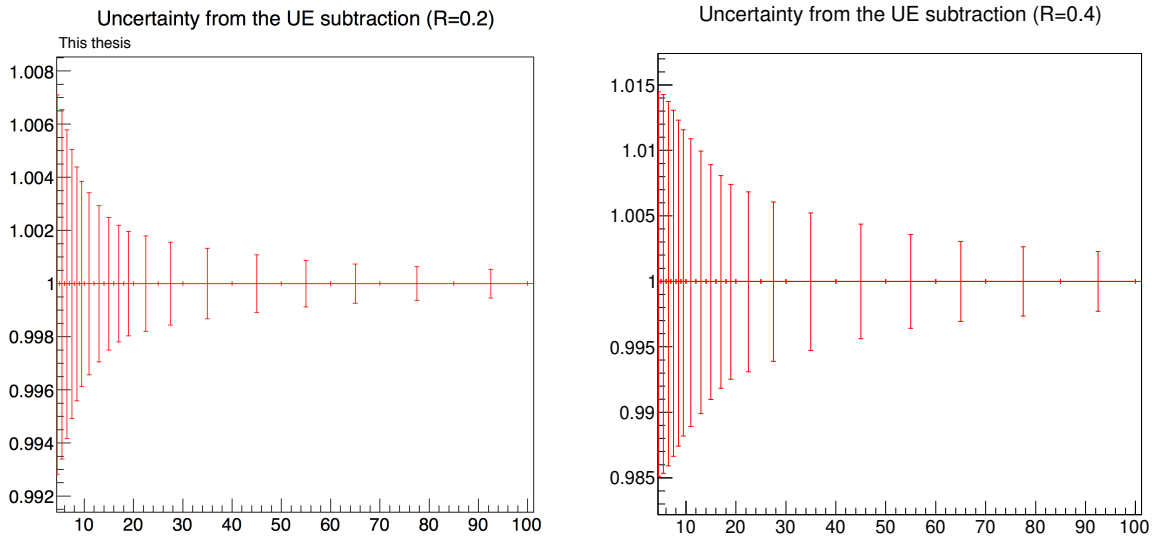

(a) UE:Systematic uncertainty R=0.2

(b) UE:Systematic uncertainty R=0.4

Figure 93: Systematic uncertainty in the jet cross section from Underlying event subtraction

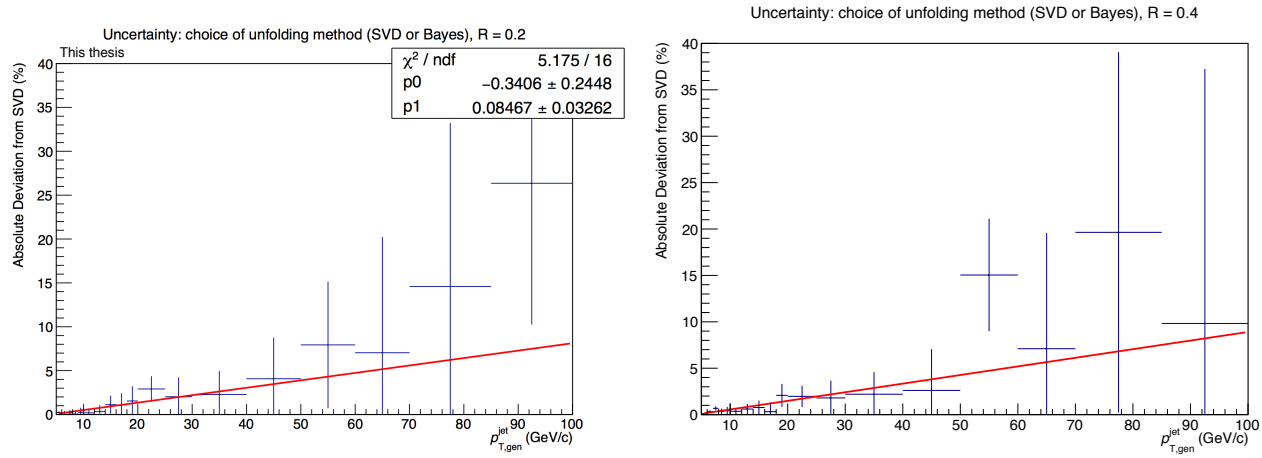

(a) Unfolding: Uncertainty from choice of unfolding method R=0.2

(b) Unfolding: Uncertainty from choice of unfolding method R=0.4

Figure 94: Systematic uncertainty from the choice of unfolding method. The lines in the figure represent fit results with linear function and the values at the bin centers are assigned as the bin-by-bin systematic uncertainties.

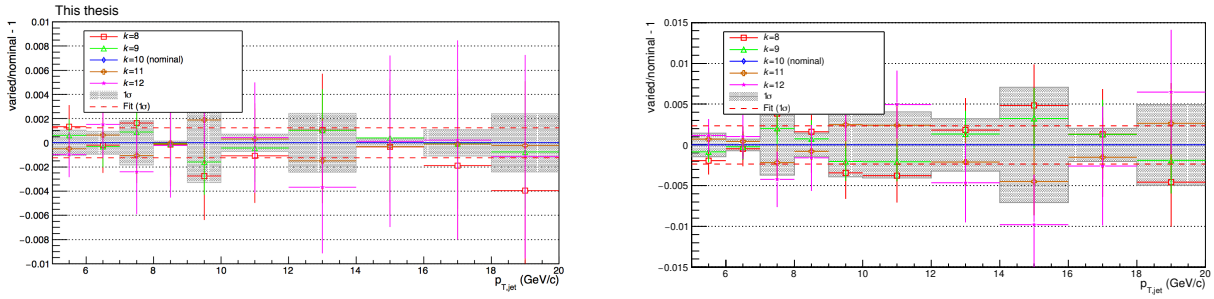

(a) Unfolding: Difference from nominal regularization parameter (R=0.2)

(b) Unfolding: Difference from nominal regularization parameter (R=0.4)

Figure 95: Systematic uncertainty from the choice of regularization parameter k by varying nominal ± 2 in the p_{T} range of 5-20 (GeV/c)

Choice of regularization parameter

The SVD unfolding is regularized by a choice of an integer valued parameter which separates statistically significant and non significant singular values of the orthogonalized response matrix. The choice is made by looking at the behavior of the so-called 'd-vector' [74, 65], which is not unambiguous. To estimate the related systematic uncertainties, we varied the regularization parameter by $\pm$ 2. The resulting variations are shown in Fig. 95 and Fig. 96 for 5$<$ p_T^{jet} $<$20 GeV/c and 20 GeV/c$<$ p_T^{jet} respectively. The differences are of the order of 1-2%.

Choice of event generator

In this section we discuss the uncertainties related to the choice of the MC event generator used for calculating the detector response matrix. Compared to a bin-by-bin correction, the unfolding should have a small generator dependence. However, differences in the simulated jet spectra and jet fragmentation between different event generators can induce differences in the jet response matrix and the prior used for the unfolding (in RooUnfold, the training sample is used to derive the prior).

Our method to estimate this uncertainty is based on a fast simulation, as described in 5.1. We simulated PYTHIA events, extracted the charged final-state particles, applied particle-by-particle a parameterized tracking efficiency and p_T resolution and used the FastJet anti-k_{T} algorithm to cluster both the original 'particle level' tracks and the 'reconstructed level' tracks to obtain the detector response matrix. To estimate the uncertainty, we used different PYTHIA tunes. We unfolded the measured spectrum with the

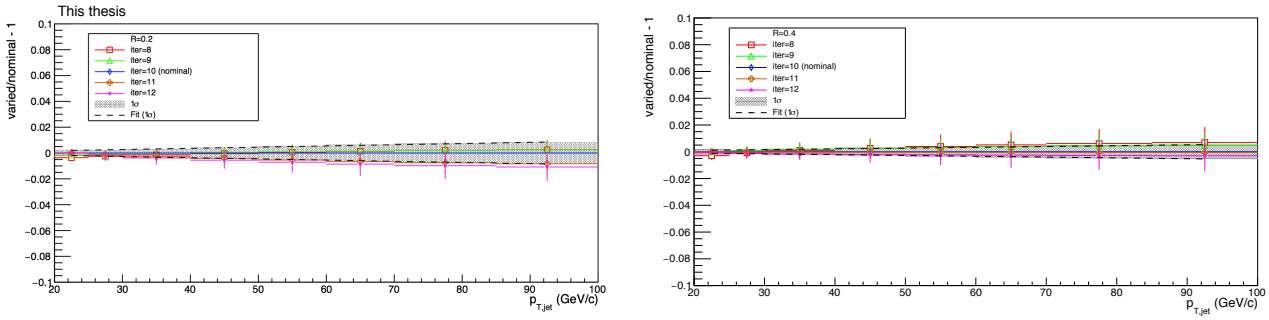

(a) Unfolding: Difference from nominal regularization parameter R=0.2

(b) Unfolding: Difference from nominal regularization parameter R=0.4

Figure 96: Systematic uncertainty from the choice of regularization parameter k by varying nominal ± 2 in the p_{T} range of 20-100 (GeV/c)

response matrix for each tune/generator, and used the ratio to the nominal PYTHIA tune to estimate the uncertainty. The resulting uncertainties are the order of 5-10% at maximum, as shown in Fig. 97.

Systematics: Cross section normalization

The visible inelastic pp cross section at $\sqrt{s} = 5.02$ TeV, measured by VdM scans at ALICE, is:

$$\sigma_{\mathrm{V0}} = 51.2 \pm 1.2 \text{ mb (syst.)}$$

corresponding to a normalization systematic uncertainty of 2.3%.

Summary of systematics

The systematics of charged jet differential production cross section is summarized in Table 4. The quadratic sum of uncertainties from individual systematic uncertainty sources are assigned as total systematic uncertainty.

5.2 Systematics for charged jet v_2 in Pb-Pb collisions

In this measurement, the systematic uncertainties from the following sources are considered as in Ref.[36]:

- Shape uncertainties:
  - Unfolding
  - Jet $p_{\mathrm{T}}^{\mathrm{ch}}$-measured

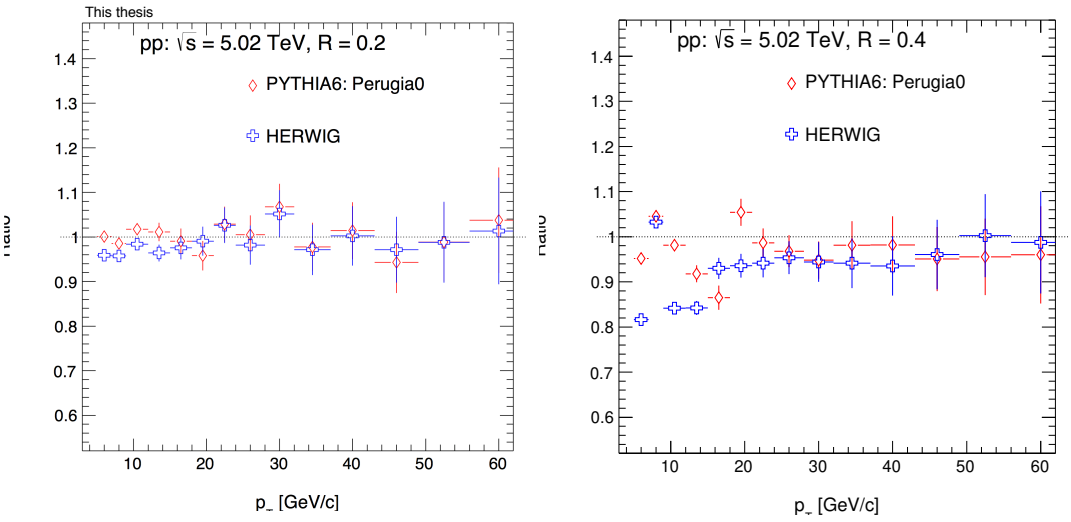

Figure 97: Systematic uncertainty from the choice of event generator for jet cone R = 0.2 (left) and R = 0.4 (right), showing the ratio to nominal PYTHIA8 Monash 2013 tune.

  - $\rho_{\mathrm{ch}}(\varphi)$ fit

- Correlated uncertainties:

  - Tracking
  - Jet $p_{\mathrm{T}}^{\mathrm{ch}}$-unfolded

Since the same ALICE detector and analysis method are used for the jet v_2^{jet} measurement in Pb-Pb collisions at $\sqrt{s_{\mathrm{NN}}} = 2.76$ TeV [36], the relative uncertainties are taken from this previous study.

5.3 Systematics for charged jet-hadron correlation in Pb-Pb collisions

In this measurement, the systematic uncertainties from the following sources are considered:

- Method of flow background shape estimation
- Jet p_{T} correction for UE
- Event classification for event mixing.
- Peak shape estimator

Jet resolution parameter	Jet p_{T} bin (GeV/c)	Track efficiency (%)	Track p_{T} resolution (%)	Unfolding (%)	Normalization (%)	Secondaries (%)	Total (%)
$R = 0.2$	5−6	1	negl.	1.4	2.3	2.4	3.7
	20−25	2.6	negl.	2.3	2.3	2.2	4.7
	40−50	5.2	negl.	3.8	2.3	2.5	7.3
	85−100	10	negl.	7.8	2.3	2.6	13.1
$R = 0.3$	5−6	1.5	0.1	2.9	2.3	2.2	4.6
	20−25	4.1	0.1	3.4	2.3	2.3	6.3
	40−50	6.2	0.1	4.3	2.3	2.6	8.3
	85−100	8.4	0.1	7.0	2.3	2.7	11.5
$R = 0.4$	5−6	0.9	1.9	1.9	2.3	2.1	4.2
	20−25	3.7	1.9	1.8	2.3	2.4	5.6
	40−50	5.4	1.9	2.5	2.3	2.5	7.2
	85−100	7.5	1.9	4.5	2.3	2.8	9.6
$R = 0.6$	5−6	3.4	1	2.1	2.3	1.9	5.1
	20−25	5.7	1	1.7	2.3	2.6	6.9
	40−50	6.8	1	2.2	2.3	2.6	8
	85−100	8.3	1	4.0	2.3	2.7	9.9

Table 4: Summary of the systematic uncertainties in jet cross section for R=0.2-0.6 and in various of jet transverse momentum ranges.

Systematics: Method of flow background shape estimation

The underlying background distribution in the correlation function, which is dominated by flow effect, is estimated by a side-band method for this study. As a systematic study, the following methods are tested:

- Narrower side-band subtraction :
  Basically, same as the nominal side-band subtraction method but the background distribution is estimated in a narrower η range ($1.1 < |\eta| < 1.3$)

- Fitting at side-band region :
  Fitting is performed on background-dominated distributions in the nominal side-band region ($1 < |\eta| < 1.5$). The fit range is restricted to $|\Delta\phi| < \pi/2$ to avoid contributions from the away-side peak. Fit results are subtracted from the raw distribution instead of side-band distributions directly. The following function is tested for this systematic study (see Fig. 98):

$$f(x) = B\left[1 + \sum_{n} 2v_n^t v_n^a \cos(x - a)\right] \tag{58}$$

  where B, v, a are free parameters and n = 2-4.

- Flow MC simulation :
  The flow BackGround (BG) distribution is estimated with a Monte-Calro (MC) method based on the measured v_2, v_3 of inclusive hadron and jet, as well as two particle correlation studies done by the PHENIX Collaboration [75]. The background levels between the data and MC distributions are adjusted based on the Zero-Yield-At-Minimum (ZYAM) assumption. The minimum point of the data distribution is estimated in the side-band region ($1 < |\eta| < 1.5$).

The discrepancy between these results and the nominal side-band method is calculated and the RMS assigned as the systematic uncertainty. Fig. 99 shows an example of flow MC simulation results compared to the nominal side-band distribution. The flow background shape estimation is the major source of systematic uncertainties of this jet-hadron correlation measurement.

Systematics: Jet p_{T} correction for UE

Local underlying p_{T} is subtracted from jet p_{T} but the background fluctuation effect in-plane and out-of-plane still have to be considered. To assess the effect from trigger jet p_{T} determination, all observables are calculated with uniform background p_{T} subtraction method (median of k_{T} cluster is used as uniform background density estimator) as a test of extreme case and the discrepancy from nominal result is assigned as systematic uncertainty.

Systematics: Event classification for event mixing

For the acceptance correction with event mixing, the events are divided into 10% centrality intervals and 2 cm z_{vertex} intervals as a nominal selection. As a systematic study of event mixing, 5% centrality and 1 cm z_{vertex} intervals are tested. The RMS of discrepancies from nominal result is assigned as systematic uncertainty.

Systematics: Peak shape estimator

A fit is performed to extract quantities of peak shape. Fig. 99 shows an example of peak fitting with Gaussian. Lorentz function gives a better description of the Near-side peak shape than Gaussian (see Fig. 80). So, the Lorentz function is employed as nominal peak shape estimator. The Lorentzian function has 3 parameters: the location parameter (peak position), the peak height and the FWHM. The FWHM parameter, which express the 'width', cannot be directly compared with σ of a Gaussian. However, only the ratio of width between in-plane and out-of-plane is focused in this study. The ratio will be comparable and, in fact, the both results with Gaussian and Lorentzian function fits are comparable within statistical errors. Here, the discrepancy between the peak shapes estimated from the

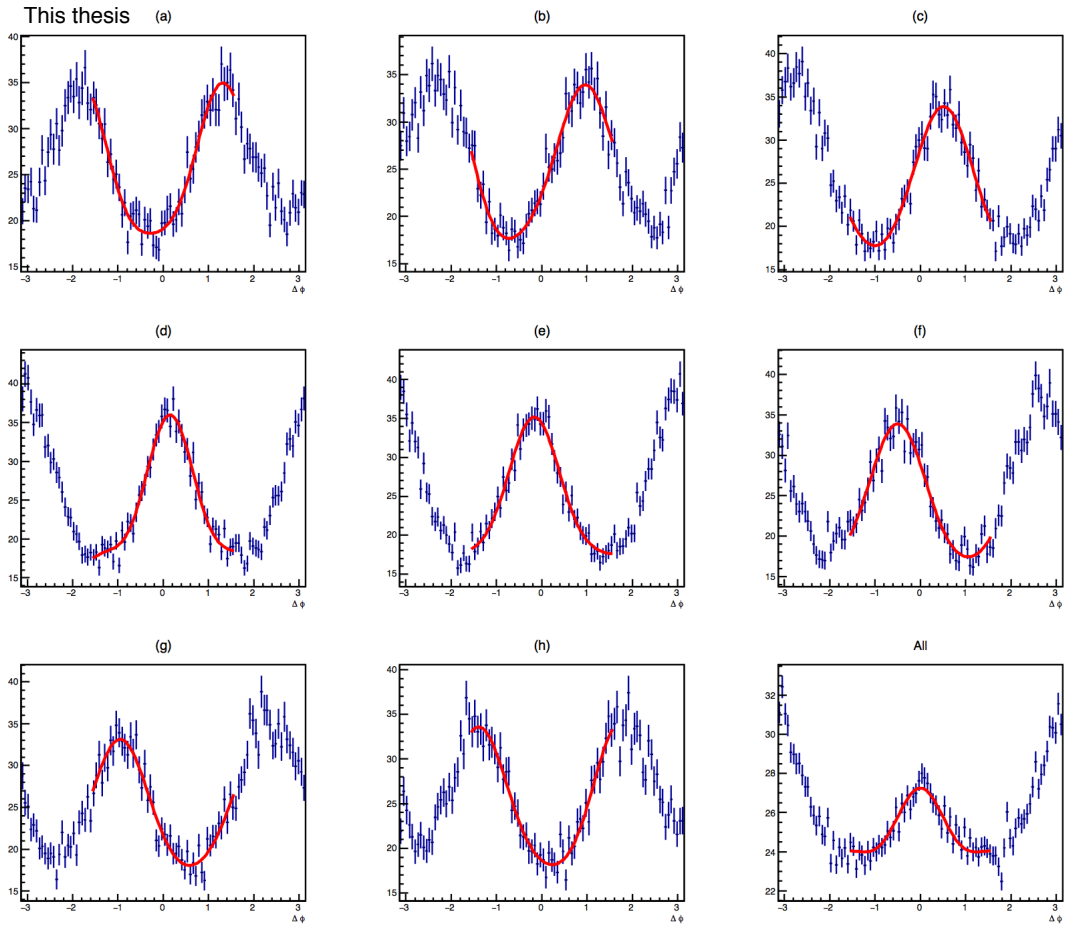

Figure 98: An example of flow shape fit in the side-band region for $p_{\mathrm{T,jet}} > 20$ GeV/c, $2 < p_{\mathrm{T,track}}^{\mathrm{assoc}} < 4$GeV/$c$. The characters attached to top of each panels are defined in Fig. 75. The y-axis is expressed in arbitrary unit.

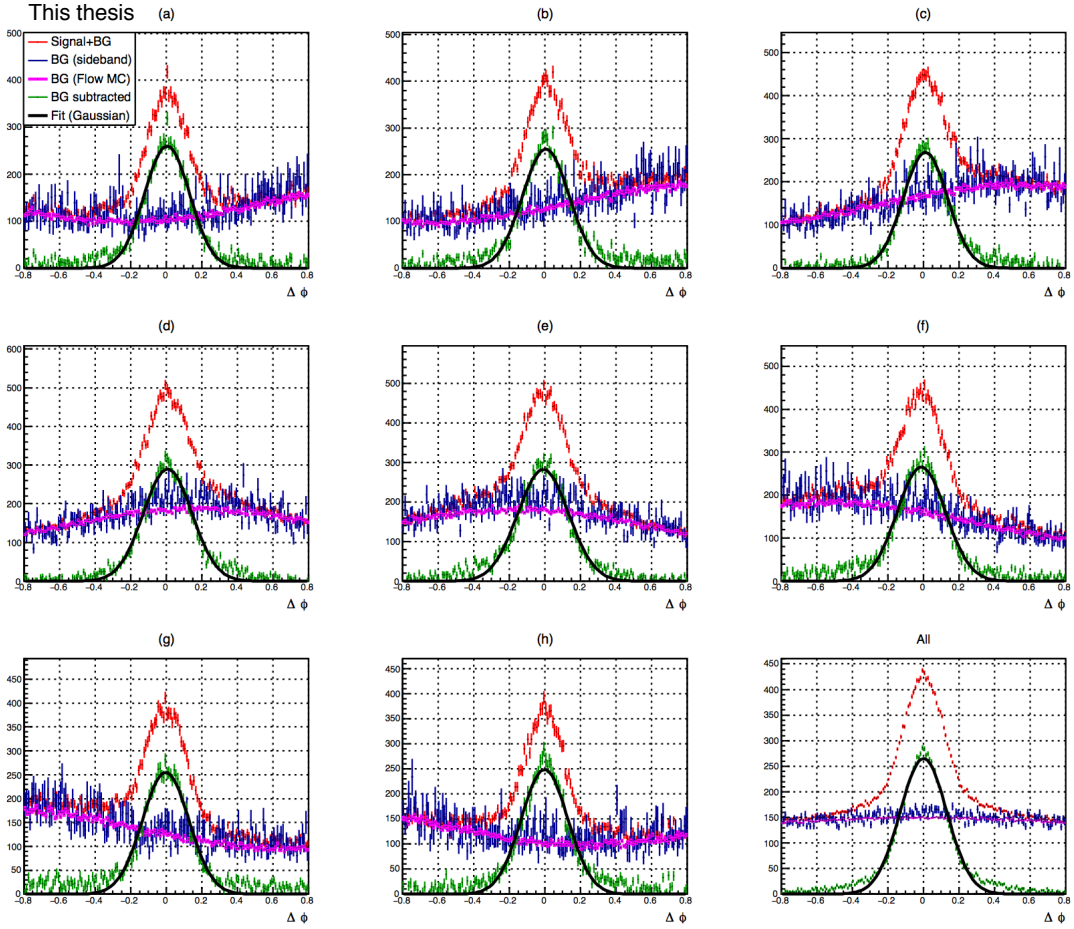

Figure 99: An example of flow shape MC simulation and peak fitting with Gaussian for $p_{\mathrm{T,jet}} > 20$ GeV/c, $2 < p_{\mathrm{T,track}}^{\mathrm{assoc}} < 4$GeV/$c$. The characters attached to top of each panels are defined in Fig. 75. The y-axis is expressed in arbitrary arbitrary unit.

two fit functions are considered as systematics for peak shape (Peak position, width ratio) extraction.

Summary of systematics

The calculated systematic uncertainties for correlation functions are summarized in Tab. 5-12. The quadratic sum of uncertainties from individual systematic uncertainty sources are assigned as total systematic uncertainty.

$\Delta\varphi$	(-0.7, -0.6)	(-0.3, -0.2)	(0.1, 0.2)	(0.5, 0.6)
Flow BG (%)	72	13	9	62
Event mixing (%)	6	5	2	8
UE estimation (%)	18	10	2	37
Total uncertainty (%)	74	17	9	73

Table 5: Systematic uncertainties of in-plane correlation function in various $\Delta\varphi$ bins. $p_{\mathrm{T,jet}} > 20(\mathrm{GeV}/c)$, $p_{\mathrm{T}}^{\mathrm{assoc}}$ =0.7-2(GeV/c).

$\Delta\varphi$	(-0.7, -0.6)	(-0.3, -0.2)	(0.1, 0.2)	(0.5, 0.6)
Flow BG (%)	21	7	2	15
Event mixing (%)	10	5	1	12
UE estimation (%)	28	3	3	7
Total uncertainty (%)	36	9	4	20

Table 6: Systematic uncertainties of out-of-plane correlation function in various $\Delta\varphi$ bins. $p_{\mathrm{T,jet}} > 20(\mathrm{GeV}/c)$, $p_{\mathrm{T}}^{\mathrm{assoc}}$ =0.7-2(GeV/c).

$\Delta\varphi$	(-0.7, -0.6)	(-0.3, -0.2)	(0.1, 0.2)	(0.5, 0.6)
Flow BG (%)	78	2	2	35
Event mixing (%)	6	2	1	55
UE estimation (%)	6	3	1	37
Total uncertainty (%)	78	4	2	75

Table 7: Systematic uncertainties of in-plane correlation function in various $\Delta\varphi$ bins. $p_{\mathrm{T,jet}} > 20(\mathrm{GeV}/c)$, $p_{\mathrm{T}}^{\mathrm{assoc}}$ =2-4(GeV/c).

$\Delta\varphi$	(-0.7, -0.6)	(-0.3, -0.2)	(0.1, 0.2)	(0.5, 0.6)
Flow BG (%)	35	4	4	22
Event mixing (%)	22	2	1	40
UE estimation (%)	1	5	2	25
Total uncertainty (%)	41	7	5	52

Table 8: Systematic uncertainties of out-of-plane correlation function in various $\Delta\varphi$ bins. $p_{\mathrm{T,jet}} > 20(\mathrm{GeV}/c)$, $p_{\mathrm{T}}^{\mathrm{assoc}}$ =2-4(GeV/c).

$\Delta\eta$	(-0.7, -0.6)	(-0.3, -0.2)	(0.1, 0.2)	(0.5, 0.6)
Event mixing (%)	10	4	2	9
UE estimation (%)	4	6	1	5
Total uncertainty (%)	11	7	2	10

Table 9: Systematic uncertainties of in-plane correlation function in various $\Delta\eta$ bins. $p_{\mathrm{T,jet}} > 20(\mathrm{GeV}/c)$, $p_{\mathrm{T}}^{\mathrm{assoc}}$ =0.7-2(GeV/c).

$\Delta\eta$	(-0.7, -0.6)	(-0.3, -0.2)	(0.1, 0.2)	(0.5, 0.6)
Event mixing (%)	17	3	1	7
UE estimation (%)	13	1	1	1
Total uncertainty (%)	21	3	1	7

Table 10: Systematic uncertainties of out-of-plane correlation function in various $\Delta\eta$ bins. $p_{\mathrm{T,jet}} > 20(\mathrm{GeV}/c)$, $p_{\mathrm{T}}^{\mathrm{assoc}}$ =0.7-2(GeV/c).

$\Delta\eta$	(-0.7, -0.6)	(-0.3, -0.2)	(0.1, 0.2)	(0.5, 0.6)
Event mixing (%)	9	1	1	8
UE estimation (%)	9	4	1	5
Total uncertainty (%)	13	4	1	9

Table 11: Systematic uncertainties of in-plane correlation function in various $\Delta\eta$ bins. $p_{\mathrm{T,jet}} > 20(\mathrm{GeV}/c)$, $p_{\mathrm{T}}^{\mathrm{assoc}}$ =2-4(GeV/c).

$\Delta\eta$	(-0.7, -0.6)	(-0.3, -0.2)	(0.1, 0.2)	(0.5, 0.6)
Event mixing (%)	28	1	1	13
UE estimation (%)	24	1	2	3
Total uncertainty (%)	37	1	2	13

Table 12: Systematic uncertainties of out-of-plane correlation function in various $\Delta\eta$ bins. $p_{\mathrm{T,jet}} > 20(\mathrm{GeV}/c)$, $p_{\mathrm{T}}^{\mathrm{assoc}}$ =2-4(GeV/c).

Chapter 6 Results and Discussions

6.1 Charged jets in pp collisions

In this section, the experimental results of charged jet inclusive production cross section measurement in pp collisions at $\sqrt{s} = 5.02$ TeV are shown. The results are compared with model predictions based on LO and NLO pQCD calculations.

6.1.1 Charged jet inclusive differential cross section

The inclusive charged jet production cross sections in pp collisions are shown in Fig. 100 and Fig. 101. Jets are reconstructed using the anti-k_{T} algorithm and the cross sections are obtained for jet resolution parameters $R = 0.2$, 0.3, 0.4, and 0.6. The pseudorapidity range is limited to $|\eta_{\mathrm{jet}}| < 0.9 - R$. The underlying event is not subtracted for the results presented in Fig. 100 while it is in Fig. 101. The measured kinematic region is $5 < p_{\mathrm{T,jet}}^{ch} < 100$ GeV/c and spans from 5×10^{-7} to 2×10^{-1} mb $(\mathrm{GeV}/c)^{-1}$ following a power law.

The measured charged jet production cross sections are compared with several pQCD predictions. PYTHIA is a Monte Carlo (MC) event generator based on the pQCD calculation of $2 \rightarrow 2$ Leading-Order (LO) parton-level hard scattering processes. PYTHIA also includes parton shower and hadronization into final-state particles based on the Lund model [76]. The results are compared with PYTHIA6 and PYTHIA8 for several tunes to account for non perturbative effects. The PYTHIA6 Perugia 2011 tune [77] is based on the pp results from LHC at $\sqrt{s} = 0.9$ and 7 TeV. The PYTHIA8 Monash 2013 tune [78] is based on the pp results at $\sqrt{s} = 8$ and 13 TeV. The PYTHIA8 A14 [79] and the CUETP8M1 [80] tunes are derived from the Monash 2013 tune which were extracted from the underlying event measurements performed by ATLAS and CMS Collaborations. The PYTHIA6 tunes used in this study employ the CTEQ5L [81] Parton Distribution Function (PDF) and the PYTHIA8 tunes utilize the NNPDF2.3 LO PDF [82].

The POWHEG-BOX framework [83, 84, 85, 86] provides Next-to-Leading-Order (NLO) pQCD calculations of $2 \rightarrow 2$ and $2 \rightarrow 3$ parton interactions at $\mathcal{O}(\alpha_{\mathrm{s}}^3)$. POWHEG provides only a calculation of initial parton interactions. Therefore, some shower MC is added to simulate the entire event evolution and obtain the final-state information. In this study, the outgoing partons generated by POWHEG are used as input of PYTHIA8 with A14 tune to simulate the parton shower and the hadronization. The CT14nlo PDF set [87] is utilized for the calculation of initial parton interactions by POWHEG. The default values

of the renormalization scale μ_R and factorization scale μ_F at which the born-level matrix elements are evaluated are chosen to be $\mu_R = \mu_F = p_{\mathrm{T}}$.

Fig. 102, 103 show the comparison between the data and PYTHIA predictions. Fig. 104, 105 show the comparison between the data and POWHEG+PYTHIA8 predictions. The underlying event is evaluated with the perpendicular cone method and subtracted from both the data and MC results are shown in Fig. 103 and Fig. 105. The ratios of the MC predictions to the measured results are shown in bottom panels.

PYTHIA6 Perugia 2011 tune and PYTHIA8 Monash 2018 tune show the maximal (about 25%) difference between data and MC. Predictions from the UE tunes, A14 and CUETP8M1, show better agreement. PYTHIA8 gives a better description of the overall spectra shape than PYTHIA6. At LO accuracy, the measurements are only qualitatively described by the theoretical predictions which failed to reproduce the jet spectrum over the entire measured transverse momentum range.

POWHEG+PYTHIA8, NLO pQCD-based predictions, give good agreement at the 10% level over the widen kinematic phase space (from $p_{\mathrm{T}} > 10$ GeV/c). However, the POWHEG+PYTHIA8 predictions disagree with the data at the low transverse momentum though the theoretical uncertainties are large. In general, non-perturbative processes, such as Multi-Parton Interaction (MPI) and Fragmentation, play a role in this low transverse momentum region ($p_{\mathrm{T}} < 10$ GeV/c). Next-to-Next-to-Leading Order (NNLO) calculations [88] are less sensitive to scale factors (μ_R, μ_F), which is the source of the largest systematic uncertainties for the current NLO calculation. None of current models can precisely describe the UE [89]. So that further studies of the UE are also crucial to understand the jet cross section behavior in the low transverse momentum region.

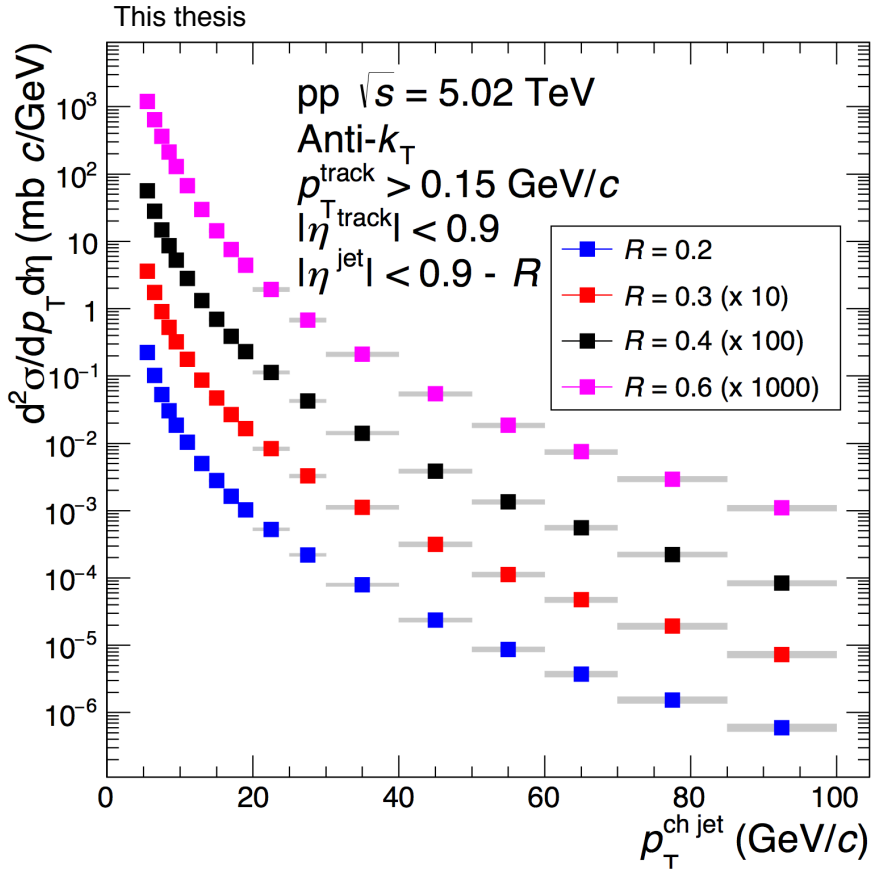

Figure 100: Charged jet differential cross sections in pp collisions at $\sqrt{s} = 5.02$ TeV. Statistical uncertainties are smaller than the marker size. UE is not subtracted. The systematic uncertainties are shown as shaded bands around the data points. Data are scaled by different factors to enhance visibility.

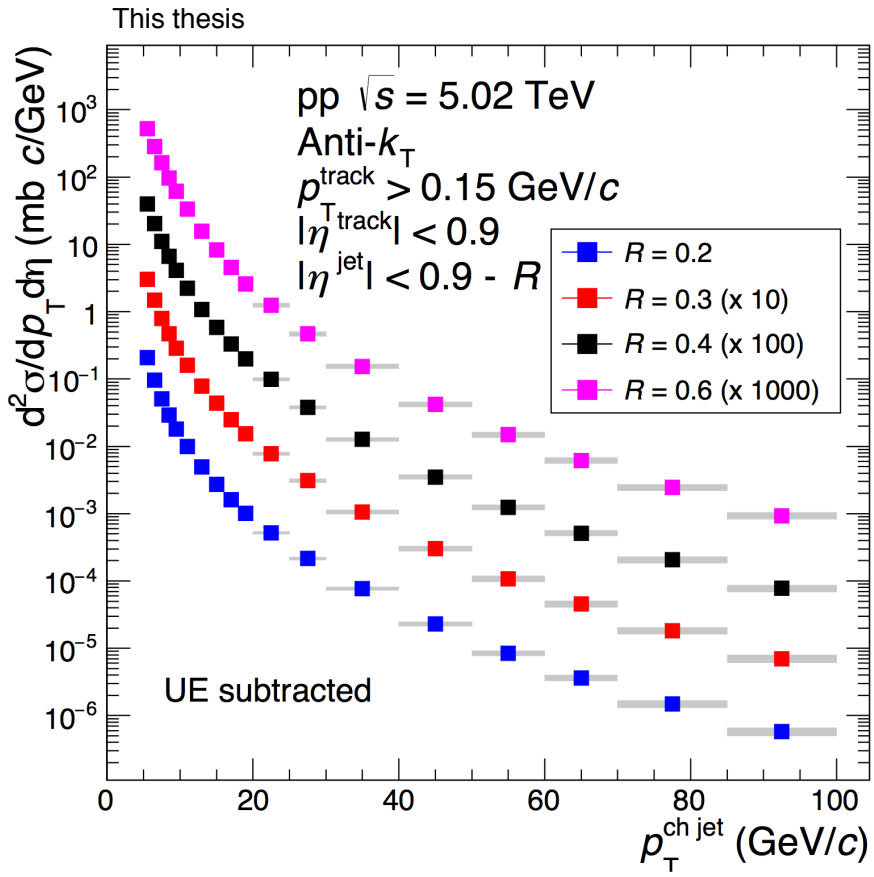

Figure 101: Charged jet differential cross sections with UE subtraction in pp collisions at $\sqrt{s} = 5.02$ TeV. Statistical uncertainties are smaller than the marker size. The systematic uncertainties are shown as shaded bands around the data points. Data are scaled by different factors to enhance visibility.

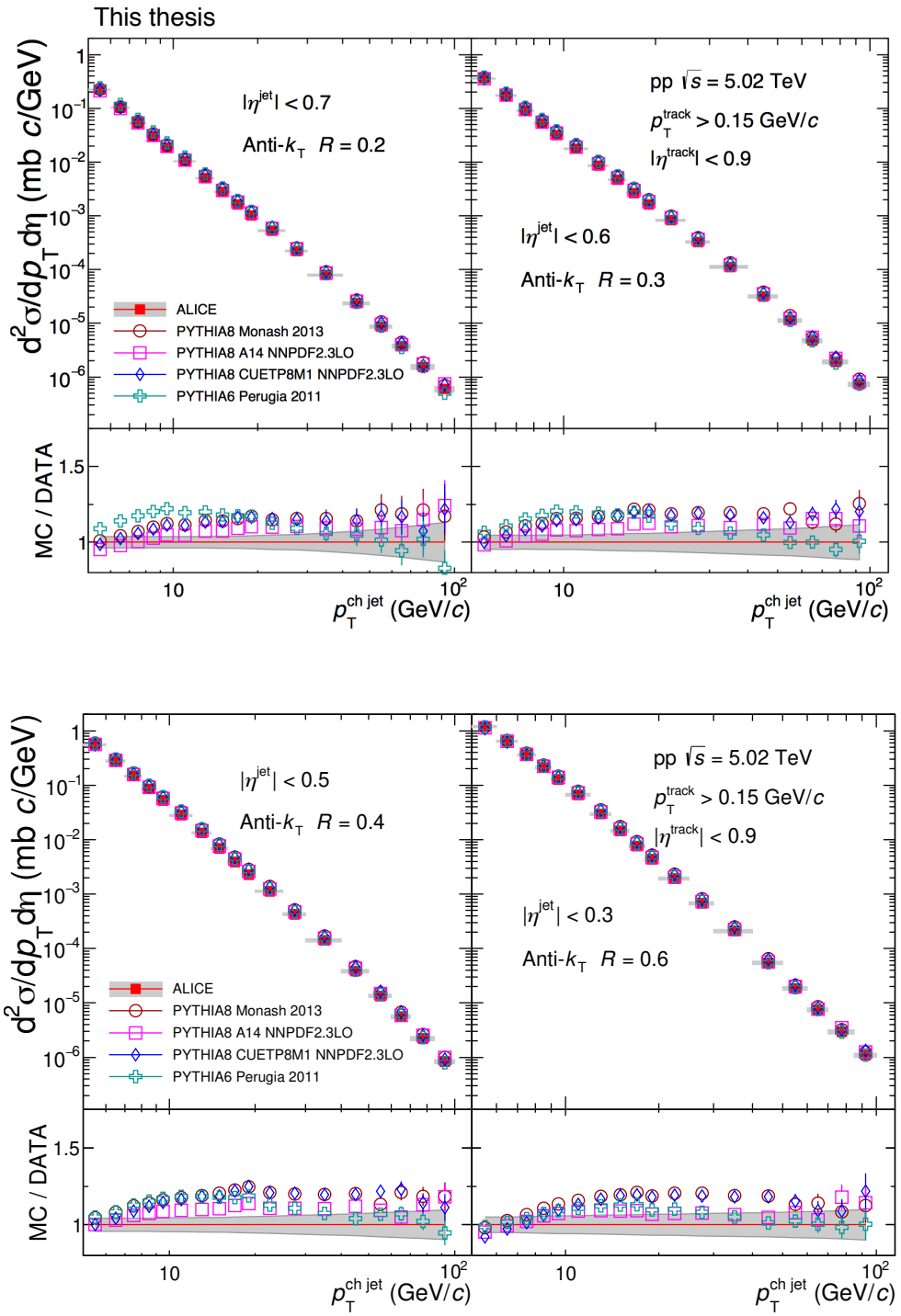

Figure 102: Comparison of the charged jet cross section to LO pQCD MC predictions with different jet resolution parameters $R = 0.2$, 0.3, 0.4, and 0.6. UE is not subtracted. Statistical uncertainties are displayed as vertical error bars. The systematic uncertainty on the data is indicated by a shaded band drawn around unity. The red lines in the ratio correspond to unity.

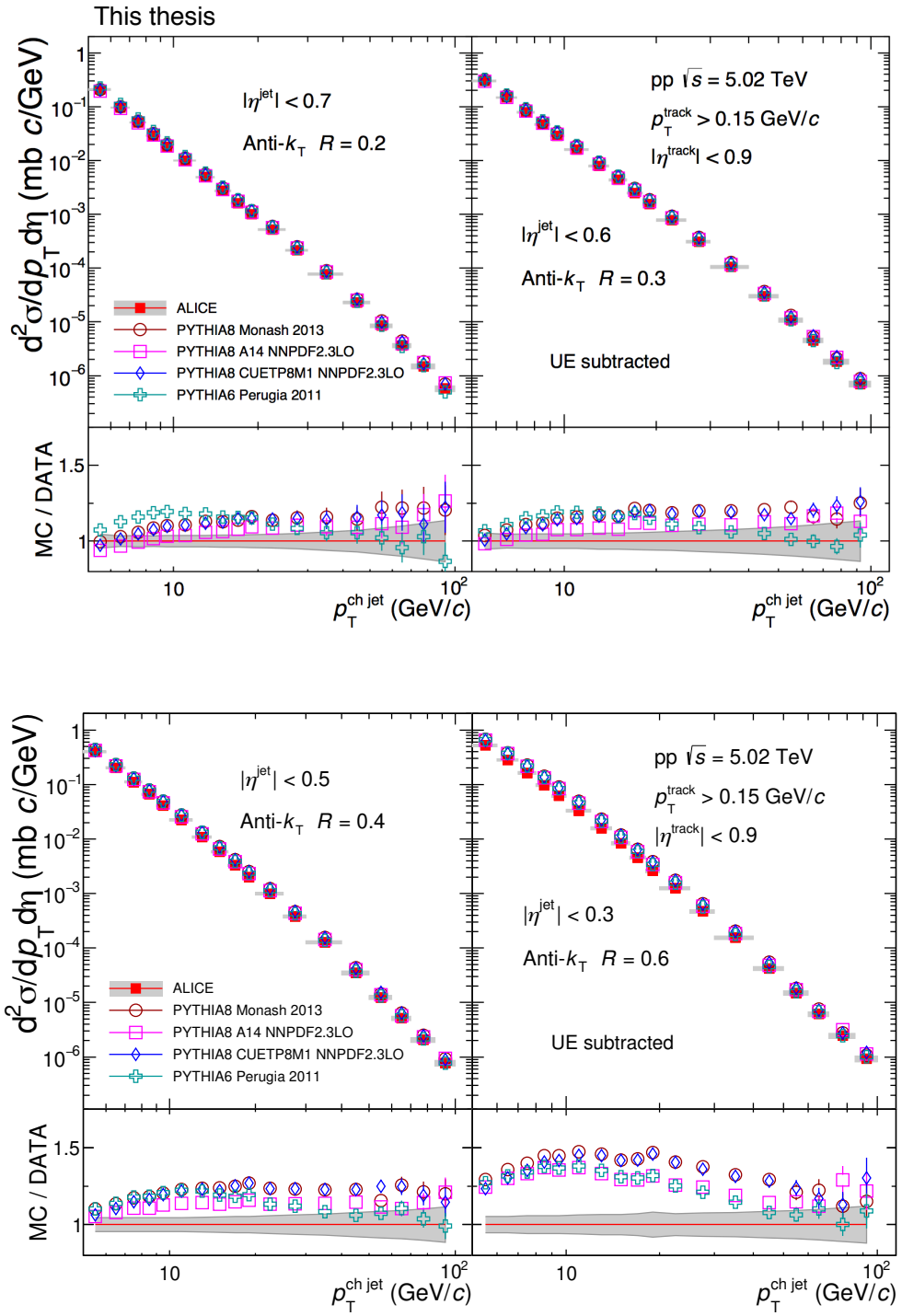

Figure 103: Comparison of the charged jet cross section to LO pQCD MC predictions. UE subtraction is applied. Statistical uncertainties are displayed as vertical error bars. The systematic uncertainty on the data is indicated by a shaded band drawn around unity. The red lines in the ratio correspond to unity.

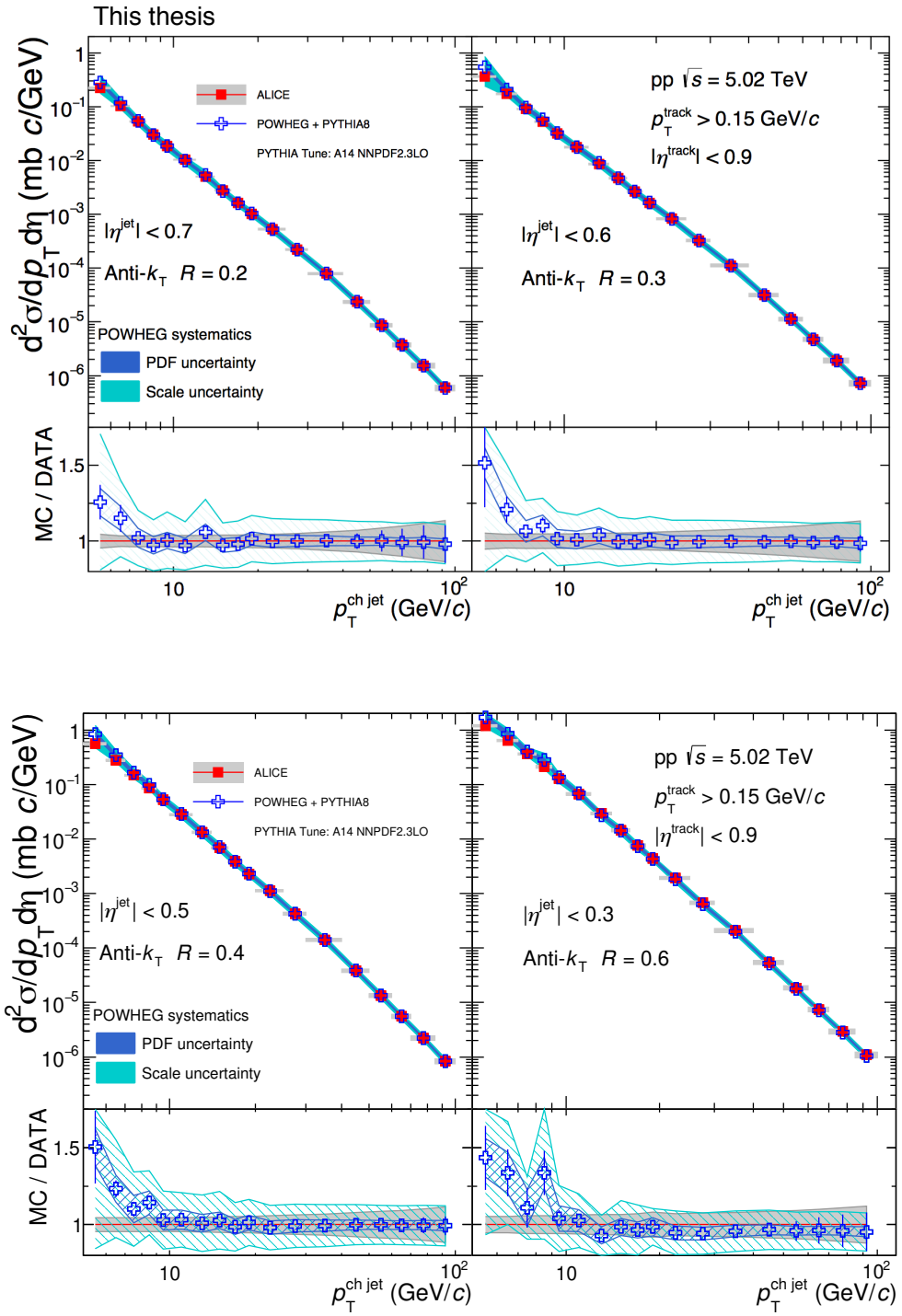

Figure 104: Comparison of the charged jet cross section to NLO pQCD MC predictions (POWHEG+PYTHIA8). UE is not subtracted. Statistical uncertainties are displayed as vertical error bars. The systematic uncertainty on the data is indicated by a shaded band drawn around unity. The red lines in the ratio correspond to unity.

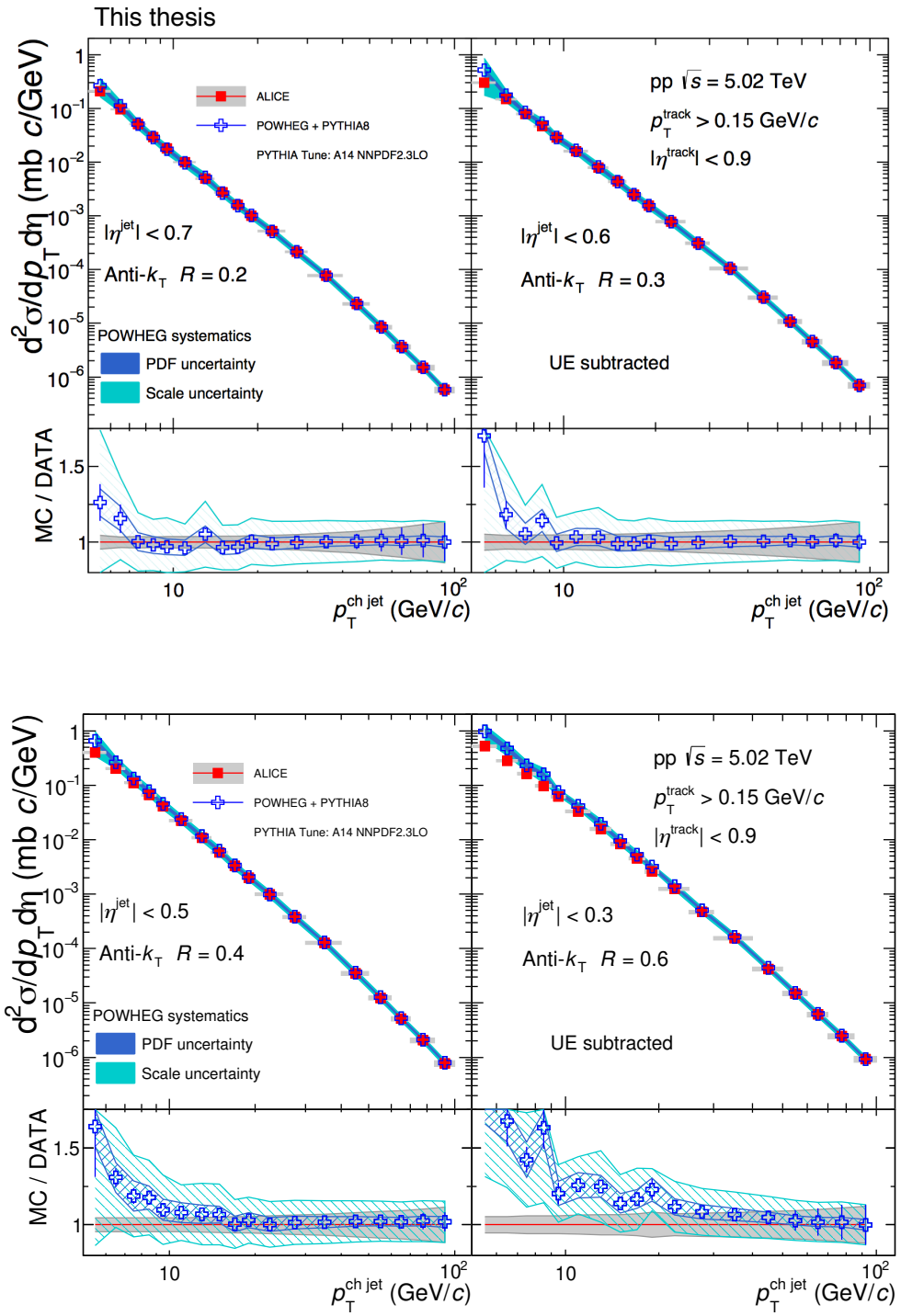

Figure 105: Comparison of the charged jet cross section to NLO pQCD MC prediction (POWHEG+PYTHIA8). UE subtraction is applied. Statistical uncertainties are displayed as vertical error bars. The systematic uncertainty on the data is indicated by a shaded band drawn around unity. The red lines in the ratio correspond to unity.

6.1.2 Charged jet cross section ratio

The charged jet production cross section ratios $R = 0.2$ to $R = 0.4$ and 0.6 for $|\eta_{\rm jet}| < 0.3$ are shown in Fig. 106. Statistical correlations are eliminated by dividing all data sample into two exclusive sub-samples, each of two samples used for respectively estimating the numerator and denominator of the cross section ratio. The ratios are sensitive to the jet radial profiles and provides insights into the interplay between perturbative and non-perturbative effects. The departure of the ratios from unity, due to QCD radiations, decreases with increasing the jet collimation in high transverse momentum range. The measurements are compared with PYTHIA and POWHEG+PYTHIA8 calculations. Both models provide a good description of the ratio within a 10% accuracy. This result suggests the significance of parton shower on this observable besides higher-order matrix element calculations.

The results are compared with those obtained with different collision energies and different collision systems. Fig. 107 (left) shows a comparison with the result in pp collisions at $\sqrt{s} = 7$ TeV and Fig. 107 (right) shows a comparison with the result in p-Pb collisions at $\sqrt{s}_{\rm NN} = 5.02$ TeV. No significant difference is observed. Which could be no collision energy dependence nor cold-nuclear matter effects on for jet radial profiles.

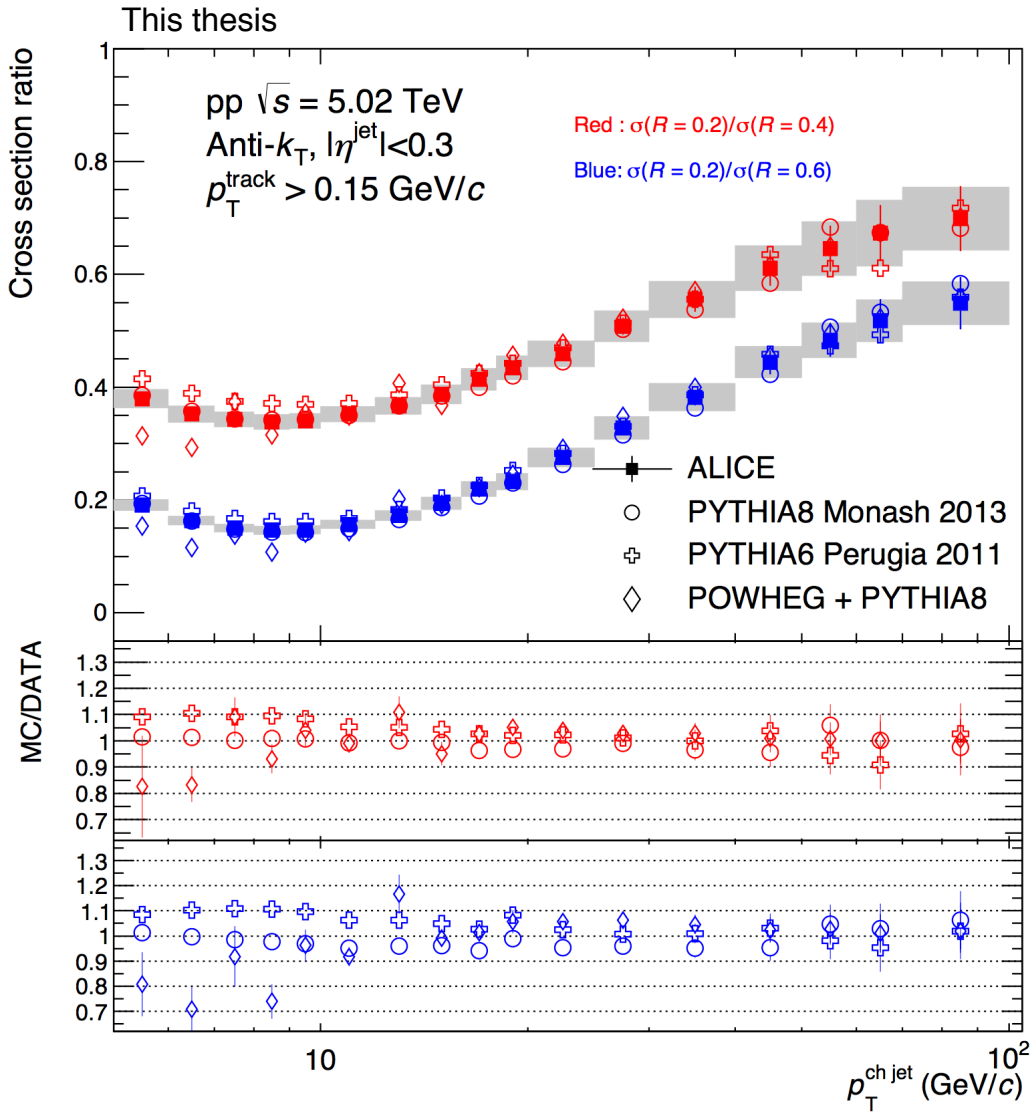

Figure 106: Charged jet cross section ratios for $\sigma(R = 0.2)/\sigma(R = 0.4)$ (Red) and $\sigma(R = 0.2)/\sigma(R = 0.6)$(Blue) in comparison with LO (PYTHIA) and NLO event generators with matched parton showers and modelling of hadronization and the underlying event (POWHEG+PYTHIA8). UE is not subtracted. The systematic uncertainty of the cross section ratio is indicated by a shaded band drawn around data points. No uncertainties are drawn for theoretical predictions for better visibility in upper panel.

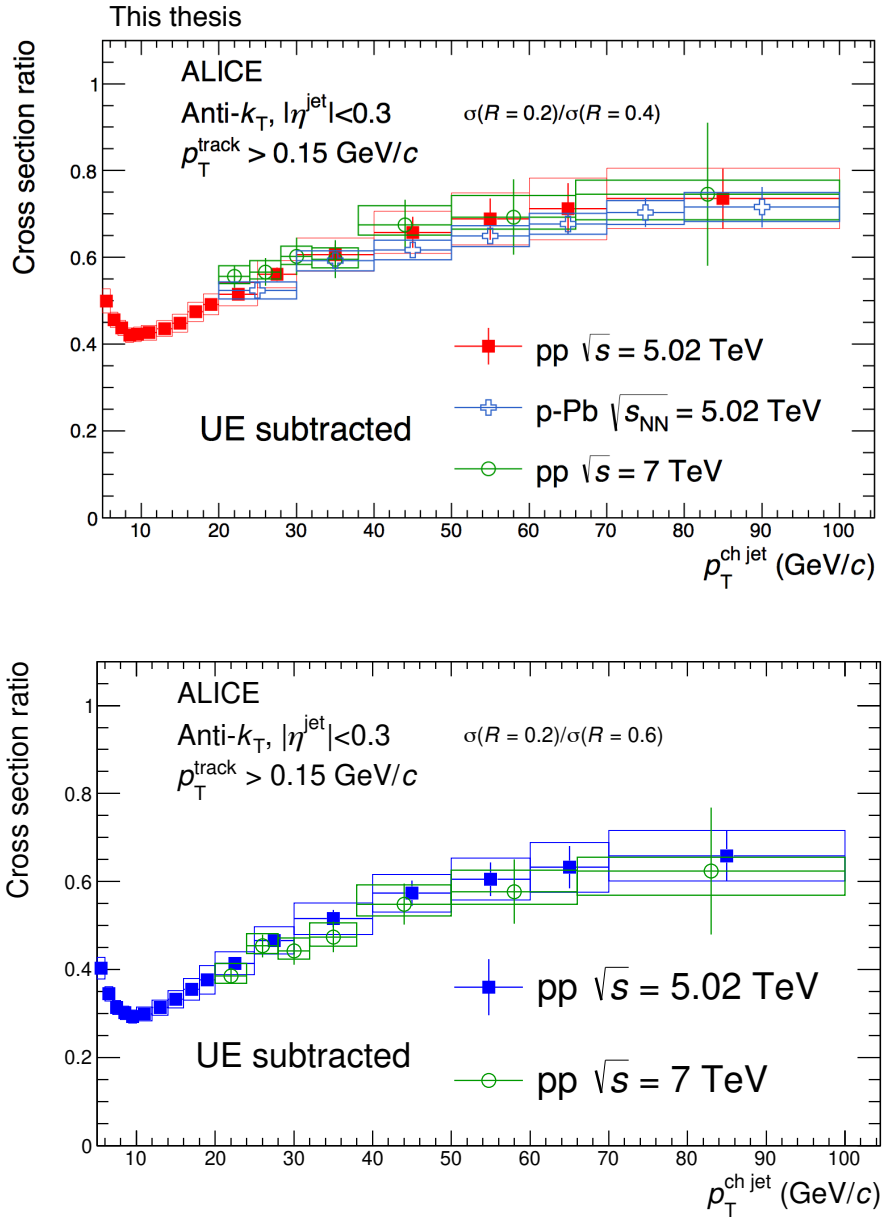

Figure 107: Comparison of the charged jet cross section ratio with UE subtraction to other results. The results in pp collisions at $\sqrt{s} = 5.02$ TeV are compared to the results of pp collisions at $\sqrt{s} = 7$ TeV and p-Pb collisions at $\sqrt{s_{\rm NN}} = 5.02$ TeV.

6.2 Charged jets in Pb-Pb collisions

In this section, the charged jet measurements in mid-central (30-50%) Pb-Pb collisions at $\sqrt{s_{\rm NN}}$ = 5.02 TeV are presented. The charged jets are measured w.r.t 2^{nd} order event plane. Charged jet v_2, which expresses the difference in jet yields in-plane and out-of-plane, is measured to quantitatively assess the parton path-length dependence of the jet suppression. A jet-hadron correlation study is also performed to measure the initial collision geometry dependence of the modification of near-side jet peak shape. The width and mean position of the near-side peaks are measured and compared between in-plane and out-of-plane emissions.

6.2.1 Charged jet v_2 in mid-central Pb-Pb collisions

In non-central ultra relativistic heavy-ion collisions, QGP is formed in the almond-shaped overlap region of the two colliding nuclei. Since the 2^{nd} order event plane is strongly correlated with the initial elliptical shape of the overlap region, the jet v_2, quantifies the variation in parton energy loss for in-plane and out-of-plane jet emissions due to the difference of the in-medium parton path-lengths. The 2^{nd} order anisotropic coefficient v_2 is measured for charged jets as shown in Fig. 108 in mid-central (30-50%) Pb-Pb collisions at $\sqrt{s_{\rm NN}}$ = 5.02 TeV. A positive v_2 value is observed for charged jets, which implies a smaller jet yield out-of-plane than in-plane. This result is consistent with a path-length dependent parton energy loss since partons emitted out-of-plane have a longer in-medium path-length, leading to a stronger energy suppression than in-plane. This result is compared with the charged jet v_2 in Pb-Pb collisions of similar centrality but at $\sqrt{s_{\rm NN}}$ = 2.76 TeV. No significant collision energy dependence is observed as well as other measurements of jet quenching, such as the nuclear modification factor ($R_{\rm AA}$).

A charged jet $R_{\rm AA}$ in Pb-Pb collisions at $\sqrt{s_{\rm NN}}$ = 5.02 TeV is measured as a function of centrality by using the measured charged jet production cross section in pp collisions at the same collision energy. The strength of the jet $p_{\rm T}$-suppression, $\Delta p_{\rm T}$, is estimated as a function of the in-medium parton path-length based on the measured $R_{\rm AA}$ as shown in Fig. 109 [5]. The estimated $\Delta p_{\rm T}$ is fitted by a linear or quadratic function. Both functions gave good description within large uncertainties. Therefore, dominant contribution for in-medium energy loss by collisional energy loss (linear) and radiative energy loss (quadratic) cannot be distinguished in the current uncertainties of the inclusive charged jet $R_{\rm AA}$ measurement.

To further investigate the path-length dependence of jet suppression, a toy MC simulation based on the Glauber model is performed and compared to the measured charged jet

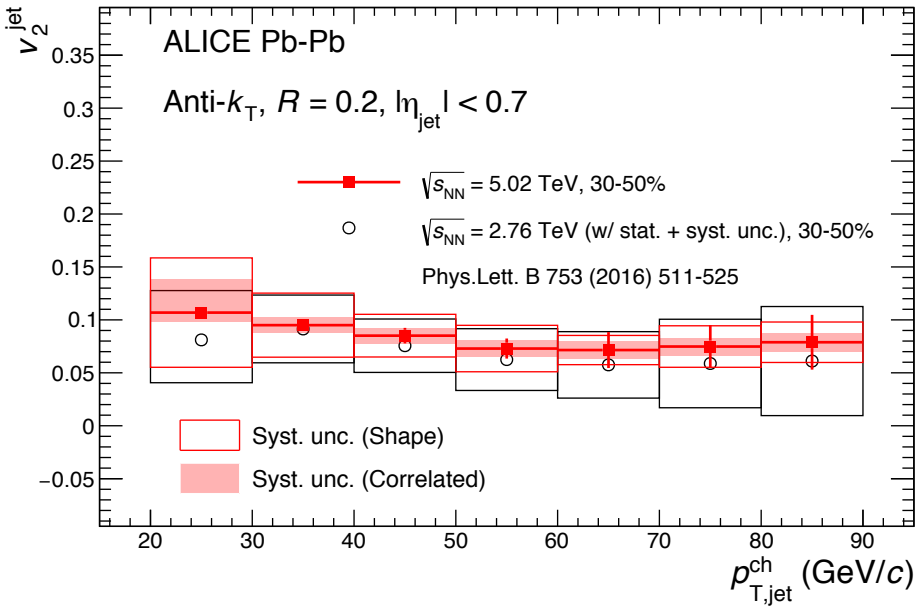

Figure 108: Charged jet v_2 in mid-central (30-50%) Pb-Pb collisions at $\sqrt{s_{\rm NN}}$ = 5.02 TeV (Red). The result is compared to the $v_2^{\rm jet}$ in mid-central (30-50%) Pb-Pb collisions at $\sqrt{s_{\rm NN}}$ = 2.76 TeV (Black) [36]

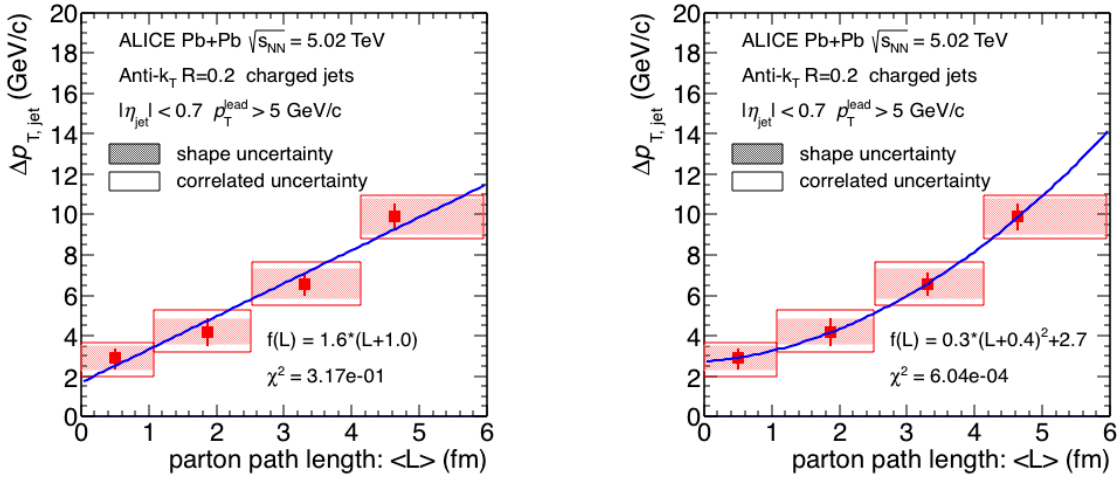

Figure 109: Estimated $R = 0.2$ charged jet $p_{\rm T}$ suppression as a function of in-medium parton path-length L [5]. The result are fit by a linear function (left) or by a quadratic function (right)

v_2. Here, in order to determine the effective overlap region of two colliding nuclei where the medium is created, two definitions are tested:

- def. 1) The overlap region of average nucleus radii of two colliding nuclei. (Fig. 110 left)
  Here the average nucleus radius is $1.2A^{1/3}$ fm, where A is the mass number of the given nucleus.
- def. 2) The elliptical region defined by the distribution of participants which is estimated by Glauber MC simulation (Fig. 110 right). The length of major and minor axes of the elliptical region are defined as 1 σ of the sliced participant distribution in-plane and out-of-plane (projection to x' or y' axis at $y' = 0$ or $x' = 0$).

The def. 1 is the same definition as the one assumed in the study presented in Ref. [5]. The def. 2 is based on the event plane dependent inclusive hadron $R_{\rm AA}$ study shown in Ref. [90]. The parton path-length is calculated as the average length between the point where the nucleon-nucleon collisions occurred and the edge of the effective overlap region. Hereafter, the path-length calculated based on def. 1 and def. 2 expressed as L_{HS} and L_{σ} respectively. The toy model simulation inputs are:

- The measured charged jet production cross section in pp collisions
  The $R = 0.2$ charged jet production cross section measurement in pp collisions shown in Fig. 100 serves as a reference for jet production without medium-induced jet suppression. The spectrum is fit by a double-Tsallis function (Eq.57).
- The estimated $\Delta p_{\rm T}$ based on the $R_{\rm AA}$ measurement in Pb-Pb collisions at $\sqrt{s_{\rm NN}} = 5.02$ TeV
  The estimated $\Delta p_{\rm T}$ for $R = 0.2$ charged jets as a function of $\langle L \rangle^{\alpha}$ or $\rho^{\beta}\langle L \rangle^{\alpha}$ is fit by linear function, where $\langle L \rangle$ is the in-medium parton path-length calculated with the Glauber MC simulation and ρ is the initial energy density. In this study, only $\Delta p_{\rm T}$ in 0-50% centrality collisions (largest three $\langle L \rangle$ points in Fig. 109) are used since the event selection bias leads to a non-negligible non-medium-induced high-$p_{\rm T}$ hadron suppression in peripheral collisions [91]. The initial energy density ρ is calculated in the same way as Ref. [90]:
  $$\rho = K \frac{dN/d\eta}{4\pi L_{\rm in} L_{\rm out}} \tag{59}$$
  where $L_{\rm in}$ and $L_{\rm out}$ are the major and minor axis lengths of the effective overlap region and K is a constant assumed to only weakly depend on centrality and collision energy.

In this study, as well as in Ref. [90], $K = 1$ (GeV/fm) is chosen in such a way as to make ρ expressed units of in GeV/fm^3.

Nucleons inside the nucleus are distributed according to the Woods-saxon potential. The inelastic pp collision cross section $\sigma_{\rm inel}^{pp} = 68$ mb is utilized to compute the number of participants. The fit functions to the $R = 0.2$ charged jet production cross section are

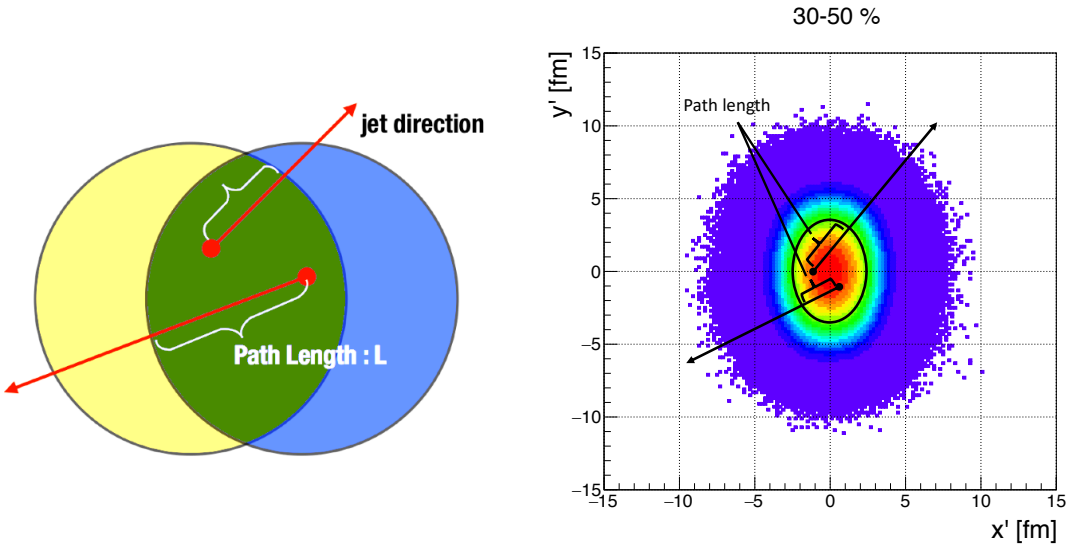

Figure 110: Definitions of the effective overlapping region for in-medium parton path-length calculation with Glauber MC simulation.
Left: The overlapping region of average nucleus radii of two colliding nuclei [5].
Right: The elliptical region defined by participant distribution. The major and minor axes are defined as 1 σ of the slice of participant distribution in-plane and out-of-plane. The x' axis is corresponding to the participant event plane direction.

shifted by the expected $\Delta p_{\rm T}$ in-plane and out-of-plane expected from the linear fit of the $\Delta p_{\rm T}$ as a function of $\langle L \rangle^{\alpha}$ or $\rho^{\beta}\langle L \rangle^{\alpha}$. The jet v_2 as a function of $p_{\rm T}$ is estimated based on the set of shifted functions derived from the parameter space scanning of α and β. The jet v_2 χ^2 is calculated with the measured charged jet $v_2^{\rm data}$ and the estimated $v_2^{\rm MC}$ by MC simulation as:

$$\chi^2 = \sum \frac{\left(v_2^{\rm data} - v_2^{\rm MC}\right)^2}{\sigma_{stat.}^2 + \sigma_{syst.}^2} \tag{60}$$

where $\sigma_{stat.}$ and $\sigma_{syst.}$ are the quadratic sum of the statistical and systematic uncertainties respectively. The reduced chi-square (χ^2/ndf) is calculated by dividing the χ^2 by the number of data points. Fig. 111 shows the calculated reduced chi-square for the jet v_2 (red) and for a linear fit of the $\Delta p_{\rm T}$ (blue) as a function of path-length exponent. The results suggest that

the jet v_2 measurement is more sensitive to the path-length than the $R_{\rm AA}$ measurement as a function of centrality, because the distribution of the jet v_2 reduced chi-square is narrower than that of the $\Delta p_{\rm T}$. Although the optimal path-length exponent differs from jet j_2 to $\Delta_{p_{\rm T}}$, it is eventually not constrained by both def. 1,2 due to large uncertainties. In the Ref. [90],

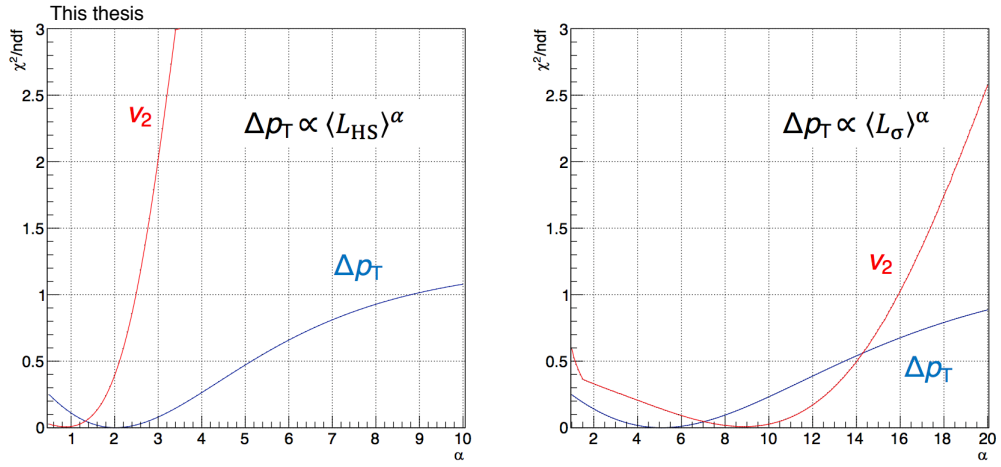

Figure 111: The reduced chi-square for jet v_2 (red) and $\Delta p_{\rm T}$ linear fit (blue).
Left: The reduced chi-square as a function of the $\langle L_{\rm HS}\rangle$ exponent (α).
Right: The reduced chi-square as a function of the $\langle L_{\sigma}\rangle$ exponent (α).

it was reported that the inclusive hadron $R_{\rm AA}$ in-plane and out-of-plane scale when taking into account the centrality dependent energy initial density ρ. Fig. 112 shows the reduced chi-square for $\Delta p_{\rm T}$ linear fit (left) and jet v_2 (right) as a function of the path-length and ρ exponents (α, β) within def. 2. $\alpha = 2.6$ and $\beta = 1.1$ result in the best description of both jet v_2 and $\Delta p_{\rm T}$ simultaneously. In the Ref. [90], two scenarios of $\Delta p_{\rm T} \propto \sqrt{\rho} L$ and $\Delta p_{\rm T} \propto \rho^{3/4} L^2$ were proposed based on radiative energy loss calculation. This result is close to the $\Delta p_{\rm T} \propto \rho^{3/4} L^2$ case. However, $\Delta p_{\rm T} \propto \sqrt{\rho} L$ is not ruled out due to the large uncertainties. The in-medium energy loss scenario will be constrained by reducing the uncertainties. This scaling with ρ turns out to be not effective within def. 1 case, because, unlike the def. 2 case, ρ being almost constant over the 0-50% centrality interval class.

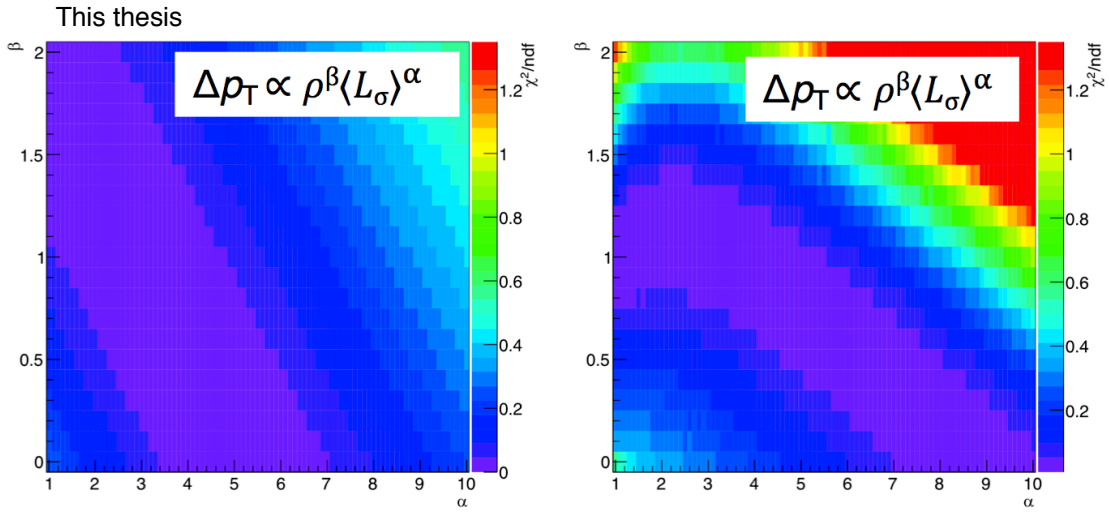

Figure 112: The reduced chi-square as a function of the exponent of $\langle L_\sigma \rangle$ (α) and of ρ (β) for Δp_{T} (derived from R=0.2 jet R_{AA}) fit (left) and for jet v_2 (right).

6.2.2 Charged jet-hadron correlations in mid-central Pb-Pb collisions

In order to explore the jet modification dependence on initial collision geometry, jet-hadron correlations are studied w.r.t the 2^{nd}-order event plane. In this study, background subtracted near-side jet peaks are fit by a Lorentzian function, which is also known a the 'Cauchy distribution'. Fig. 113 and Fig. 114 show the near-side peaks observed for in-plane ($|\Delta\phi(\phi_{\mathrm{jet}-\psi_2})| < \pi/4$)) and out-of-plane ($|\Delta\phi(\phi_{\mathrm{jet}-\psi_2})| > 3\pi/8$)) jet emission correlated with low ($0.7 < p^{assoc}_{\mathrm{T,track}} < 2$ GeV/c) and high ($2 < p^{assoc}_{\mathrm{T,track}} < 4$ GeV/c) p_{T} associated tracks respectively. Left (Right) figures are projections of $C(\Delta\varphi, \Delta\eta)$ on $\Delta\phi$ ($\Delta\eta$) axis.

$\Delta\phi$ distributions of low-p_{T} associated tracks show a broadening of the near-side peak width from in-plane to out-of-plane jet emission. The out-of-plane width increases by about 10-20% in $\Delta\phi$. $\Delta\eta$ distribution of near-side peak also shows the broadening for low-p_{T} associated tracks by about 1-10%. However, it is not so significant within the uncertainties. on the other hand, no difference between in-plane and out-of-plane is observed for high-p_{T} associated tracks. As reported by the CMS Collaboration, for low-p_{T} associates, the jet radial profile broadens in the most central Pb-Pb collisions Fig. 22. This suggests that the jet radial profile broadens as in-medium parton path lengthens. This finding is consistent with the results obtained in the present study. Furthermore, the radial profile for the high-p_{T} associates is not modified for the most central collisions according to the CMS results. This observation is again consistent with the results hereinbefore shown. Reflecting on these

results, the observed phenomenon could be interpreted as due to:

- In-medium parton shower evolution different from the vacuum one.
- Energy re-distribution in a medium with hydrodynamical evolution
  The modification of the jet radial profile reported by the CMS Collaboration is described by a model including hydrodynamical effects as shown in Fig. 23. The results shown in this thesis may also be described by a similar model.

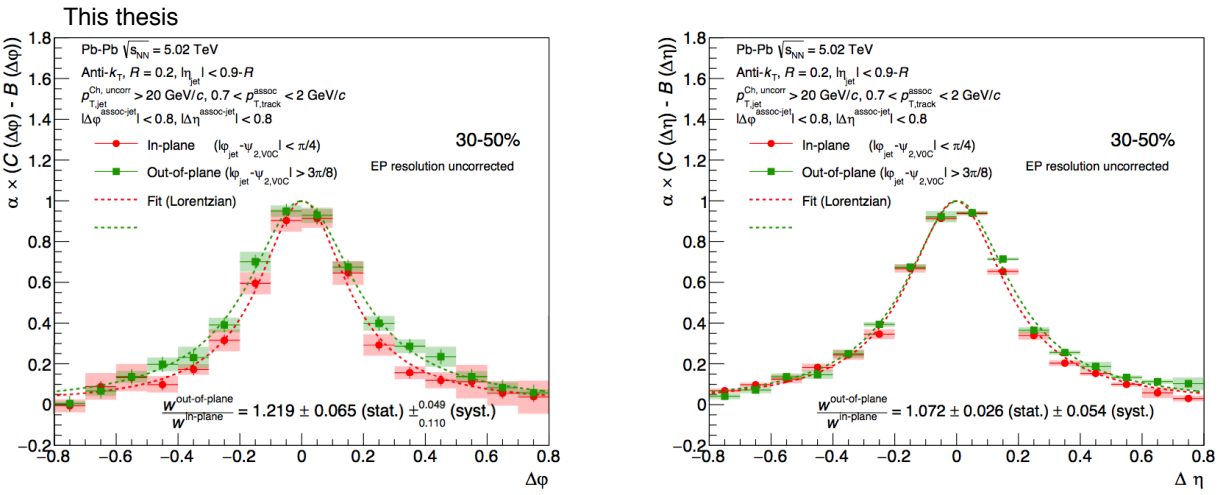

Figure 113: Near-side jet-hadron correlations for in-plane jets ($|\Delta\phi(\phi_{\mathrm{jet}-\psi_2})| < \pi/4$), Red) and out-of-plane jets ($|\Delta\phi(\phi_{\mathrm{jet}-\psi_2})| > 3\pi/8$), Green). $p_{\mathrm{T,jet}}^{\mathrm{ch,\ det}} > 20$ GeV/c. $0.7 < p_{\mathrm{T,track}}^{assoc} < 2$ GeV/c. α is selected as the fit function height to be 1.

Fig. 115 shows the near-side azimuthal peak position w.r.t jet axis. The peak position is shifted towards the in-plane direction and this effect is stronger for low-p_{T} associates. The medium thickness and pressure gradient will be asymmetric w.r.t the jet axis, especially in mid-central collisions. These features may be able to describe this azimuthal asymmetry w.r.t the jet axis due to the initial elliptical collision geometry. In order to quantify the amplitude of the shift effect w.r.t the event plane, Fig. 115 is fit by a sine function:

$$f(x) = M \cdot \mathrm{Sin}(2x) \tag{61}$$

where M is a free parameter which express the amplitude of the sine curve.

A MC simulation by JEWEL [37], which incorporates in-medium parton energy loss and parton shower evolution, is performed in order to compare our experimental results to theoretical predictions. The lost energy re-distribution and hydrodynamical medium

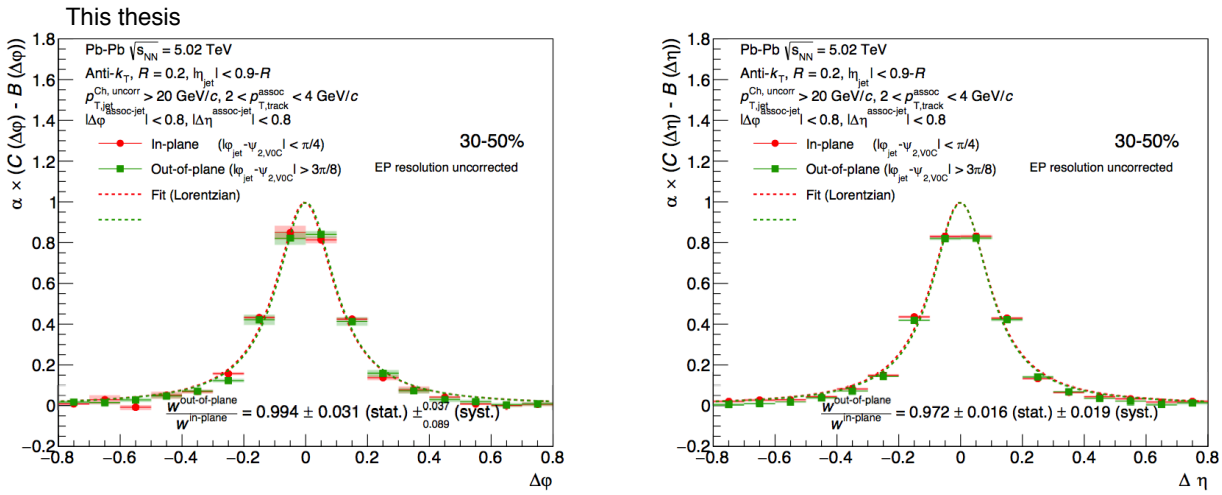

Figure 114: Near-side jet-hadron correlations for in-plane jets ($|\Delta\phi(\phi_{\mathrm{jet}-\psi_2})| < \pi/4$)) and out-of-plane jets ($|\Delta\phi(\phi_{\mathrm{jet}-\psi_2})| > 3\pi/8$), Green). $p_{\mathrm{T,jet}}^{\mathrm{ch,\ det}} > 20$ GeV/c, $2 < p_{\mathrm{T,track}}^{assoc} < 4$ GeV/c. α is selected as the fit function height to be 1.

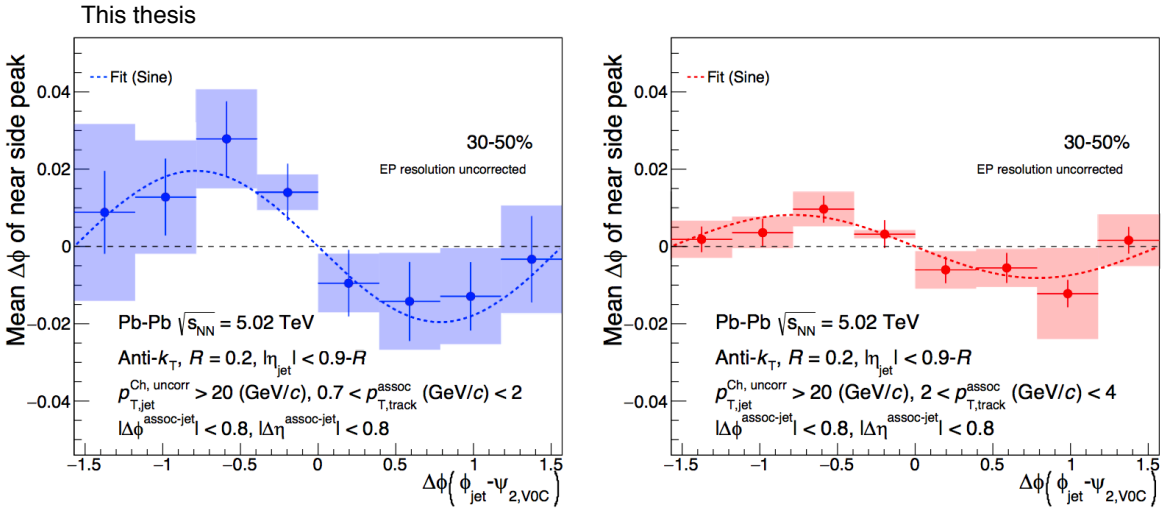

Figure 115: The near-side peak position w.r.t jet axis in azimuth as a function of angle between jet axis and event plane. $p_{T,jet}^{\mathrm{ch,\ det}} > 20$GeV/$c$. Left: $0.7 < p_{\mathrm{T,track}}^{assoc} < 2$ GeV/c, Right: $2 < p_{\mathrm{T,track}}^{assoc} < 4$ GeV/c

response are nevertheless included in this simulation. The generated particles by JEWEL are reduced/smeared according to the tracking efficiency (Fig. 36) and resolution (Fig. 37) since all the observables in this jet-hadron correlation work are not corrected for detector effects. The charged jets in the MC simulation are reconstructed by anti-k_{T} algorithm as well as the data analysis. The reconstructed charged jet p_{T} is also smeared according to the measured δp_{T} (Fig. 74) in order to adjust the jet energy scale between data and MC simulation. After the jet p_{T} smearing, jet-hadron correlations are measured for $p_{T,jet}^{\mathrm{ch,\ det}} > 20\mathrm{GeV}/c$, $0.7 < p_{\mathrm{T,track}}^{assoc} < 2$ GeV/c and $2 < p_{\mathrm{T,track}}^{assoc} < 4$ GeV/c.

p_{T}^{assoc} (GeV/c)	$0.7 < p_{\mathrm{T,track}}^{assoc} < 2$	$2 < p_{\mathrm{T,track}}^{assoc} < 4$
Data	1.22 ± 0.07 (stat.) $\pm^{0.05}_{0.11}$ (syst.)	1.00 ± 0.03 (stat.) $\pm^{0.04}_{0.09}$ (syst.)
JEWEL	1.02 ± 0.02 (stat.)	1.00 ± 0.03 (stat.)

Table 13: The ratio of near-side jet peak width in azimuth ($\Delta\varphi$) out-of-plane over the one of in-plane. The results from data are compared to JEWEL predictions.
$p_{T,jet}^{\mathrm{ch,\ det}} > 20\mathrm{GeV}/c$, $0.7 < p_{\mathrm{T,track}}^{assoc} < 2$ GeV/c and $2 < p_{\mathrm{T,track}}^{assoc} < 4$ GeV/c

p_{T}^{assoc} (GeV/c)	$0.7 < p_{\mathrm{T,track}}^{assoc} < 2$	$2 < p_{\mathrm{T,track}}^{assoc} < 4$
Data	1.07 ± 0.03 (stat.) $\pm$ 0.05 (syst.)	0.97 ± 0.02 (stat.) $\pm$ 0.02 (syst.)
JEWEL	0.98 ± 0.02 (stat.)	0.97 ± 0.02 (stat.)

Table 14: The ratio of near-side jet peak width in eta ($\Delta\eta$) out-of-plane over the one of in-plane. The results from data are compared to JEWEL predictions.
$p_{T,jet}^{\mathrm{ch,\ det}} > 20\mathrm{GeV}/c$, $0.7 < p_{\mathrm{T,track}}^{assoc} < 2$ GeV/c and $2 < p_{\mathrm{T,track}}^{assoc} < 4$ GeV/c

Tab. 13 and 14 show the ratio of near-side peak width out-of-plane over the one of in-plane in 30-50% Pb-Pb collisions at $\sqrt{s_{\mathrm{NN}}} = 5.02$ TeV (Data). The former table is for the peak in azimuth and the latter one is for the peak in eta. The peak width is estimated by fitting with Lorentzian function. The data results are compared to the JEWEL predictions. The broadening effect observed in the data result for low-p_{T} associates is not observed in the JEWEL prediction within uncertainty.

p_{T}^{assoc} (GeV/c)	$0.7 < p_{\mathrm{T,track}}^{assoc} < 2$	$2 < p_{\mathrm{T,track}}^{assoc} < 4$
Data	-0.02 $\pm$ 0.005 (stat.) $\pm$ 0.006 (syst.)	-0.008 $\pm$ 0.002 (stat.) $\pm$ 0.002 (syst.)
JEWEL	-0.004 $\pm$ 0.002 (stat.)	0.0006 $\pm$ 0.0007 (stat.)

Table 15: The amplitudes of sine function (Eq. 61) obtained by the fitting to the peak position in azimuth as a function of the angle between trigger jet axis and event plane. The results from data are compared to JEWEL predictions.
$p_{T,jet}^{\mathrm{ch,\ det}} > 20\mathrm{GeV}/c$, $0.7 < p_{\mathrm{T,track}}^{assoc} < 2$ GeV/c and $2 < p_{\mathrm{T,track}}^{assoc} < 4$ GeV/c

Tab. 15 shows the amplitudes of sine function (Eq. 61) obtained by fitting of near-side peak positions in azimuth ($\Delta\varphi$). Similar effect is observed in JEWEL prediction for low-p_{T} associates though it is tiny effect in comparison with the one of data. No peak position shift is observed for high-p_{T} associates in JEWEL prediction.

The results in Tab. 13, 14, and 15 suggests that the difference of near-side jet-like peak modification in-plane, mid-plane, and out-of-plane cannot be described only by in-medium parton energy loss and parton shower evolution.

Chapter 7 Summary

Jets are well calibrated experimental observables to study QCD effects. Measurements of jets allows to access the initial partons because of the asymptotic freedom property of the QCD and the elementary process of jet production being calculable with pQCD. Jets are also well established probes of QGP which is a hot and dense QCD medium formed in relativistic heavy-ion collisions. Measurements of jets allowed to probe the entire evolution of the medium since jets originate from initial hard-scattered partons which lose energy while traversing the medium. The properties of QGP, such as stopping power, can be assessed by measureing the medium induced energy suppression of jets.

In general, the p_{T} spectrum of jets follows a power-law distribution. Hence, high-p_{T} jet events are rare. Event triggering is a powerful experimental technique to enable the measurement of such rare probes. In this thesis, the trigger system development and its commissioning to the ALICE electromagnetic calorimeters (EMCal, DCal and PHOS), which was performed during LHC LS 1 and the first year of LHC Run2, have been described. The Di-Jet calorimeter, called DCAL, has been installed during LS1 to enhance the jet measurement capability of ALICE. The firmware of the Level-1 online trigger electronics, the Summary Trigger Unit (STU), has been upgraded to adapt it to the new detector configurations of Run2. A new trigger algorithm for heavy-ion collisions, which calculates the background on an event-by-event basis the energy density estimated by the calorimeters opposite side in azimuth, has been implemented. We performed the commissioning tasks and the trigger system was operated stably throughout LHC Run2 (Late 2015-2018). The physics results utilizing the trigger data start to come out. The firmware upgrade and commissioning was done as a cooperative work mainly with H.Yokoyama.

A data analysis with the pp collisions at $\sqrt{s} = 5.02$ TeV and Pb-Pb collisions at $\sqrt{s_{\mathrm{NN}}} = 5.02$ TeV datasets has been performed. Charged jet production cross sections in pp collisions have been measured with jet resolution parameter $R = 0.2$, 0.3, 0.4 and 0.6. The measured cross sections have been compared with LO and NLO pQCD-based model predictions. The data results in kinematic range $10 < p_{\mathrm{T,jet}}^{\mathrm{ch}} < 100\mathrm{GeV}/c$ are well described by pQCD calculation at NLO accuracy. On the other hand, predictions show a large discrepancy from data in lower $p_{\mathrm{T,jet}}$ range while large theoretical uncertainties mainly coming from normalization factors of the pQCD calculation. The systematic uncertainties

could be improved with Next-to-Next-to-Leading Order (NNLO) calculations. It may also be important to understand non-perturbative effects, such as the underlying event, for an improved understanding of the jet production cross section in low $p_{\mathrm{T,jet}}$ range.

The 2^{nd} anisotropic coefficient for charged jets, v_2^{jet} has been measured in mid-central (30-50%) Pb-Pb collisions for R = 0.2 jets. The results have been compared with the v_2^{jet} in mid-central (30-50%) Pb-Pb collisions at $\sqrt{s}_{\mathrm{NN}} = 2.76$ TeV. As a result, no collision energy dependence is found. A toy model MC Glauber simulation has been performed to study in-medium path-length dependent parton energy loss in detail. The estimated strength of jet suppression, $\Delta p_{\mathrm{T,jet}}$, by R_{AA} measurement [5] and measured production cross section of charged jet in pp collisions have been used as inputs of the simulation. The results of toy model MC, especially with $\Delta p_{\mathrm{T,jet}} \propto \rho^{1.1}\langle L_\sigma \rangle^{2.6}$ case, quantitatively describes the v_2^{jet} and R_{AA} in mid-central (30-50%) Pb-Pb collisions at $\sqrt{s}_{\mathrm{NN}} = 5.02$ TeV simultaneously. It basically supports the in-medium radiative energy loss scenario of $\Delta p_{\mathrm{T}} \propto \rho^{3/4} L^2$ which was proposed in Ref. [90]. However, one another scenario, $\Delta p_{\mathrm{T}} \propto \sqrt{\rho} L$, is not ruled out due to the large uncertainties. There are possibly available dataset of Pb-Pb collisions at $\sqrt{s}_{\mathrm{NN}}$ = 5.02 TeV taken in 2018 and further experiment will be performed in future at the LHC Run3 (see also below). The statistical uncertainties will be reduced by analyzing these new data. One of the largest systematic uncertainties comes from underlying event fluctuation. Recently, it was proposed that the underlying event fluctuation effect may be able to reduce by machine learning technique [92]. The in-medium energy loss scenario will be constrained by reducing the uncertainties on both v_2^{jet} and R_{AA} in further studies.

Jet-hadron correlations for $p_{\mathrm{T,jet}}^{\mathrm{det}} > 20$ GeV/c have been studied w.r.t 2^{nd} order event plane. The correlations has been studied in $0.7 < p_{\mathrm{T,track}}^{\mathrm{assoc}} < 2$ GeV/c and $2 < p_{\mathrm{T,track}}^{\mathrm{assoc}} <$ 4 GeV/c. Broader distribution of the near-side jet peak in out-of-plane jet emission in comparison with in-plane jet emission is observed for low-p_{T} associates. A near-side peak position shift in azimuth towards in-plane direction have also been observed for both p_{T} range. The measured results have been compared to theoretical prediction by JEWEL. The prediction doesn't reproduce the measured results except that the peak position shift for low-p_{T} associates are partially reproduced. It suggests that the near-side peak shape modification w.r.t 2^{nd}-order event plane cannot be described only by the in-medium parton energy loss and parton shower evolution. Therefore, the medium-induced near-side jet modification may be understood as a combination of in-medium radiation, initial geometry dependent energy suppression and medium response with hydrodynamical evolution.

As shown in this thesis and other studies, charged jet measurements with ALICE detector have been well established. In future, full jet (charged+neutral) measurements with

calorimeters using the triggered data will enhance the physics capabilities of the jet measurements. For example, full jet measurement with EMCal+DCal allows di-jet measurement with high energy resolution in comparison with measurements of charged jets. Another remarkable challenging project at the ALICE is that the high-rate continuous data readout with online track reconstruction in Run3 [93, 94]. It will also allow measurement of rare probes with high statistical precision.

Appendix A A Large Ion Collider Experiment

A Large Ion Collider Experiment (ALICE) is one of the major experiments at LHC. The main physics program of ALICE aims at revealing the properties of hot and dense nuclear matter, i.e QGP. As of 2018, about 1800 members from 177 institutes in 41 countries are participating with the ALICE collaboration [56].

Figure 116: The world map on the earth. The countries collaborating with ALICE are colored in red [56].

Appendix B Quality Assurance for pp collisions

Track QA study was performed for datasets of pp collisions.

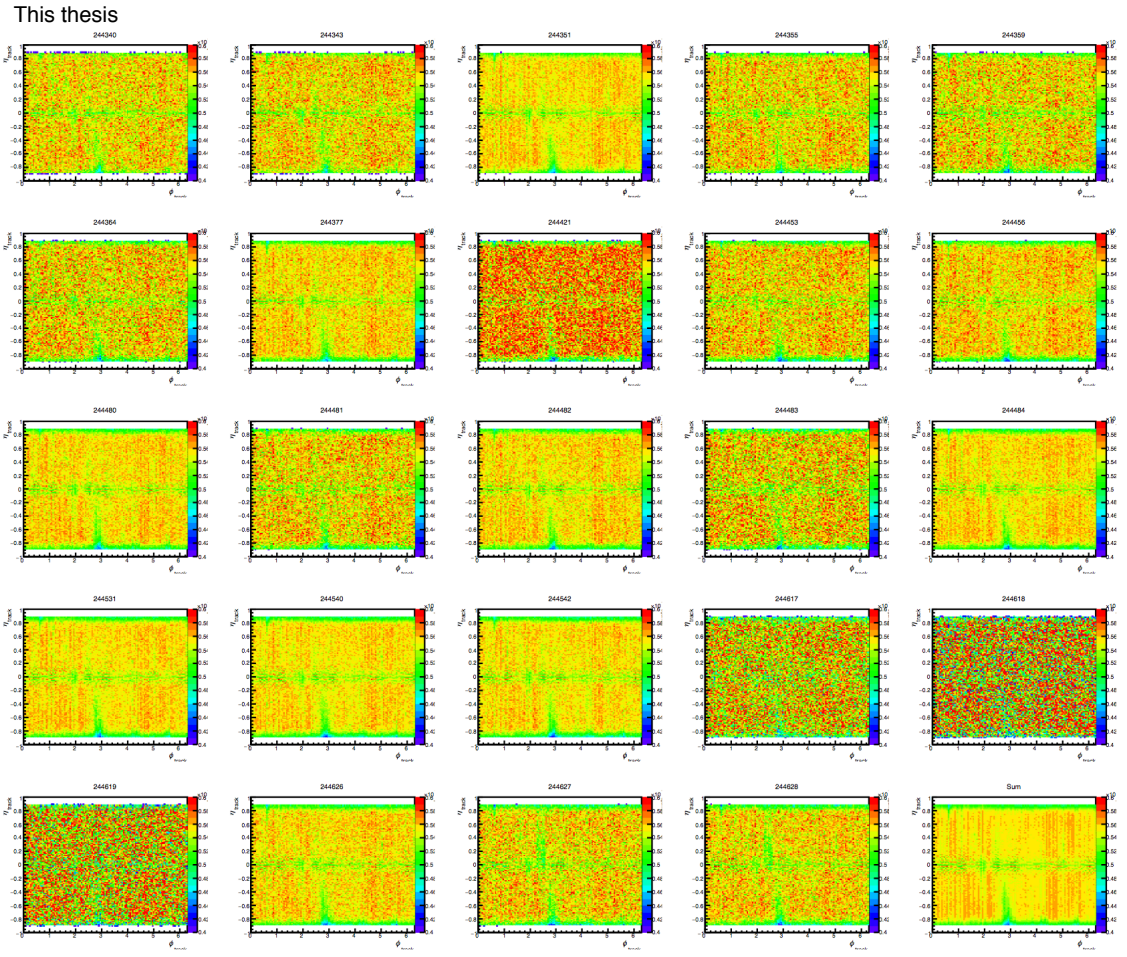

Figure 117: ϕ-η distributions of hybrid tracks for each run used for data analysis.

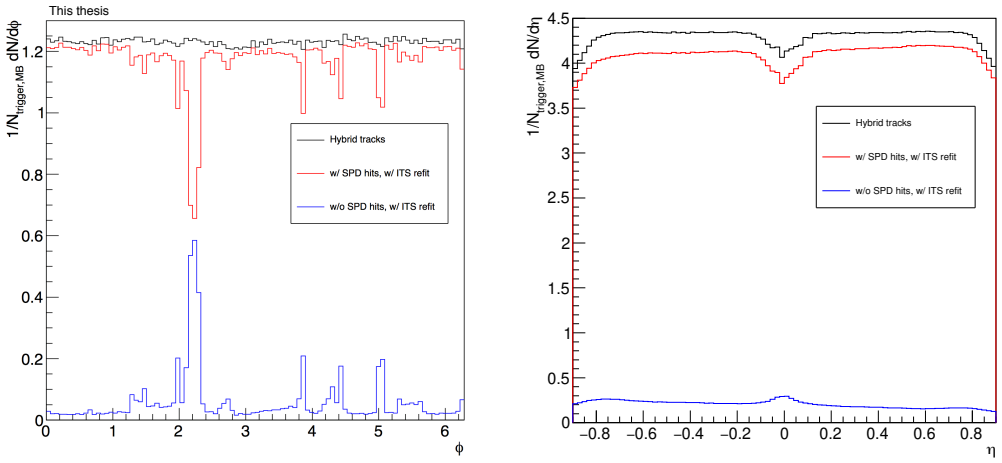

(a) Charged tracks ϕ distribution

(b) Charged tracks η distribution

Figure 118: ϕ and η distributions of charged tracks (a) with Hybrid track cut (black), (b) with SPD hits and ITS refit (red), and (c) without SPD hit and ITS refit (blue) .

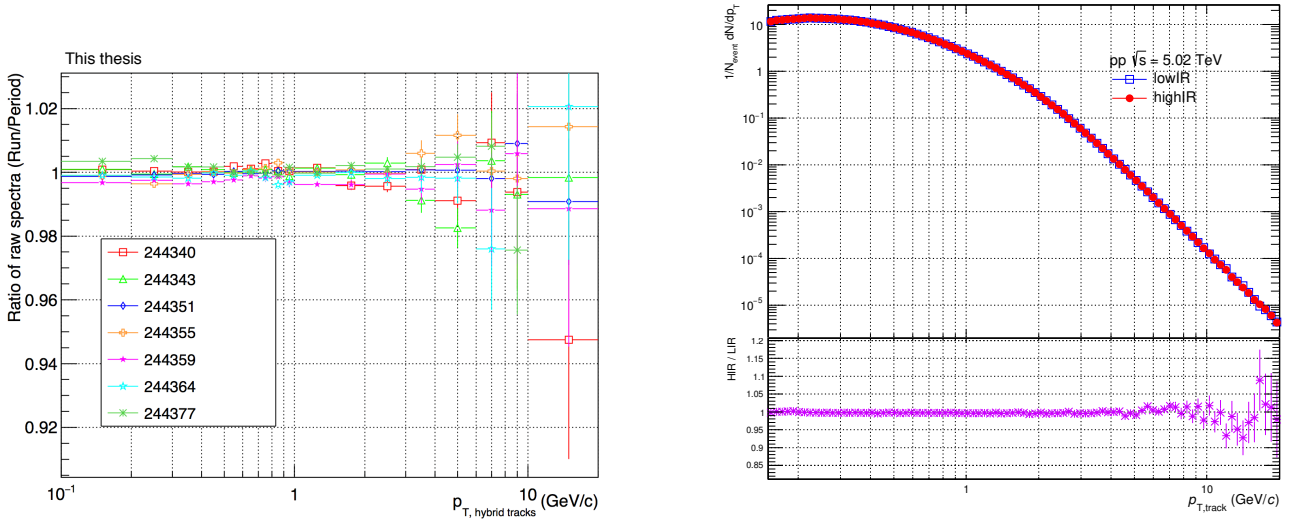

(a) Ratio of hybrid tracks p_{T} spectra in LIR to the merged LIR period.

(b) Hybrid tracks p_{T} spectra and ratio in LIR and HIR.

Figure 119: Validation of hybrid tracks p_{T} spectra per data collection period.

Bibliography

[1] A. Einstein, "Über den einfluß der schwerkraft auf die ausbreitung des lichtes," *Annalen der Physik* **340** 10, (1911) 898–908.

[2] C. Patrignani, Particle Data Group, "Review of Particle Physics," *Chinese Physics C* **40** 10, (Oct., 2016) 100001.

[3] R. Oerter, "The Theory of Almost Everything: The Standard Model, the Unsung Triumph of Modern Physics," *Penguin Group* **0-13-236678-9** (2006) .

[4] P. W. Higgs, "Broken symmetries, massless particles and gauge fields," *Physics Letters* **12** 2, (1964) 132–133.

[5] H. Yokoyama, *Measurement of jet spectra reconstructed with charged particles in Pb-Pb collisions at $\sqrt{s_{NN}}$ = 5.02 TeV with the ALICE detector at the LHC*. PhD thesis, University of Tsukuba and Université Grenoble Alpes, 2018.

[6] A. Bednyakov, "Quantum Field Theory and the Electroweak Standard Model," *lectures given at ESHEP2018, Maratea, Italy* (2018) , arXiv:1812.10675 [hep-ph].

[7] F. Halzen, A. D. Martin, *QUARKS & LEPTONS: An Introductory Course in Modern Particle Physics*. Wiley, 1984. ISBN:0471887412, 9780471887416.

[8] S. Sarkar, H. Satz, B. Sinha, *The Physics of the Quark-Gluon Plasma: Introductory Lectures (Lecture Notes in Physics 785)*. Springer, 2010.

[9] S. Aoki *et al.*, "2+1 flavor lattice QCD toward the physical point," *Phys. Rev. D* **79** (2009) , arXiv:0807.1661 [hep-lat].

[10] J. Collins, D. Soper, G. Sterman, "Factorization for Short Distance Hadron - Hadron Scattering," *Nucl. Phys.* **B261** (1985) 104–142.

[11] H1 and ZEUS collaborations, F. Aaron, *et al.*, "Combined Measurement and QCD Analysis of the Inclusive $e^{\pm}$ p Scattering Cross Sections at HERA," *Journal of High Energy Physics* **109** (2010) .

[12] D. de Florian *et al.*, "Parton-to-Pion Fragmentation Reloaded," *Phys. Rev. D* **91** (2015) .

[13] J. Collins, M. Perry, "Superdense Matter: Neutrons Or Asymptotically Free Quarks?," *Phys. Rev. Lett* **34** (1975) .

[14] G. Aarts *et al.*, "QCD at nonzero chemical potential: Recent progress on the lattice," *AIP Conference Proceedings* **1701** 020001, (2016) .

[15] S. Borsányi *et al.*, "The QCD equation of state with dynamical quarks," *J. High Energ. Phys.* **77** (2010) .

[16] S. Adler, *et al.* (PHENIX Collaboration), "Systematic studies of the centrality and $\sqrt{s_{NN}}$ dependence of the $dE_T/d\eta$ and $dN_{ch}/d\eta$ in heavy ion collisions at midrapidity," *Phys. Rev. C* **71** (2005) .

[17] **CMS** Collaboration, *Pseudorapidity and centrality dependence of energy flow in 2.76TeV PbPb collisions*. No. CMS-PAS-HIN-11-003. CERN, Geneva, 2011. `http://cds.cern.ch/record/1354215`.

[18] R. Hosokawa *et al.*, "Measurement of charged jet cross section in pp collisions at $\sqrt{s}$ = 5.02 TeV." ALICE Internal Analysis Note.

[19] R. Snellings, "Collective expansion at the LHC: selected ALICE anisotropic flow measurements," *J. Phys. G: Nucl. Part. Phys.* **41** 124007, (2014) .

[20] S. J. Das *et al.*, "Relating centrality to impact parameter in nucleus-nucleus collisions," *Phys. Rev. C* **97** 014905, (2018) .

[21] J. S. Moreland, J. E. Bernhard, S. A. Bass, "Alternative ansatz to wounded nucleon and binary collision scaling in high-energy nuclear collisions," *Phys. Rev. C* **92** (2015) 011901, `arXiv:1412.4708 [[nucl-th]]`.

[22] B. Abelev *et al.* (ALICE Collaboration), "Centrality determination of Pb-Pb collisions at $\sqrt{s_{\rm NN}}$ = 2.76 TeV with ALICE," *Phys. Rev. C* **88** 044909, (2013) .

[23] J. Adam, *et al.*, A. Collaboration), "Centrality dependence of the charged-particle multiplicity density at mid-rapidity in Pb-Pb collisions at $\sqrt{s_{\rm NN}}$ = 5.02 TeV," *Phys. Rev. Lett.* **116** 222302, (2016) .

[24] M. L. Miller *et al.*, "Glauber Modeling in High Energy Nuclear Collisions," *Ann. Rev. Nucl. Part. Sci.* **57** (2007) 205–243.

[25] B. Alver, G. Roland, "Collision-geometry fluctuations and triangular flow in heavy-ion collisions," *Phys. Rev. C* **81** 054905, (2010) .

[26] J. L. Nagle, M. P. McCumber, "Heavy ion initial conditions and correlations between higher moments in the spatial anisotropy," *Phys. Rev. C* **83** 044908, (2011) .

[27] C. Loizides, J. Nagle, P. Steinberg, "Improved version of the PHOBOS Glauber Monte Carlo," *SoftwareX* **1-2** (2015) 13–18, `arXiv:1408.2549 [nucl-ex]`.

[28] The CMS Collaboration, A. M. Sirunyan *et al.*, "Jet properties in PbPb and pp collisions at $\sqrt{s}_{\mathrm{NN}} = 5.02$ TeV," *J. High Energ. Phys.* **6** (2018) .

[29] D. d'Enterria, "Jet quenching," `arXiv:0902.2011 [nucl-ex]`.

[30] ALICE Collaboration, "Charged jet cross sections and properties in proton-proton collisions at $\sqrt{s}$ =7 TeV," *Phys. Rev. D* **91** 112012, (2015) .

[31] A. Collaboration, "Measurement of the inclusive jet cross section in pp collisions at $\sqrt{s} = 2.76$ TeV and comparison to the inclusive jet cross section at $\sqrt{s} = 7$ TeV using the ATLAS detector," *Eur. Phys. J. C* **73** 2509, (2013) .

[32] J. Adams *et al.* (STAR Collaboration), "Evidence from d + Au Measurements for Final-State Suppression of High-p_{T} Hadrons in Au + Au Collisions at RHIC," *Phys. Rev. Lett.* **91** 072304, (2003) .

[33] The CMS Collaboration, V. Khachatryan *et al.*, "Charged-particle nuclear modification factors in PbPb and pPb collisions at $\sqrt{s_{\mathrm{NN}}} = 5.02$ TeV," *J. High Energ. Phys.* **39** (2017) .

[34] G. I. Veres (for the CMS Collaboration), "Overview of results on jets from the CMS Collaboration," *Nucl. Phys. A* **904-905** (2013) 146c–153c.

[35] H. Yokoyama (for the ALICE collaboration), "Measurement of Inclusive Charged Jet Production in pp and Pb–Pb collisions at $\sqrt{s_{\mathrm{NN}}} = 5.02$ TeV with ALICE," *Nucl. and Part. Phys. Proceedings* **289-290** (2017) 109–112.

[36] A. Collaboration, "Azimuthal anisotropy of charged jet production in $\sqrt{s_{\mathrm{NN}}} = 2.76$ TeV Pb-Pb collisions," *Phys. Lett. B* **753** (2016) 511–525.

[37] K. C. Zapp, "JEWEL 2.0.0 - Directions for Use," *Eur. Phys. J. C* **74** (2014) .

[38] Y. Tachibana, N. B. Chang, G. Y. Qin, "Full jet in quark-gluon plasma with hydrodynamic medium response," *Phys. Rev. C* **95** 044909, (2017) .

[39] J. Adam *et al.* (ALICE Collaboration), "Anisotropic Flow of Charged Particles in Pb-Pb Collisions at $\sqrt{s_{\rm NN}} = 5.02$ TeV," *Phys. Rev. Lett.* **116** 132302, (2016) .

[40] H. Niemi *et al.*, "Predictions for 5.023 TeV Pb + Pb collisions at the CERN Large Hadron Collider," *Phys. Rev. C* **93** 014912, (2016) .

[41] J. Noronha-Hostler, M. Luzum, J.-Y. Ollitrault, "Hydrodynamic predictions for 5.02 TeV Pb-Pb collisions," *Phys. Rev. C* **93** 034912, (2016) .

[42] "CERN: Home." `https://home.cern`.

[43] **ALICE** Collaboration, E. Abbas *et al.*, "Performance of the ALICE VZERO system," *JINST* **8** (2013) P10016, `arXiv:1306.3130 [nucl-ex]`.

[44] **ALICE** Collaboration, B. Abelev *et al.*, "Performance of the ALICE Experiment at the CERN LHC," *Int. J. Mod. Phys. A* **29** (2014) 1430044, `arXiv:1402.4476 [nucl-ex]`.

[45] **ALICE** Collaboration, K. Aamodt *et al.*, "Alignment of the ALICE Inner Tracking System with cosmic-ray tracks," *JINST* **5** (2010) P03003, `arXiv:1001.0502 [physics.ins-det]`.

[46] K. Røed, *Single Event Upsets in SRAM FPGA based readout electronics for the Time Projection Chamber in the ALICE experiment.* PhD thesis, University of Bergen, 2009.

[47] C. Lippmann, "Performance of the alice time projection chamber," *Phys. Procedia* **37** (2012) 434–441.

[48] A. Akindinov *et al.*, "Latest results on the performance of the multigap resistive plate chamber used for the ALICE TOF," *Nucl. Instrum. Meth. A* **533** (2004) 74–78.

[49] N. Jacazio (for The ALICE collaboration), "PID performance of the ALICE-TOF detector in Run 2," `arXiv:1809.00574 [physics.ins-det]`.

[50] **ALICE** Collaboration, J. Allen *et al.*, "ALICE DCal: An Addendum to the EMCal Technical Design Report Di-Jet and Hadron-Jet correlation measurements in ALICE," Tech. Rep. CERN-LHCC-2010-011. ALICE-TDR-14-add-1, CERN, 2010.

[51] O. Bourrion, "STU manual." Alice internal document.

[52] R. Divià, P. Jovanovic, P. Van de Vyvre, "Data Format over the ALICE DDL; version 11," Tech. Rep. ALICE-INT-2002-10-V11. CERN-ALICE-INT-2002-10-V11, CERN, Geneva, Mar, 2007. https://cds.cern.ch/record/1027339.

[53] R. Divià, "ALICE Common Data Header specifications." ALICE Internal Note.

[54] D. S. (for the ALICE Collaboration), "Energy and system dependence of nuclear modification factors of inclusive charged particles and identified light hadrons measured in pPb, XeXe and PbPb collisions with ALICE," *Nucl. Phys.* **A982** (2019) 567–570, arXiv:1807.11240 [hep-ex].

[55] D. K. (for the ALICE Collaboration), "Probing beauty and charm production in p-Pb collisions with high pT electrons measured with ALICE," in *27th International Conference on Ultra-relativistic Nucleus-Nucleus Collisions (Quark Matter 2018).* 2018.

[56] "ALICE Collaboration." http://alice-collaboration.web.cern.ch.

[57] T. Sjostrand, S. Mrenna, P. Skands, "PYTHIA 6.4 Physics and Manual," *J. High Energ. Phys.* **05** (2006) .

[58] T. S. ostrand *et al.*, "An Introduction to PYTHIA 8.2," *Comput. Phys. Commun.* **191** (2015) 159–177.

[59] X.-N. Wang, M. Gyulassy, "HIJING: A Monte Carlo model for multiple jet production in pp, pA and AA collisions," *Phys. Rev. D* **44** (1991) 3501–3516.

[60] R. Brun *et al.*, *GEANT Detector Description and Simulation Tool.* No. CERN-W5013, CERN-W-5013, W5013, W-5013. CERN, 1994.

[61] A. Collaboration, "ALICE: Physics Performance Report, Volume II," *J. Phys. G: Nucl. Part. Phys.* **32** (2006) 1295.

[62] M. Cacciari, G. P. Salam, "The anti-k_{T} jet clustering algorithm," *J. High Energ. Phys.* **04** (2008) .

[63] M. Cacciari, G. P. Salam, G. Soyez, "FastJet user manual," *Eur. Phys. J. C* **72** (2012) 1896.

[64] ATLAS Collaboration, "Properties of jets measured from tracks in proton-proton collisions at center-of-mass energy $\sqrt{s} = 7$ TeV with the ATLAS detector," *Phys. Rev. D* **84** (2011) 054001.

[65] A. Hoecker, V. Kartvelishvili, "SVD Approach to Data Unfolding," *Nucl. Instrum. Meth. A* **372** (1996) 469–481.

[66] "RooUnfold: ROOT Unfolding Framework." `http://hepunx.rl.ac.uk/~adye/software/unfold/RooUnfold.html`.

[67] T. Adye, "Unfolding algorithms and tests using RooUnfold," *Proceedings of the PHYSTAT 2011 Workshop, CERN, Geneva, Switzerland* (2011) 313–318, `arXiv:1105.1160 [physics.data-an]`.

[68] **ALICE** Collaboration, B. Abelev et al., "ALICE luminosity determination for pp collisions at $\sqrt{s} = 5$ TeV,". `https://cds.cern.ch/record/2202638`.

[69] A. M. Poskanzer, S. A. Voloshin, "Methods for analyzing anisotropic flow in relativistic nuclear collisions," *Phys. Rev. C* **58** (2011) 1671.

[70] T. Todoroki, *Measurements of Two-Particle Correlations with respect to Higher-Order Event Planes in $\sqrt{s_{NN}}$ = 200 GeV Au+Au Collisions at RHIC-PHENIX*. PhD thesis, University of Tsukuba, 2014.

[71] J. Y. Ollitrault, "Determination of the reaction plane in ultrarelativistic nucler collisions," *Phys. Rev. D* **48** (1993) 1132.

[72] **ALICE** Collaboration, B. Abelev *et al.*, "Measurement of charged jet suppression in Pb-Pb collisions at $\sqrt{s_{NN}}$=2.76TeV," *JHEP* **30** CERN-PH-EP-2013-205. CERN-PH-EP-2013-205, (Nov, 2013) 013. `http://cds.cern.ch/record/1624179`.

[73] **ALICE** Collaboration, B. B. Abelev *et al.*, "Charged jet cross sections and properties in proton-proton collisions at $\sqrt{s} = 7$ TeV," *Phys. Rev. D* **91** CERN-PH-EP-2014-254. CERN-PH-EP-2014-254, (Nov, 2014) 112012. `http://cds.cern.ch/record/1970694`.

[74] **ALICE** Collaboration, S. Acharya et al., "Constraints on jet quenching in p-Pb collisions at $\sqrt{\mathbf{s_{NN}}} = 5.02$ TeV measured by the event-activity dependence of semi-inclusive hadron-jet distributions," *Phys. Lett.* **B783** (2018) 95–113, `arXiv:1712.05603 [nucl-ex]`.

[75] PHENIX Collaboration, "Measurement of two-particle correlations with respect to second- and third-order event planes in Au+Au collisions at $\sqrt{s_{NN}} = 200$ GeV," arXiv:1803.01749 [hep-ex].

[76] B. Andersson, G. Gustafson, B. Söderberg, "A general model for jet fragmentation," *Z. Phys. C* **20** (1983) 317.

[77] P. Z. Skands, "Tuning Monte Carlo Generators: The Perugia Tunes," *Phys.Rev.* **D82** 074018, arXiv:1005.3457 [hep-ph].

[78] P. Skands, S. Carrazza, J. Rojo *Eur. Phys. J.* 3024, arXiv:1404.5630 [hep-ph].

[79] "ATLAS Run 1 Pythia8 tunes," Tech. Rep. ATL-PHYS-PUB-2014-021, CERN, Geneva, Nov, 2014. http://cds.cern.ch/record/1966419.

[80] **CMS** Collaboration, V. Khachatryan et al., "Event generator tunes obtained from underlying event and multiparton scattering measurements," *Eur. Phys. J.* **C76** (2016) 155, arXiv:1512.00815 [hep-ex].

[81] **CTEQ** Collaboration, H. Lai et al., "Global QCD analysis of parton structure of the nucleon: CTEQ5 parton distributions," *Eur.Phys.J.* 375, arXiv:hep-ph/9903282 [hep-ph].

[82] R. D. Ball et al., "Parton distributions with LHC data," *Nucl. Phys. B* **867** (2013) 244–289, arXiv:1207.1303 [hep-ph].

[83] S. Alioli *et al.*, "Jet pair production in POWHEG," *JHEP* **04** (2011) 081, arXiv:1012.3380 [hep-ph].

[84] P. Nason, "A New method for combining NLO QCD with shower Monte Carlo algorithms," *JHEP* **11** (2004) 040, arXiv:hep-ph/0409146 [hep-ph].

[85] S. Alioli *et al.*, "A general framework for implementing NLO calculations in shower Monte Carlo programs: the POWHEG BOX," *JHEP* **06** (2010) 043, arXiv:1002.2581 [hep-ph].

[86] S. Frixione, P. Nason, C. Oleari, "Matching NLO QCD computations with Parton Shower simulations: the POWHEG method," *JHEP* **11** (2007) 070, arXiv:0709.2092 [hep-ph].

[87] S. Dulat *et al.*, "New parton distribution functions from a global analysis of quantum chromodynamics," *Phys. Rev.* **D93** (2016) 033006, arXiv:1506.07443 [hep-ph].

[88] T. Gehrmann *et al.*, "Jet cross sections and transverse momentum distributions with NNLOJET," *Contribution to the Proceedings of the RADCOR2017, 24-29 Sep., 2017, St. Gilgen, Austria* (2018) , arXiv:1801.06415 [hep-ph].

[89] **ALICE** Collaboration, B. Abele *et al.*, "Underlying Event measurements in pp collisions at $\sqrt{s} = 0.9$ and 7 TeV with the ALICE experiment at the LHC," *J. High Energ. Phys.* **07** (2012) 116, arXiv:1112.2082 [hep-ex].

[90] P. Christiansen, K. Tywoniuk, V. Vislavicius, "Universal scaling dependence of QCD energy loss from data driven studies," *Phys. Rev.* **C89** 3, (2014) 034912, arXiv:1311.1173 [hep-ph].

[91] **ALICE** Collaboration, S. Acharya et al., "Analysis of the apparent nuclear modification in peripheral Pb-Pb collisions at 5.02 TeV," arXiv:1805.05212 [nucl-ex].

[92] R. Haake, C. Loizides, "Machine Learning based jet momentum reconstruction in heavy-ion collision," arXiv:1810.06324 [nucl-ex].

[93] **ALICE** Collaboration, F. Costa, A. Kluge, P. Vande Vyvre, "The detector read-out in ALICE during Run 3 and 4," *J. Phys. Conf. Ser.* **898** 3, (2017) 032011.

[94] D. Rohr *et al.*, "Track Reconstruction in the ALICE TPC using GPUs for LHC Run 3," arXiv:1811.11481 [physics.ins-det].